Supporting Information

Excited State Dynamics of Odd [*n*]Cumulenes: Chain length and Conformational Effects

Tobias Ullrich,[1] Bozheng Sun,[2] Yanwen Yang,[2] Christoph M. Schüßlbauer,[1] Michael J. Ferguson,[2] Daniele Fazzi,[3] Fabrizia Negri,[3] Matteo Tommasini,[4] Rik R. Tykwinski,[2*] Dirk M. Guldi[1*]

1 Department of Chemistry and Pharmacy and Interdisciplinary Center for Molecular Materials (ICMM), Friedrich-Alexander-University Erlangen-Nuremberg, 91058, Erlangen, Germany.

2 Department of Chemistry, University of Alberta, Edmonton, AB T6G 2G2, Canada.

3 Dipartimento di Chimica "Giacomo Ciamician", Università degli studi di Bologna, 40126, Bologna, Italy.

4 Dipartimento di Chimica, Materiali e Ingegneria Chimica "Giulio Natta", Politecnico di Milano, 20133, Milano, Italy.

Contents

Synthesis and Characterization

General Methods

Reagents were purchased reagent grade from commercial suppliers and used without further purification. Dried reaction solvents for the synthesis were from an SP-1 Stand Alone Solvent Purification System, LC Technology Solution Inc. Air or moisture sensitive reactions were performed in oven-dried glassware under an atmosphere of nitrogen. Any additional deoxygenation of reaction mixtures was achieved by purging nitrogen through the solution for at least 20 min, unless specified otherwise. Saturated (satd.) NH_4Cl and brine refer to saturated aqueous solutions of NH_4Cl and NaCl, respectively. All ratios of liquids are v/v.

^1H NMR spectra were recorded on one of the following instruments in the Department of Chemistry at the University of Alberta: an Agilent/Varian Inova four-channel 500 MHz spectrometer at 500 MHz; an Agilent/Varian VNMRS two-channel 500 MHz spectrometer at 500 MHz; or an Agilent VNMRS four-channel dual receiver 700 MHz spectrometer at 700 MHz. ^{13}C NMR spectra were recorded as broadband decoupled spectra on an Agilent/Varian VNMRS two-channel 500 MHz spectrometer with cold probe at 125 MHz or an Agilent VNMRS four-channel dual receiver 700 MHz spectrometer at 175 MHz. NMR spectra were referenced to the residual solvent signal (^1H: $CHCl_3$: 7.26 ppm, CH_2Cl_2: 5.32 ppm; ^{13}C: $CDCl_3$: 77.06 ppm, CD_2Cl_2: 53.80 ppm). Coupling constants are reported as observed.

UV-vis spectroscopy measurements were carried out on a Varian Cary 400 UV-vis spectrometer at rt with quartz cuvettes having one-centimeter path length. The wavelengths are recorded in nm, the molar extinction ε is reported in L mol^{-1} cm^{-1}.

Mass spectrometry was obtained from Bruker 9.4T Apex-Qe FTICR (MALDI), Agilent Technologies 6220 aoTOF (ESI and APPI), and Kratos MS50G (EI) instruments. Low-resolution data are provided in cases when M^+ is not the base peak; otherwise, only high-resolution data are provided.

IR spectra were recorded on a Nicolet 8700-continuum microscope system.

X-ray crystallographic analysis was performed using a Bruker D8/APEX II CCD diffractometer at the Department of Chemistry, University of Alberta.

Melting points and decomposition temperatures were obtained from a Thomas Hoover capillary melting point apparatus. DSC results were obtained from a Pyris 1 DSC by Perkin Elmer or a Polymer Differential Scanning Calorimeter by Mettler Toledo.

TLC analyses were carried out on TLC plates from Merck (TLC silica gel 60 F_{254}) or Macherey-Nagel (ALUGRAM® SIL G/UV254) and visualized via UV-light (254 nm). Column chromatography was performed using silica gel (SilicaFlash P60, Silicycle; 60M Merck).

Synthetic Protocols and Compound Characterization of the [*n*]*oi*Pr Series

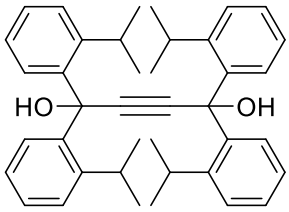

Compound 1: A solution of 2-isopropylbromobenzene (1.8 g, 9.0 mmol) in dry THF (30 mL) was cooled to –78 °C under an atmosphere of nitrogen. *n*BuLi (2.5 M in hexanes, 3.6 mL, 9.0 mmol) was added dropwise over 5 min, and the mixture was allowed to stir for 1 h. Dimethyl acetylenedicarboxylate (0.28 g, 0.24 mL, 2.0 mmol) was dissolved in THF (5 mL) and added to the solution of aryl lithium dropwise over a period of 1 min. The reaction was warmed to rt and stirred for an additional 16 h. The reaction mixture was quenched through the addition of satd. aq. NH_4Cl (30 mL). The organic phase was separated, and the aqueous phase was extracted with Et_2O (3 × 20 mL). The combined organic phases were washed with brine (100 mL), dried ($MgSO_4$), filtered, and the solvent removed in vacuo. Purification by column chromatography (silica gel, hexanes/ethyl acetate 30:1) afforded compound **1** (0.16 g, 14%) as a white solid. Mp 184–187 °C. R_f = 0.59 (hexanes/ethyl acetate 5:1). IR (solid): 3573 (s), 3438 (s, br), 3066 (s), 3024 (m), 2960 (s), 2955 (s), 2868 (s), 2219 (w), 2099 (s), 1600 (m), 1481 (s), 1446 (s), 1353 (s), 1250 (s), 1146 cm^{-1}; ^1H NMR (498 MHz, $CDCl_3$) δ 7.95 (d, J = 7.8 Hz, 4H), 7.28–7.21 (m, 8H), 7.17–7.13 (m, 4H), 3.38–3.29 (m, 4H), 2.79 (s, 2H), 0.72 (d, J = 6.5 Hz, 12H), 0.66 (d, J = 6.7 Hz, 12H); ^{13}C NMR (126 MHz, $CDCl_3$) δ 147.7, 140.6, 128.3, 127.7, 126.8, 125.2, 91.0, 75.2, 29.0, 23.8, 23.2. ESI HRMS calcd for $C_{40}H_{46}NaO_2$ ($[M + Na]^+$) 581.3390, found 581.3387.

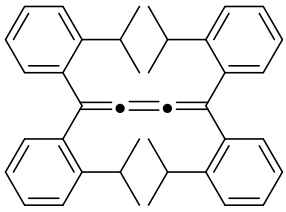

[3]*oi*Pr: To a solution of **1** (0.10 g, 0.18 mmol) in dry Et_2O (10 mL) was added $SnCl_2$ (0.12 g, 0.63 mmol) and HCl (1.0 M in Et_2O, 0.72 mL, 0.72 mmol). The resulting mixture was stirred for 3 h at rt. The reaction mixture was passed through a plug of basic alumina and eluted with CH_2Cl_2 (20 mL). The resulting solution was concentrated under a flow of nitrogen to a minimum amount (ca. 4 mL) and layered with methanol (12 mL) at rt for recrystallization, which afforded **[3]*oi*Pr** (50 mg, 53%) as a light yellow crystalline solid. Mp 188 °C (decomp). R_f = 0.57 (hexanes/CH_2Cl_2, 5:1). UV-vis (CH_2Cl_2) λ_{max} (ε) 261 (19700), 320 (sh, 8590), 373 (30200); IR (CH_2Cl_2 cast): 3061 (m), 3019 (m), 2963 (s), 2867 (s), 1952 (vw), 1920 (vw), 1596 (m), 1481 (s), 1441 (s), 1383 (m), 1362 (m) cm^{-1}; ^1H NMR (498 MHz, CD_2Cl_2) δ 7.28 (dd, J = 7.9, 1.4 Hz, 4H), 7.23 (dt, J = 7.6, 1.5 Hz, 4H), 7.12 (dd, J = 7.7, 1.5 Hz, 4H), 7.07, (dt, J = 7.4, 1.4 Hz, 4H), 3.36 (sept, J = 6.8 Hz, 4H), 0.92 (d, J = 6.9 Hz, 24H); ^{13}C NMR (126 MHz, CD_2Cl_2) δ 157.4, 147.6, 139.4, 130.5, 128.4, 126.4, 125.7, 121.8, 29.7, 23.8. EIMS *m/z* 524.3 (M^+, 23), 481.3 ($[M – iPr]^+$, 14), 262.2 (26), 247.1 (100); EI HRMS calcd for $C_{40}H_{44}$ (M^+) 524.3443, found 524.3433. DSC: decomposition, 188 °C (onset), 213 °C (peak).

A crystal of **[3]*oi*Pr** suitable for X-ray crystallographic analysis has been grown at rt, by slow diffusion of a CH_2Cl_2 solution layered with methanol. X-ray data for **[3]*oi*Pr** ($C_{40}H_{44}$), F_w = 524.75; triclinic crystal system; space group $P\bar{1}$ (No. 2); a = 10.9279(4) Å, b = 11.6448(5) Å, c = 14.2982(6) Å; α = 99.446(3)°, β = 109.913(3)°, γ = 102.504(3)°; V = 1613.08(12) $Å^3$; Z = 2; ρ_{calcd} = 1.080 $g \cdot cm^{-3}$; $2\theta_{max}$ = 141.19°; μ = 0.449 mm^{-1}; T = 173 K; total data collected = 33738; R_1 = 0.0510 [4364 observed reflections with $F_o^2 \geq 2\sigma(F_o^2)$]; ωR_2 = 0.1425 for 6118 data, 362 parameters, and 0 restraints; largest difference peak and hole = 0.311 and –0.224 e $Å^{-3}$. CCDC 2409930.

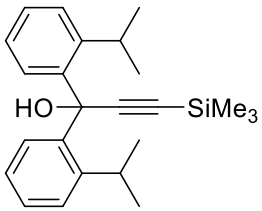

Compound 2: A solution of 2-isopropylbromobenzene (2.2 g, 11 mmol) in dry THF (50 mL) was cooled to –78 °C under an atmosphere of nitrogen. *n*BuLi (2.5 M in hexanes, 4.4 mL, 11 mmol) was added dropwise over 5 min, and the mixture allowed to stir for 1 h. Ethyl 3-[trimethylsilyl]-propynoate[1] (0.85 g, 5.0 mmol) was dissolved in THF (10 mL) and added dropwise to the solution of the aryl lithium over a period of 2 min. The reaction was warmed to rt and stirred for additional 16 h. The reaction mixture was quenched through the addition of satd. aq. NH_4Cl (40 mL). The organic phase was separated, and the aqueous phase was extracted with Et_2O (3 × 20 mL). The combined organic phases were washed with brine (100 mL), dried ($MgSO_4$), filtered, and the solvent removed in vacuo. Purification by column chromatography (silica gel, hexanes/CH_2Cl_2 2:1) afforded **2** (1.1 g, 60%) as a white solid. Mp 98–100 °C. R_f = 0.30 (hexanes/CH_2Cl_2 2:1). IR (CH_2Cl_2 cast): 3546 (m, br), 3065 (m), 3024 (m), 2962 (s), 2868 (s), 2167 (m), 1600 (w), 1482 (s), 1446 (s), 1251 (s), 1047 (s) cm^{-1}; ^1H NMR (498 MHz, $CDCl_3$) δ 7.92 (d, J = 7.9 Hz, 2H), 7.31–7.27 (m, 4H), 7.20–7.16 (m, 2H), 3.44 (sept, J = 6.6 Hz, 2H), 0.86–0.82 (m, 12H), 0.20 (s, 9H), signal of the OH group was not observed; ^{13}C NMR (126 MHz, $CDCl_3$) δ 147.9, 140.5, 128.3, 127.6, 126.7, 125.1, 108.1, 92.2, 74.7, 29.0, 23.7, 23.5, –0.1. EIMS *m/z* 364.2 (M^+, 1), 321.2 ([M – *i*Pr]$^+$, 7), 223.1 (35), 73.0 ([C_3H_9Si]$^+$, 100); EI HRMS calcd for $C_{24}H_{32}OSi$ (M^+) 364.2222, found 364.2221.

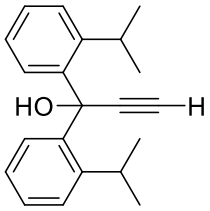

Compound 3: To a solution of alkyne **2** (0.90 g, 2.5 mmol) in CH_2Cl_2/MeOH (40 mL, 1:1) was added K_2CO_3 (0.85 g, 6.2 mmol), and the solution was stirred at rt for 3 h. The solvent was removed in vacuo, and the residue was dissolved in CH_2Cl_2 (20 mL). Satd. aq. NH_4Cl (20 mL) was added, and the organic phase separated. The aqueous phase was extracted with CH_2Cl_2 (2 × 15 mL). The combined organic phases were washed with brine (50 mL), dried ($MgSO_4$), filtered, and the solvent removed in vacuo to afford **3** (0.70 g, 96%) as a white solid. Mp 79–82 °C. R_f = 0.22 (hexanes/CH_2Cl_2 = 2:1). IR (CH_2Cl_2 cast): 3542 (s, br), 3303 (s), 3064 (m), 3024 (m), 2956 (s), 2868 (s), 2107 (vw), 1600 (w), 1576 (w), 1482 (s), 1446 (s), 1362 (s), 1028 (s) cm^{-1}; ^1H NMR (500 MHz, $CDCl_3$) δ 7.96 (d, J = 7.7 Hz, 2H), 7.32–7.25 (m, 4H), 7.21 (ddd, J = 8.0, 6.3, 2.4 Hz, 2H), 3.39 (sept, J = 6.8 Hz, 2H), 2.94 (s, 1H), 2.76 (s, 1H), 0.85–0.81 (m, 12H). ^{13}C NMR (126 MHz, $CDCl_3$) δ 147.7, 140.3, 128.5, 127.8, 126.6, 125.2, 86.8, 76.3, 74.6, 29.0, 23.7, 23.3. EIMS *m/z* 292.2 (M^+, 7), 223.1 (100); EI HRMS calcd for $C_{21}H_{24}O$ (M^+) 292.1827, found 292.1825.

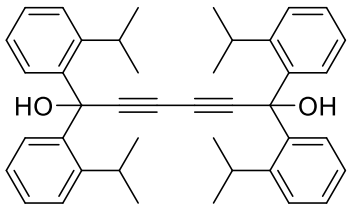

Compound 4: Terminal alkyne **3** (0.95 g, 3.2 mmol) was added to a solution of the Hay catalyst [CuCl (0.35 g, 3.5 mmol) and TMEDA (1.0 mL, 0.81 g, 7.0 mmol) in CH_2Cl_2 (30 mL), previously stirred until homogenous]. This mixture was stirred at rt under air for 1 d. Satd. aq. NH_4Cl (20 mL) was added, and the organic phase was separated. The aqueous phase was extracted with $CHCl_3$ (2 × 20 mL). The combined organic phases were washed with brine (40 mL), dried ($MgSO_4$), filtered, and the solvent removed in vacuo. Purification by column chromatography (silica gel, hexanes/ethyl acetate, 10:1) afforded **4** (0.60 g, 64%) as a light yellow solid. Mp 230–232 °C. R_f = 0.30 (hexanes/ethyl acetate, 10:1). IR (CH_2Cl_2 cast): 3572 (s), 3462 (s, br), 3066 (s), 2963 (s), 2868 (s), 2146 (w), 1600 (m), 1482 (s), 1446 (s), 1363 (s), 1267 (m) cm^{-1}; ^1H NMR (498 MHz, $CDCl_3$) δ 7.83 (d, J = 8.0 Hz, 4H), 7.30–7.26 (m, 8H), 7.19 (ddd, J = 8.4, 6.5, 2.2 Hz, 4H), 3.35 (sept, J = 6.8 Hz, 4H), 2.74 (s, 2H), 0.84 (d, J = 6.8 Hz,

12H), 0.83 (d, J = 6.8 Hz, 12H); ^{13}C NMR (126 MHz, $CDCl_3$) δ 147.8, 139.8, 128.7, 127.8, 126.7, 125.3, 83.3, 75.2, 72.1, 29.2, 23.7, 23.5. ESI MS *m/z* 605.3 ([M + Na]$^+$, 27), 565.3 ([M – OH]$^+$, 100); ESI HRMS calcd for $C_{42}H_{46}NaO_2$ ([M + Na]$^+$) 605.3390, found 605.3405, calcd for $C_{42}H_{45}O$ ([M – OH]$^+$) 565.3465, found 565.3460.

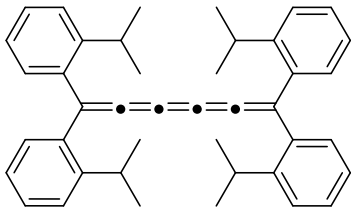

[5]*oi*Pr: To a solution of **4** (87 mg, 0.15 mmol) in dry THF (10 mL) was added $SnCl_2$ (0.10 g, 0.53 mmol) and HCl (1.0 M in Et_2O, 0.60 mL, 0.60 mmol). The resulting mixture was stirred for 3 h at rt. The reaction mixture was passed through a plug of basic alumina and eluted with CH_2Cl_2 (20 mL). The resulting solution was concentrated under a flow of nitrogen to a minimum amount (ca. 2 mL) and layered with methanol (6 mL) at rt for recrystallization, which afforded **[5]*oi*Pr** (19 mg, 23%, the actual yield was likely higher since a visible amount of product has been lost in the mother liquid during recrystallization) as a light orange crystalline solid. Mp 160 °C (decomp). R_f = 0.57 (hexanes/CH_2Cl_2, 5:1). UV-vis (CH_2Cl_2) λ_{max} (ε) 270 (50000), 359 (14400), 430 (sh, 40800), 452 (47300); IR (CH_2Cl_2 cast): 3060 (m), 3018 (m), 2964 (s), 2927 (s), 2868 (m), 1997 (w), 1954 (vw), 1922 (vw), 1595 (m), 1481 (s), 1442 (s), 1384 (m), 1362 (m) cm^{-1}; ^{1}H NMR (500 MHz, CD_2Cl_2) δ 7.37–7.34 (m, 4H), 7.28 (dt, J = 7.4, 1.3 Hz, 4H), 7.12–7.06 (m, 8H), 3.45 (sept, J = 6.9 Hz, 4H), 1.15 (d, J = 6.8 Hz, 24H); ^{13}C NMR (126 MHz, CD_2Cl_2) δ 156.3, 148.0, 139.0, 130.5, 130.3, 129.0, 126.7, 125.9, 123.6, 30.1, 24.1. MALDI HRMS (DCTB) calcd for $C_{42}H_{44}$ (M^+) 548.3438, found 548.3438. DSC: decomposition, 163 °C (onset), 165 °C (peak).

A crystal of **[5]*oi*Pr** suitable for X-ray crystallographic analysis has been grown at rt by slow diffusion of a CH_2Cl_2 solution layered with methanol. X-ray data for **[5]*oi*Pr** ($C_{42}H_{44}$), F_w = 548.77; monoclinic crystal system; space group $P2_1/c$ (No. 14); a = 13.6429(6) Å, b = 8.1223(4) Å, c = 15.3442(7) Å; β = 98.901(4)°; V = 1679.84(14) Å^3; Z = 2; ρ_{calcd} = 1.085 g·cm^{-3}; $2\theta_{max}$ = 136.5°; μ = 0.453 mm^{-1}; T = 193 K; total data collected = 8183; R_1 = 0.0524 [2021 observed reflections with $F_o^2 \geq 2\sigma(F_o^2)$]; ωR_2 = 0.1421 for 3061 data, 191 parameters, and 0 restraints; largest difference peak and hole = 0.242 and –0.151 e Å^{-3}. CCDC 2411740.

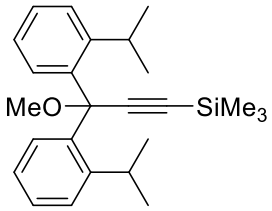

Compound S1: A solution of hexamethyldisilazane (0.53 g, 0.69 mL, 3.3 mmol) in dry THF (10 mL) was cooled to –78 °C under an atmosphere of nitrogen. *n*BuLi (2.5 M in hexanes, 1.1 mL, 2.8 mmol) was slowly added over 2 min, and the mixture allowed to stir for 1 h. Alcohol **2** (0.80 g, 2.2 mmol) was dissolved in THF (10 mL) and then added dropwise to the solution of LiHMDS over a period of 5 min. The mixture was stirred for 1 h while slowly warming to 0 °C. Dimethyl sulfate (1.3 g, 1.0 mL, 10 mmol) was added, and the reaction was warmed to rt and stirred for an additional 1 h. The reaction mixture was quenched through the addition of satd. aq. NH_4Cl (20 mL). The organic layer was separated, and the aqueous layer was extracted with Et_2O (2 × 20 mL). The combined organic phases were washed with brine (50 mL), dried ($MgSO_4$), filtered, and the solvent removed in vacuo. Purification by column chromatography (silica gel, hexanes/CH_2Cl_2 8:1) afforded **S1** (0.78 g, 94%) as a colorless solid. Mp 62–64 °C. R_f = 0.83 (hexanes/CH_2Cl_2 2:1). IR (CH_2Cl_2 cast): 3064 (m), 3023 (m), 2956 (s), 2868 (s), 2823 (m), 2165 (m), 1600 (w), 1482 (s), 1446 (s), 1251 (s) cm^{-1}; ^{1}H NMR (498 MHz, $CDCl_3$) δ 7.90 (d, J = 7.6 Hz, 2H), 7.28–7.22 (m, 4H), 7.19–7.14 (m, 2H), 3.43–3.34 (m, 2H), 3.28 (s, 3H), 0.80–0.74 (m, 12H), 0.21 (s, 9H); ^{13}C NMR (126 MHz, $CDCl_3$) δ 148.1, 139.0, 128.1, 127.5, 124.8, 104.7, 94.0, 80.8, 51.6, 28.7, 23.5, 23.3, 0.0 (one signal coincident or not observed). EIMS

m/z 378.2 (M^+, 0.3), 363.2 ([M – Me]$^+$, 4), 335.2 ([M – *i*Pr]$^+$, 6), 73.0 ([C_3H_9Si]$^+$, 100); EI HRMS calcd for $C_{25}H_{34}OSi$ (M^+) 378.2379, found 378.2375.

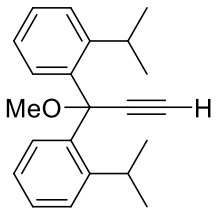

Compound 5: To a solution of alkyne **S1** (1.1 g, 2.9 mmol) in CH_2Cl_2/MeOH (60 mL, 1:1) was added K_2CO_3 (0.96 g, 6.9 mmol), and the solution was stirred at rt for 3 h. The solvent was removed in vacuo, and the residue was dissolved in CH_2Cl_2 (20 mL). Satd. aq. NH_4Cl (20 mL) was added, and the organic phase separated. The aqueous phase was extracted with CH_2Cl_2 (2 × 15 mL). The combined organic phases were washed with brine (50 mL), dried ($MgSO_4$), filtered, and the solvent removed in vacuo to afford **5** (0.82 g, 92%) as a colorless solid. Mp 79–82 °C. R_f = 0.58 (hexanes/CH_2Cl_2 5:1). IR (CH_2Cl_2 cast) 3304 (s), 3064 (m), 3023 (m), 2953 (s), 2868 (s), 2825 (m), 2103 (w), 1599 (m), 1576 (m), 1481 (s), 1446 (s), 1382 (s), 1361 (s), 1066 (s) cm^{-1}; ^{1}H NMR (500 MHz, $CDCl_3$) δ 7.95 (d, J = 7.6 Hz, 2H), 7.31–7.24 (m, 4H), 7.21 (ddd, J = 8.6, 6.9, 1.9 Hz, 2H), 3.36 (sept, J = 7.3 Hz, 2H), 3.30 (s, 3H), 2.90 (s, 1H), 0.79–0.75 (m, 12H). ^{13}C NMR (126 MHz, $CDCl_3$) δ 147.9, 138.8, 128.3, 128.0, 127.6, 124.9, 83.5, 80.7, 77.5, 51.7, 28.7, 23.5, 23.2. EIMS *m/z* 306.2 (M^+, 6), 259.1 (100); EI HRMS calcd for $C_{22}H_{26}O$ (M^+) 306.1984, found 306.1979.

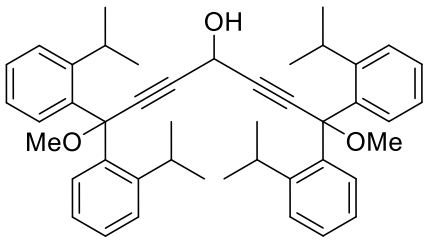

Compound S2: A solution of terminal alkyne **5** (0.91 g, 3.0 mmol) in dry THF (30 mL) was cooled to –78 °C under an atmosphere of nitrogen. *n*BuLi (2.5 M in hexanes, 1.2 mL, 3.0 mmol) was slowly added over a period of 1 min, and the mixture was allowed to stir for 1 h. Ethyl formate (0.12 mL, 0.11 g, 1.5 mmol) was added dropwise to the solution of the lithium acetylide over a period of 1 min. Then, the reaction mixture was warmed slowly to rt and stirred for an additional 4 h. The reaction mixture was quenched through the addition of satd. aq. NH_4Cl (30 mL). The organic phase was separated, and the aqueous phase was extracted with diethyl ether (2 × 20 mL). The combined organic phases were washed with brine (50 mL), dried ($MgSO_4$), filtered, and the solvent removed in vacuo. Purification by gradient elution column chromatography (silica gel, hexanes/ethyl acetate 20:1→10:1) afforded **S2** (0.68 g, 71%) as a white powder that was ca. 90% pure, based on ^{1}H NMR spectroscopy. Mp 63–65 °C. R_f = 0.26 (hexanes/ethyl acetate 10:1). IR (CH_2Cl_2 cast): 3520 (m, br), 3415 (m, br), 3064 (m), 2954 (s), 2868 (s), 2825 (m), 1599 (w), 1575 (w), 1482 (s), 1460 (s), 1383 (s), 1362 (s) cm^{-1}; ^{1}H NMR (500 MHz, $CDCl_3$) δ 7.88 (br s, 4H), 7.29–7.22 (m, 8H), 7.15–7.11 (m, 4H), 5.39 (d, J = 7.7 Hz, 1H), 3.37–3.29 (m, 4H), 3.25 (s, 6H), 2.18 (d, J = 7.9 Hz, 1H), 0.76 (br s, 24H); ^{13}C NMR (126 MHz, $CDCl_3$) δ 147.9, 138.6, 128.3, 128.0, 127.6, 124.94, 124.92, 86.4, 84.7, 80.7, 52.7, 51.8, 28.8, 23.6, 23.4. MALDI MS (DCTB) *m/z* 663.4 ([M + Na]$^+$, 100); MALDI HRMS (DCTB) calcd for $C_{45}H_{52}NaO_3$ ([M + Na]$^+$) 663.3809, found 663.3807.

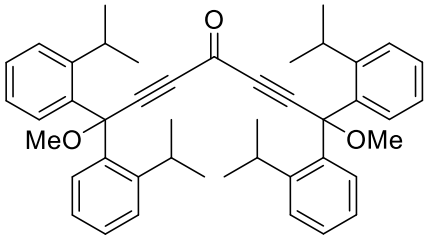

Compound 6: To a solution of alcohol **S2** (0.64 g, 1.0 mmol) in CH_2Cl_2 (15 mL) at rt was added PCC (0.43 g, 2.0 mmol), celite (0.60 g), and molecular sieves (4 Å, 0.60 g). The mixture was stirred at rt for 16 h. The reaction mixture was passed through a plug of silica gel (CH_2Cl_2, 150 mL) to remove the chromium waste, and the solvent was removed in vacuo to afford **6** (0.63 g, quant) as a white powder. Mp 65–68 °C. R_f = 0.65 (hexanes/ethyl acetate 10:1). IR (CH_2Cl_2 cast): 3065 (m), 3024 (m), 2956 (s), 2868 (s), 2826 (m), 2201

(s), 1638 (s), 1482 (s), 1446 (s), 1221 (s) cm^{-1}; ^1H NMR (500 MHz, $CDCl_3$) δ 7.82 (d, J = 8.1 Hz, 4H), 7.35–7.28 (m, 8H), 7.19 (ddd, J = 8.4, 7.0, 1.7 Hz, 4H), 3.32–3.24 (m, 4H), 3.28 (s, 6H), 0.78 (d, J = 6.8 Hz, 24H); ^{13}C NMR (126 MHz, $CDCl_3$) δ 159.7, 148.1, 137.1, 128.8, 128.1, 127.9, 125.2, 92.5, 89.0, 81.2, 52.4, 29.0, 23.6, 23.3. MALDI MS (DCTB) *m/z* 661.4 ($[M + Na]^+$, 100), 607.4 ($[M – OMe]^+$, 20); MALDI HRMS (DCTB) calcd for $C_{45}H_{50}NaO_3$ ($[M + Na]^+$) 661.3652, found 661.3646.

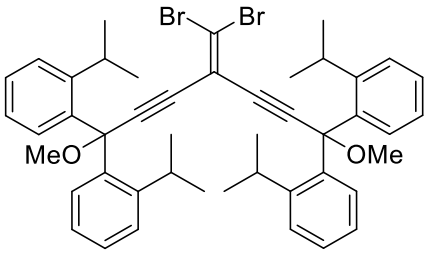

Compound 7: To a solution of triphenylphosphine (1.9 g, 7.2 mmol) in CH_2Cl_2 (25 mL) was added CBr_4 (1.2 g, 3.6 mmol), and the mixture was stirred for 5 min. Ketone **6** (1.7 g, 2.7 mmol) was dissolved in CH_2Cl_2 (10 mL) and added dropwise to the solution of triphenyl phosphonium ylide over a period of 1 min. After stirring for an additional 30 min, the CH_2Cl_2 in the reaction mixture was removed under vacuum, and the residue was dissolved in methanol (25 mL). The resulting solution was poured into water (50 mL), then extracted with hexanes (3 × 50 mL). The combined organic phases were washed with water (150 mL) and brine (150 mL), dried ($MgSO_4$), filtered, and the solvent removed in vacuo. Purification by column chromatography (silica gel, hexanes/CH_2Cl_2 10:1) afforded **7** (1.3 g, 61%) as a white solid. Mp 142–144 °C. R_f = 0.38 (hexanes/CH_2Cl_2 5:1). IR (CH_2Cl_2 cast): 3064 (m), 3022 (m), 2954 (s), 2867 (s), 2824 (m), 2215 (w), 1599 (m), 1575 (m), 1482 (s), 1445 (s), 1383 (s), 1362 (s), 1265 (s) cm^{-1}; ^1H NMR (498 MHz, $CDCl_3$) δ 7.85 (d, J = 8.0 Hz, 4H), 7.28–7.20 (m, 8H), 7.14–7.10 (m, 4H), 3.32–3.25 (m, 4H), 3.26 (s, 6H), 0.74–0.70 (m, 24H); ^{13}C NMR (126 MHz, $CDCl_3$) δ 148.0, 138.3, 128.3, 128.2, 127.6, 124.9, 113.8, 108.3, 96.2, 85.7, 81.5, 52.1, 28.9, 23.6, 23.4. MALDI MS (DCTB) *m/z* 817.2 ($[M + Na]^+$, 100), 793.1 (M^+, 8), 763.2 ($[M – OMe]^+$, 17), 713.3 ($[M – {}^{81}Br]^+$, 42); MALDI HRMS (DCTB) calcd for $C_{46}H_{50}{}^{79}Br_2NaO_2$ ($[M + Na]^+$) 815.2070, found 815.2077.

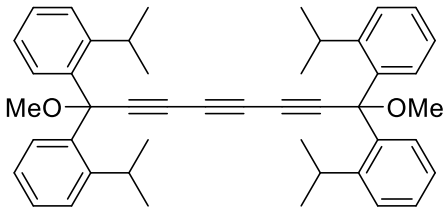

Compound 8: A solution of the alkenyl dibromide **7** (0.54 g, 0.68 mmol) in dry hexanes (15 mL) was cooled to –78 °C under an atmosphere of nitrogen. *n*BuLi (2.5 M in hexanes, 0.33 mL, 0.83 mmol) was added dropwise over a period of 1 min, and the reaction was warmed to rt. After stirring for an additional 30 min, the reaction mixture was cooled to –78 °C and quenched through the addition of satd. aq. NH_4Cl (10 mL). The organic phase was separated, and the aqueous phase was extracted with CH_2Cl_2 (2 × 10 mL). The combined organic phases were washed with brine (25 mL), dried ($MgSO_4$), filtered, and the solvent removed in vacuo. The crude mixture was eluted by column chromatography (silica gel, hexanes/CH_2Cl_2 10:1) to remove the polar impurities and then recrystallized from CH_2Cl_2 (10 mL) and methanol (40 mL) to afford **8** (0.30 g, 69%) as a white powder. Mp 212–214 °C. R_f = 0.41 (hexanes/CH_2Cl_2 5:1). IR (CH_2Cl_2 cast): 3064 (m), 3022 (m), 2955 (s), 2868 (s), 2825 (m), 2209 (vw), 1600 (m), 1575 (m), 1481 (s), 1446 (s), 1314 (s) cm^{-1}; ^1H NMR (700 MHz, $CDCl_3$) δ 7.80 (d, J = 7.6 Hz, 4H), 7.30–7.24 (m, 8H), 7.19–7.16 (m, 4H), 3.30–3.27 (m, 10H), 0.83–0.67 (m, 24H); ^{13}C NMR (176 MHz, $CDCl_3$) δ 148.0, 138.0, 128.6, 128.0, 127.7, 125.1, 81.6, 78.7, 74.0, 64.2, 52.3, 29.0, 23.6, 23.3. MALDI HRMS (DCTB) calcd for $C_{46}H_{50}O_2$ (M^+) 634.3805, found 634.3799.

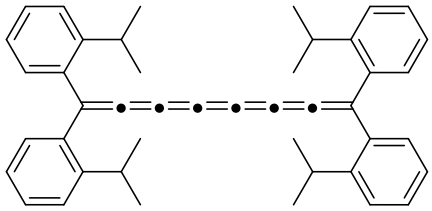

[7]*oi*Pr: To a solution of the oligoyne **8** (50 mg, 0.079 mmol) in CH_2Cl_2 (5 mL) was added $SnCl_2$ (48 mg, 0.25 mmol) and HCl (1.0 M in Et_2O, 0.32 mL, 0.32 mmol). The resulting mixture was stirred for 2 h at 0 °C. The reaction mixture was passed through a plug of basic alumina and eluted with CH_2Cl_2 (20 mL). The resulting solution was concentrated under a flow of nitrogen to a minimum amount (ca. 1.5 mL) and layered with methanol (6 mL) at –30 °C for precipitation, which afforded **[7]*oi*Pr** (26 mg, 57%) as a dark red powder. Mp 88 °C (decomp). R_f = 0.58 (hexanes/CH_2Cl_2 5:1). UV-vis (CH_2Cl_2) λ_{max} (ε) 257 (28600), 297 (69100), 321 (92600), 441 (39000), 511 (60100), 556 (sh, 18500); IR (solid): 3060 (m), 3019 (m), 2963 (s), 2927 (s), 2868 (s), 2056 (w), 1957 (vw), 1920 (vw), 1610 (m), 1481 (s), 1440 (s), 1384 (m), 1363 (m), 1346 (m) cm^{-1}; ^1H NMR (498 MHz, CD_2Cl_2) δ 7.40–7.37 (m, 4H), 7.31 (ddd, J = 8.1, 7.0, 1.6 Hz, 4H), 7.15–7.08 (m, 8H), 3.42 (sept, J = 6.8 Hz, 4H), 1.17 (d, J = 6.8 Hz, 24H); ^{13}C NMR (126 MHz, CD_2Cl_2) δ 154.7, 148.2, 138.6, 130.6, 129.4, 128.7, 128.0, 126.9, 126.1, 124.9, 30.3, 24.1. MALDI HRMS (DCTB) calcd for $C_{44}H_{44}$ (M^+) 572.3438, found 572.3440. DSC: decomposition, 103 °C (onset), 114 °C (peak).

Crystallographic analysis of [3]*oi*Pr and [5]*oi*Pr

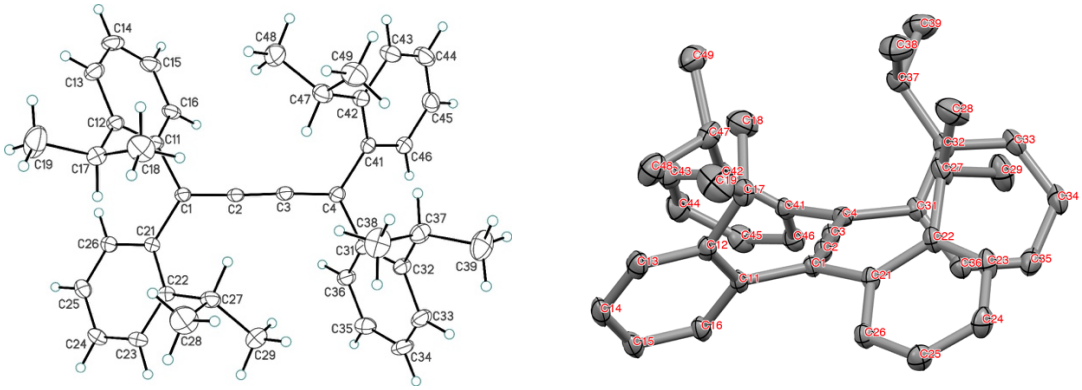

Figure S1. Crystallographic analysis of **[3]*oi*Pr**, top view (left) and end-on view (right). Non-hydrogen atoms are represented by Gaussian ellipsoids at the 30% probability level. Hydrogen atoms are shown with arbitrarily small thermal parameters. Selected bond lengths [Å]: C1–C2 1.335(2), C2–C3 1.255(2), C3–C4 1.335(2). Selected bond angles [°]: C1–C2–C3 177.46(18), C2–C3–C4 176.24(18). Selected torsion bond angles [°]: C2–C1–C11–C12 –128.45(18), C2–C1–C21–C22 39.9(3), C3–C4–C31–C32 –118.37(19), C3–C4–C41–C42 44.4(3).

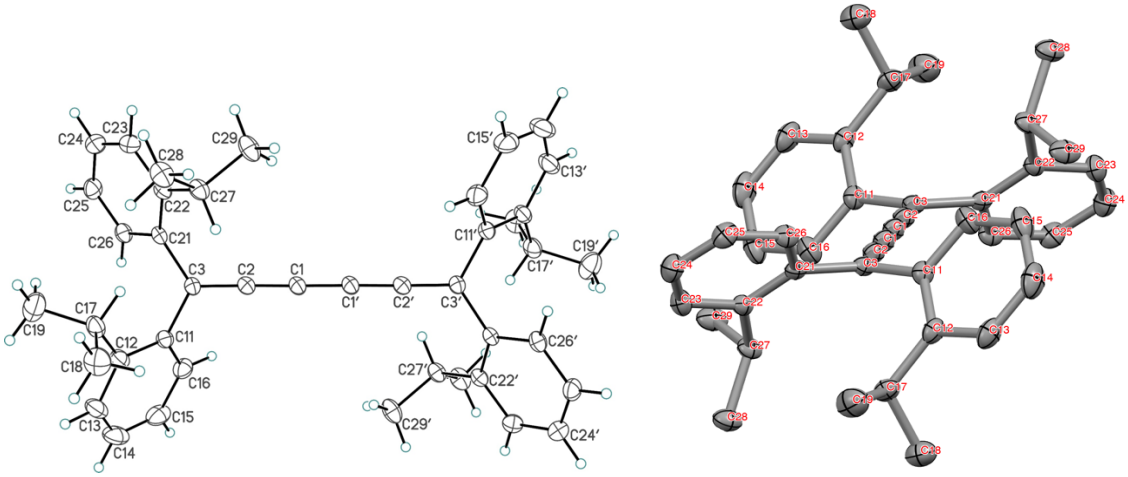

Figure S2. Crystallographic analysis of **[5]*oi*Pr**, top view (left) and end-on view (right). Non-hydrogen atoms are represented by Gaussian ellipsoids at the 30% probability level. Hydrogen atoms are shown with arbitrarily small thermal parameters. Selected bond lengths [Å]: C3–C2 1.334(3), C2–C1 1.260(3), C1–C1' 1.298(4). Selected bond angles [°]: C3–C2–C1 178.8(2), C2–C1–C1' 179.0(3). Selected torsion bond angles [°]: C2–C3–C11–C12 123.5(2), C2–C3–C21–C22 –46.9(3).

^{1}H and ^{13}C NMR spectra for new compounds

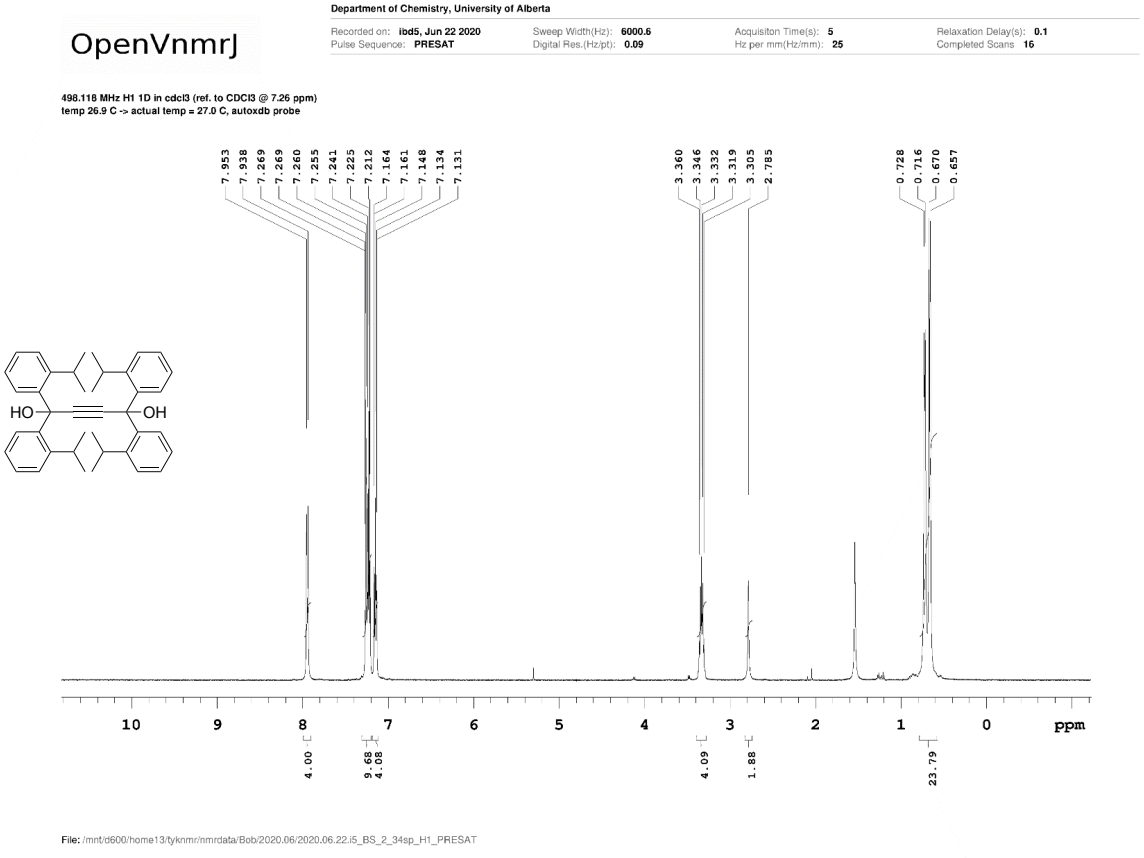

Figure S3. ^{1}H NMR spectrum of compound **1** in $CDCl_3$.

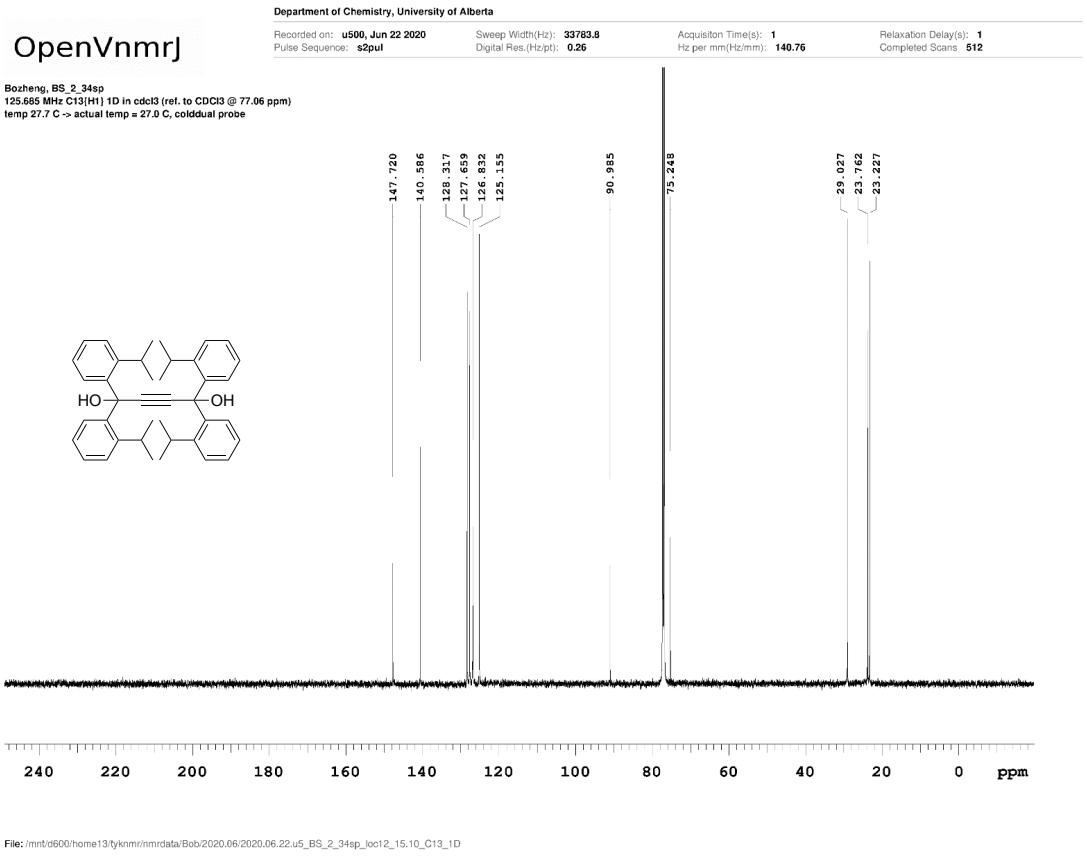

Figure S4. ^{13}C NMR spectrum of compound **1** in $CDCl_3$.

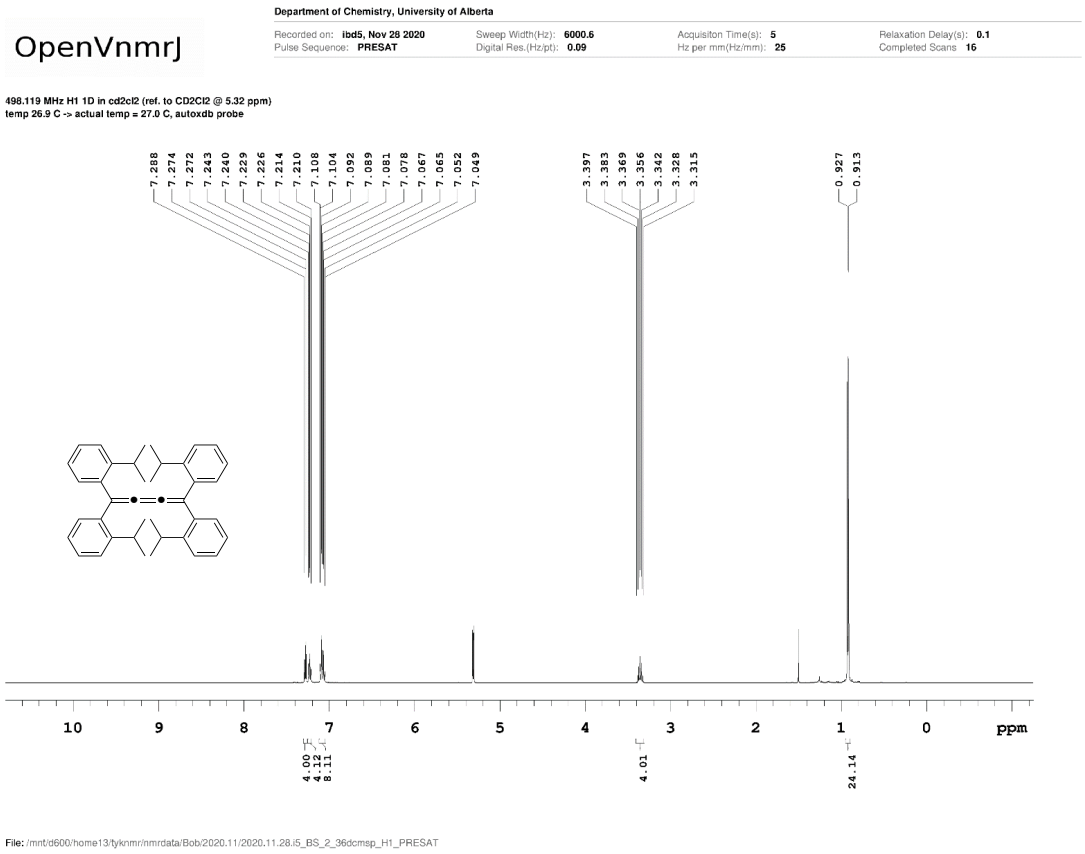

Figure S5. ^{1}H NMR spectrum of compound **[3]*oi*Pr** in CD_2Cl_2.

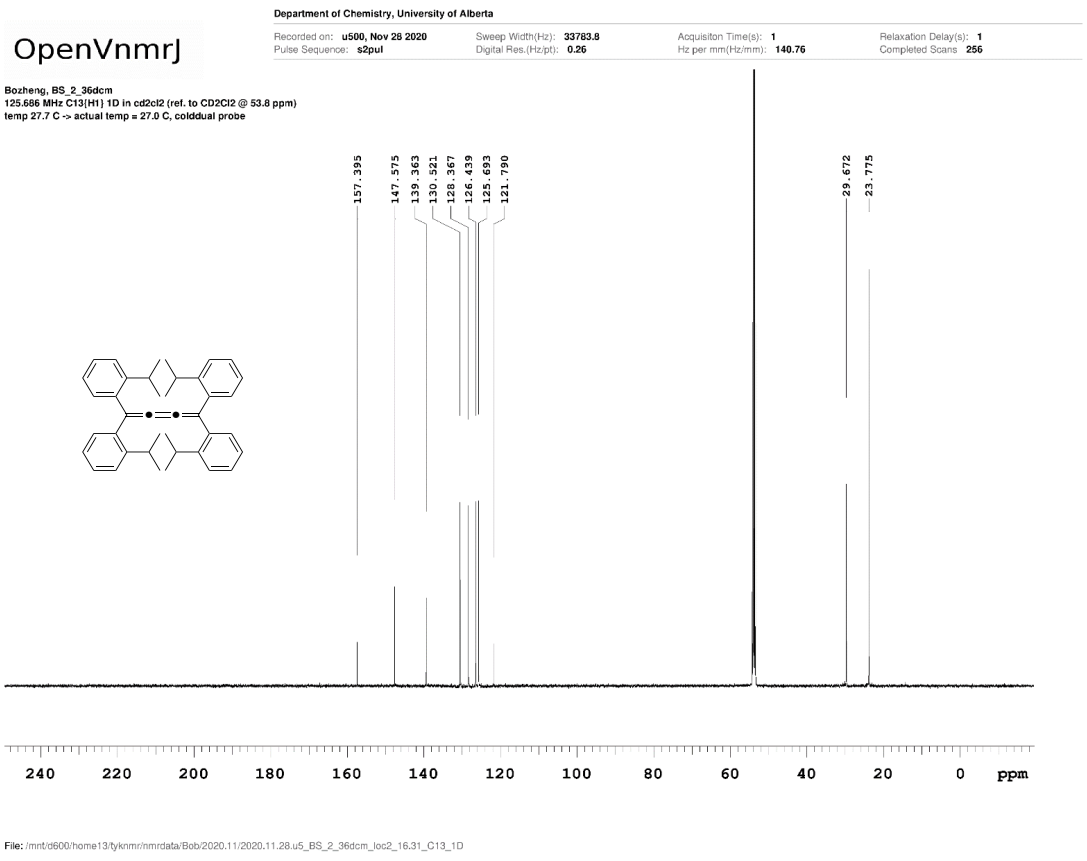

Figure S6. ^{13}C NMR spectrum of compound **[3]*oi*Pr** in CD_2Cl_2.

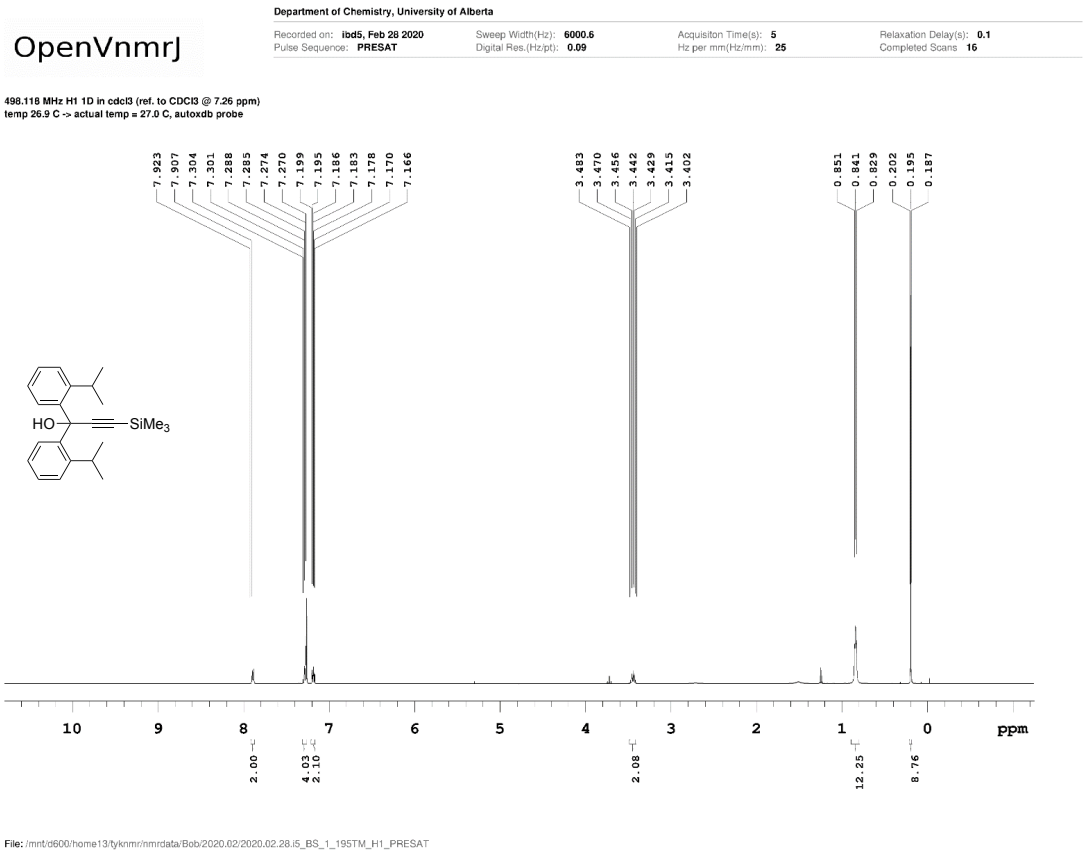

Figure S7. ^{1}H NMR spectrum of compound **2** in $CDCl_3$.

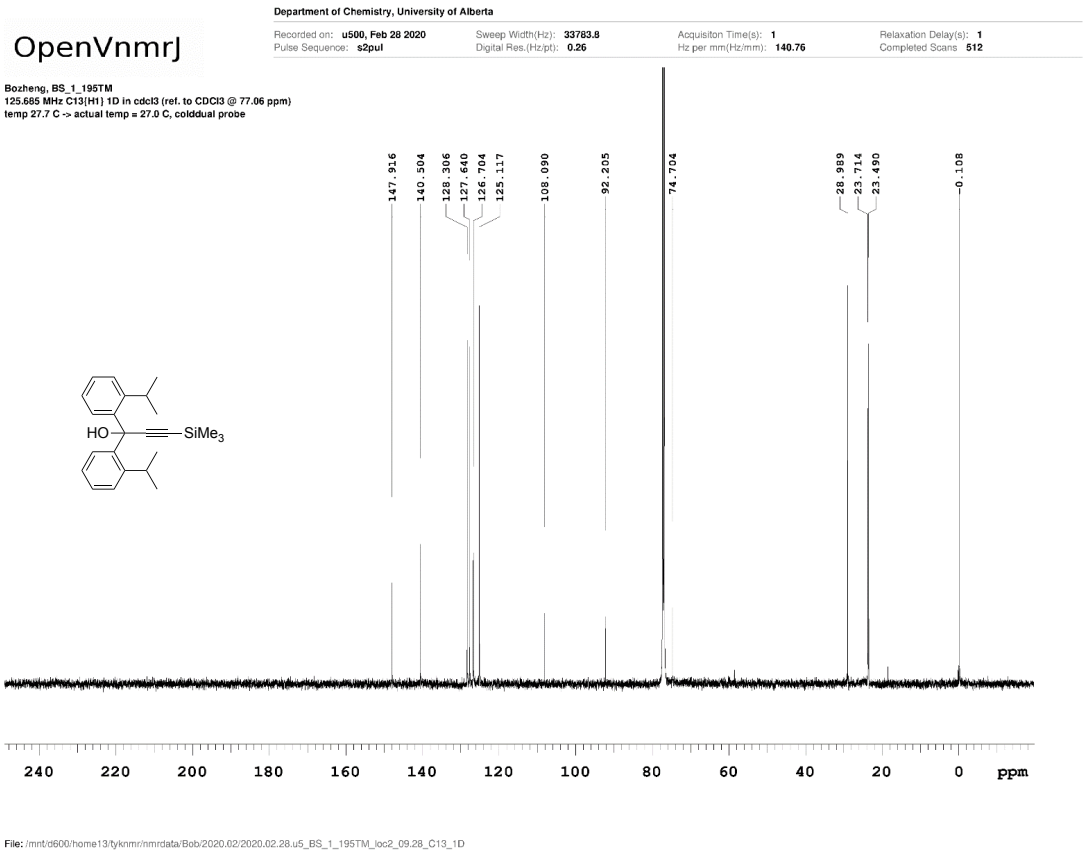

Figure S8. ^{13}C NMR spectrum of compound **2** in $CDCl_3$.

Figure S9. ^{1}H NMR spectrum of compound **3** in $CDCl_3$.

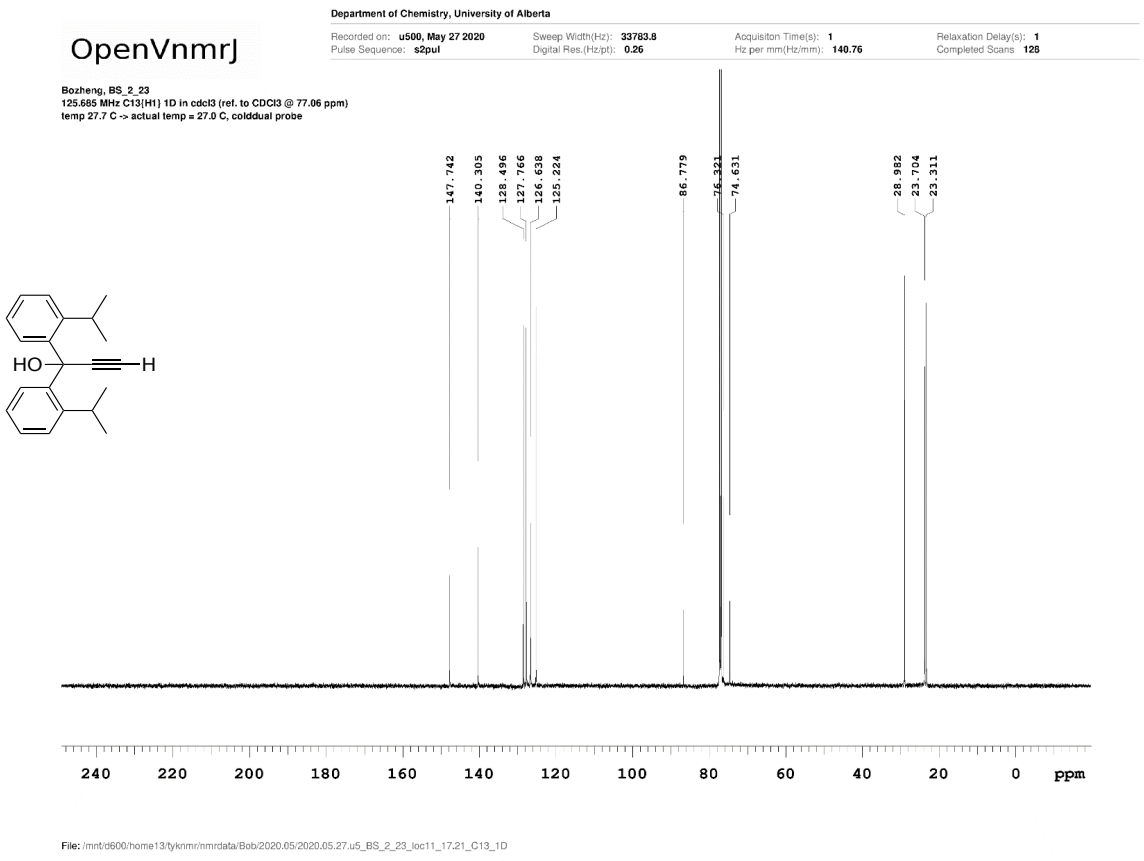

Figure S10. ^{13}C NMR spectrum of compound **3** in $CDCl_3$.

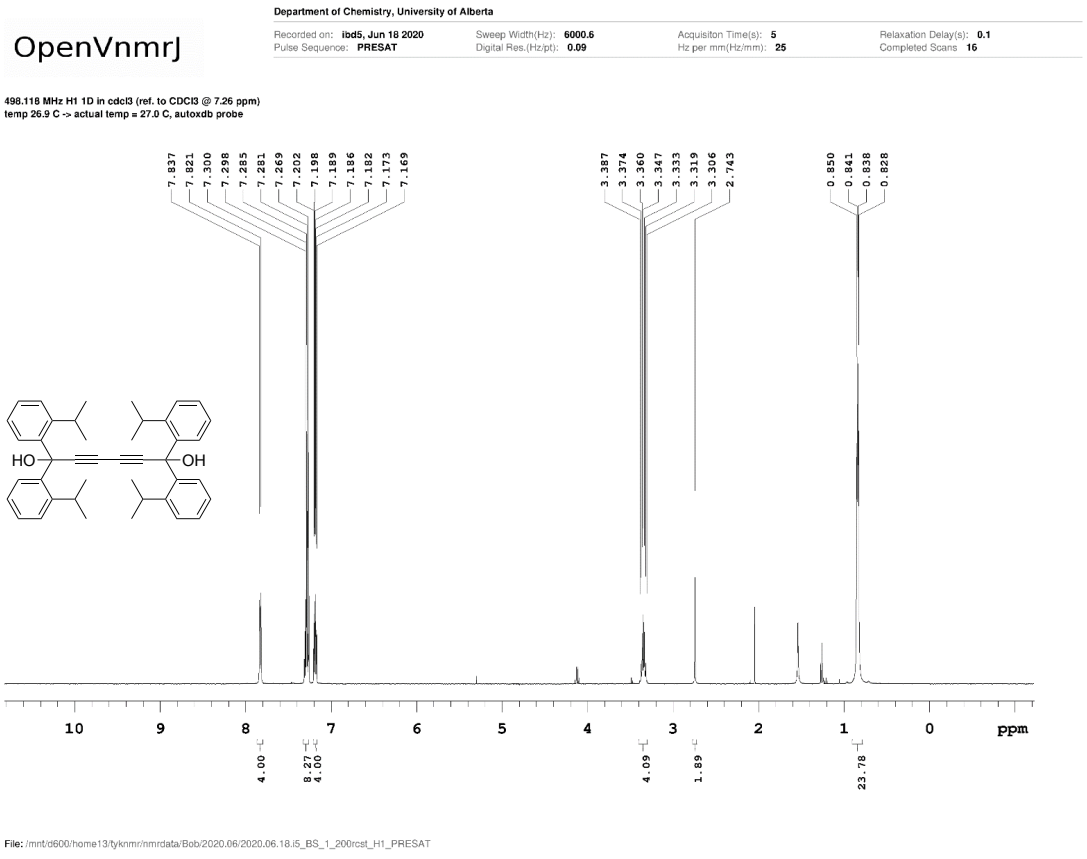

Figure S11. ^{1}H NMR spectrum of compound **4** in $CDCl_3$.

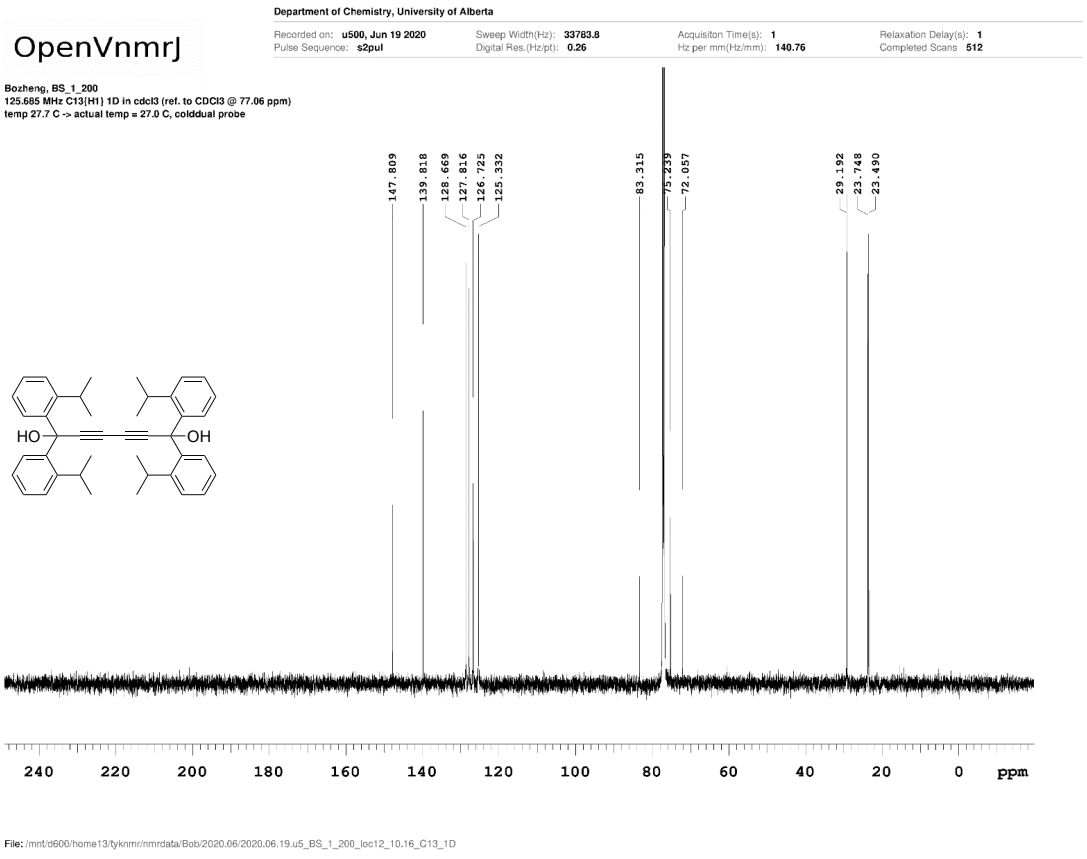

Figure S12. ^{13}C NMR spectrum of compound **4** in $CDCl_3$.

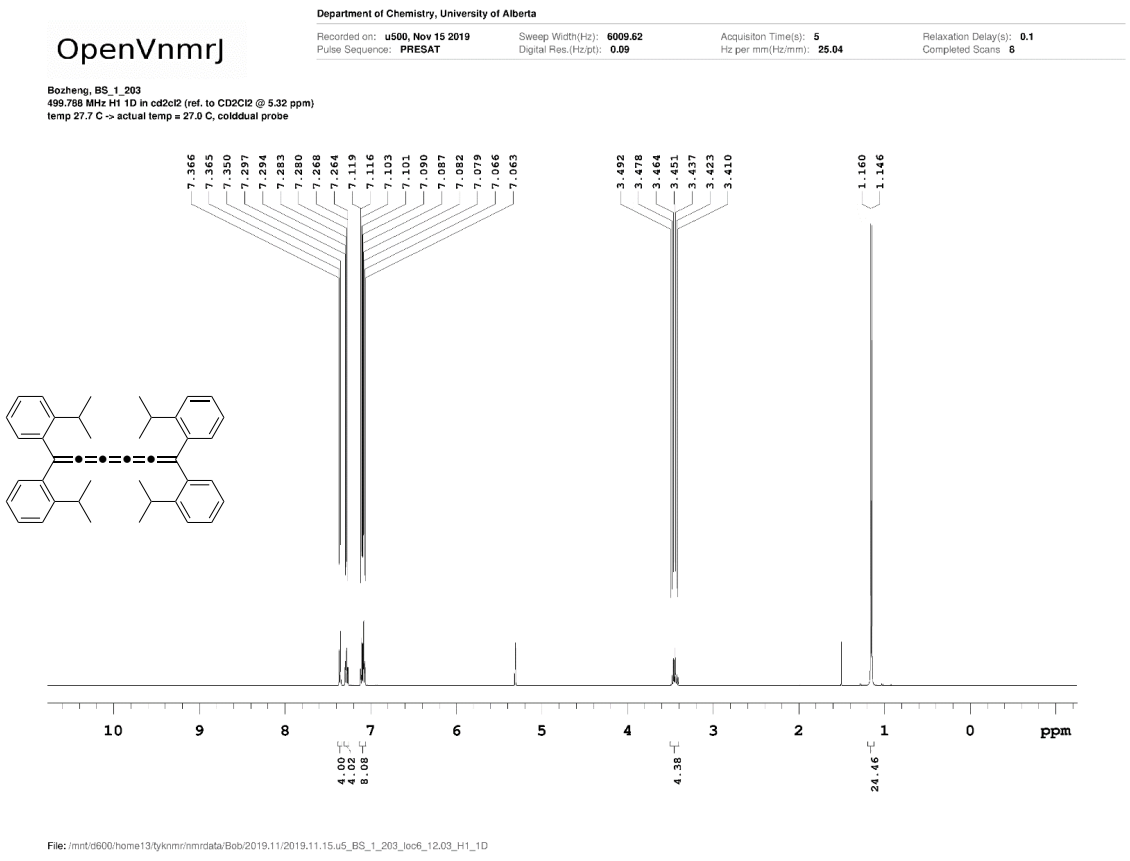

Figure S13. ^{1}H NMR spectrum of compound **[5]*oi*Pr** in CD_2Cl_2.

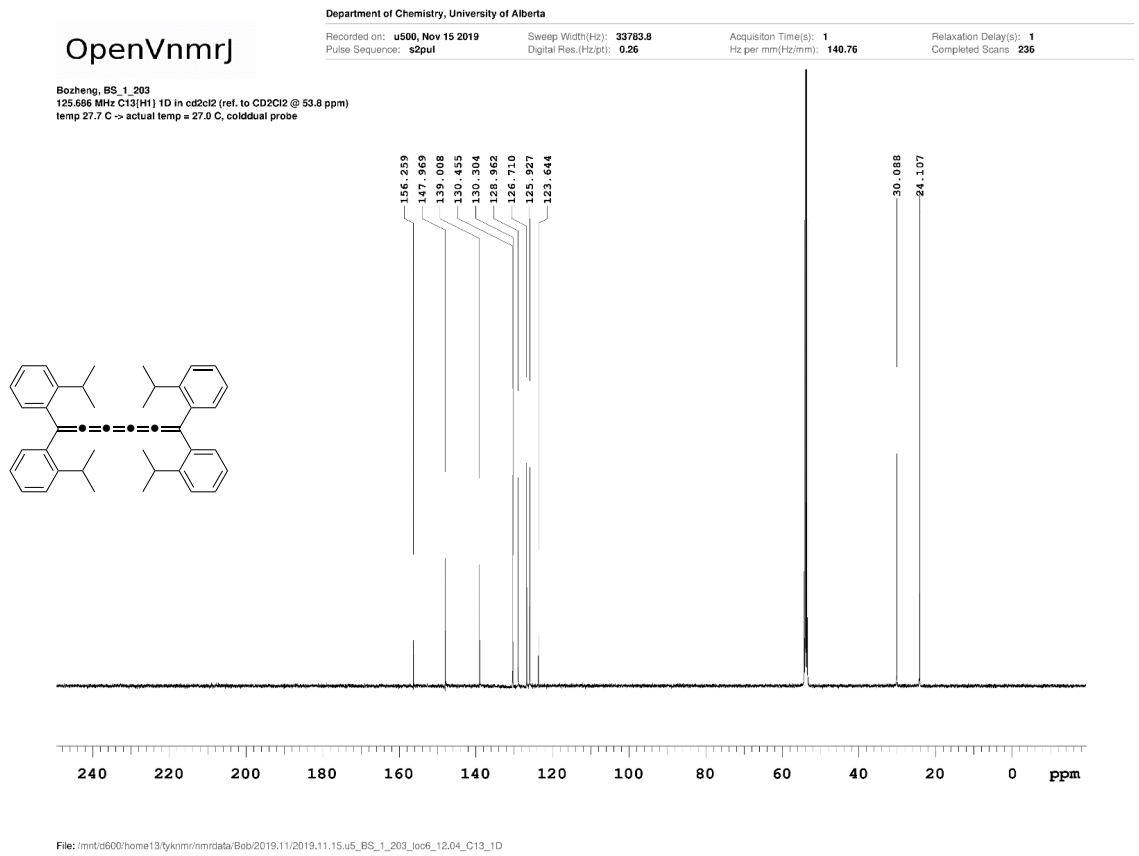

Figure S14. ^{13}C NMR spectrum of compound **[5]*oi*Pr** in CD_2Cl_2.

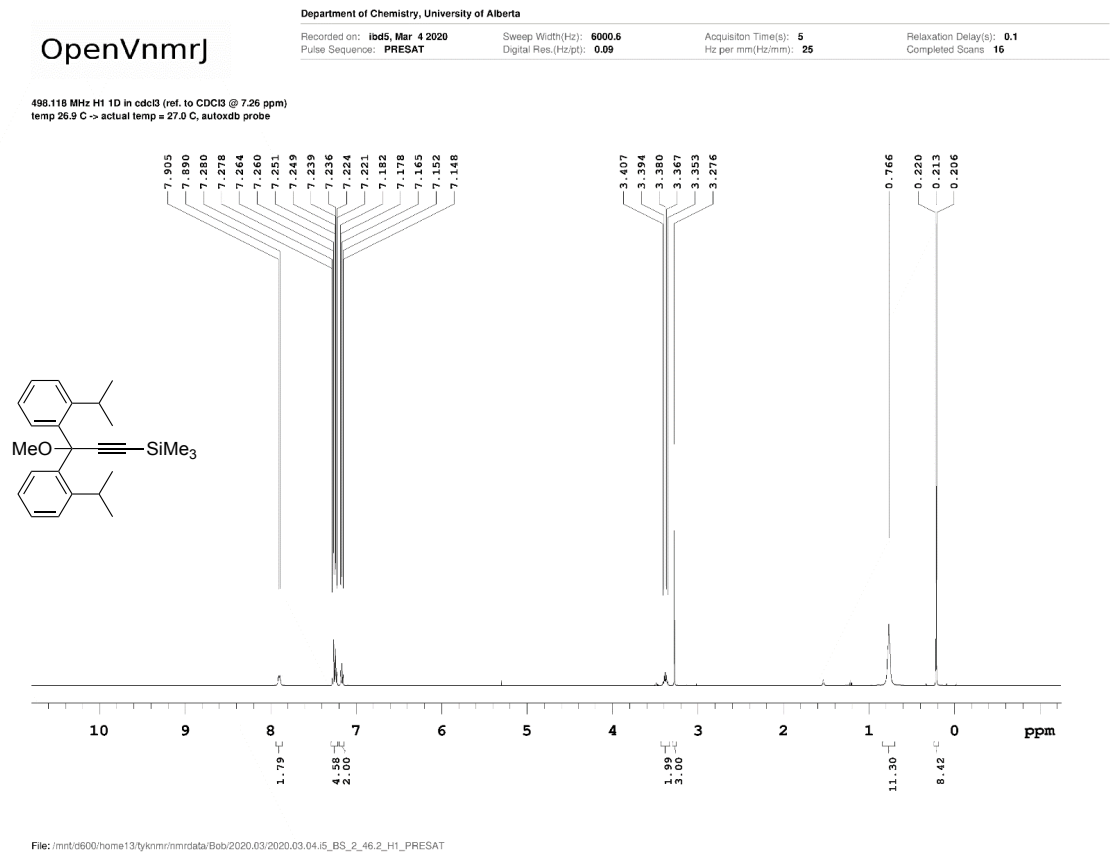

Figure S15. ^{1}H NMR spectrum of compound **S1** in $CDCl_3$.

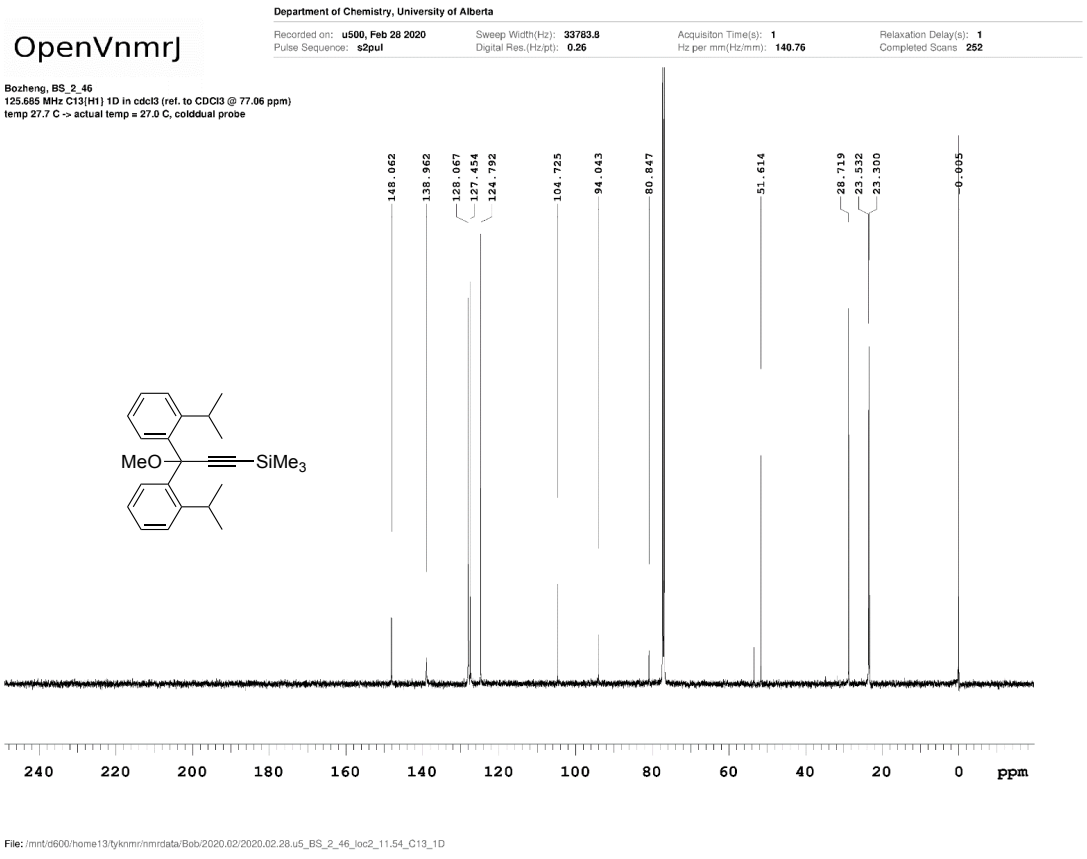

Figure S16. ^{13}C NMR spectrum of compound **S1** in $CDCl_3$.

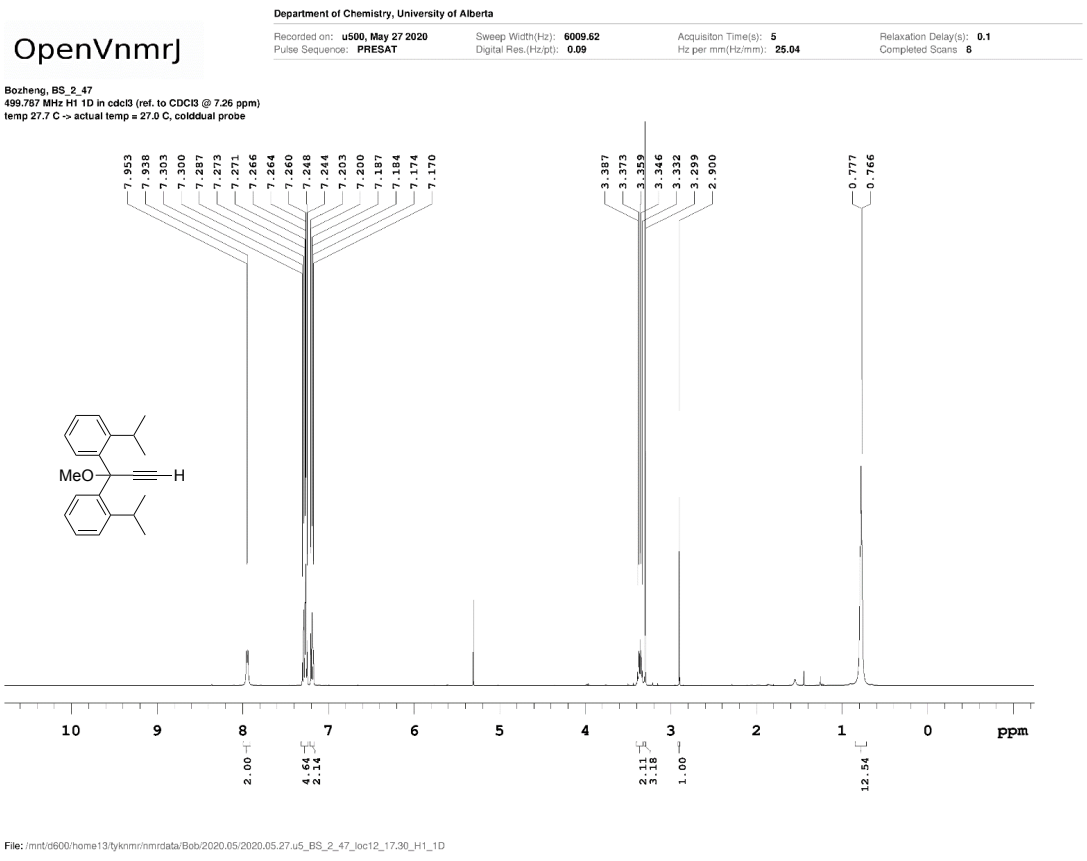

Figure S17. ^{1}H NMR spectrum of compound **5** in $CDCl_3$.

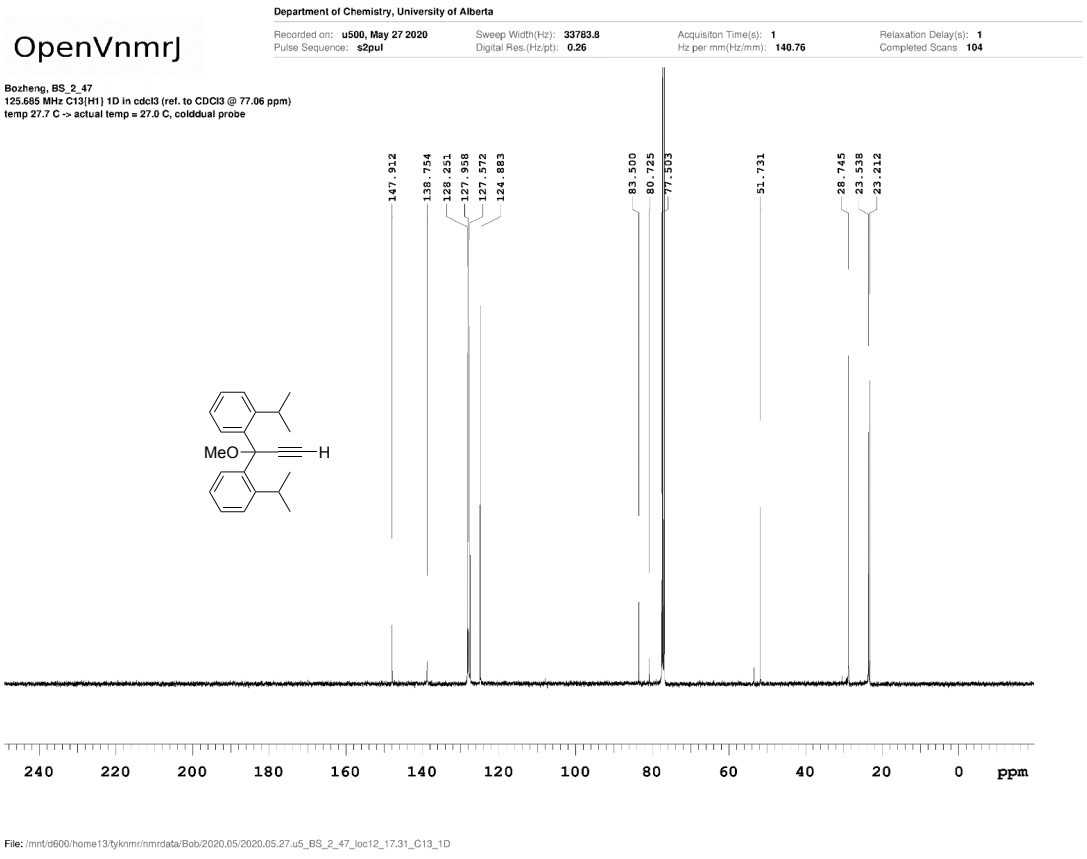

Figure S18. ^{13}C NMR spectrum of compound **5** in $CDCl_3$.

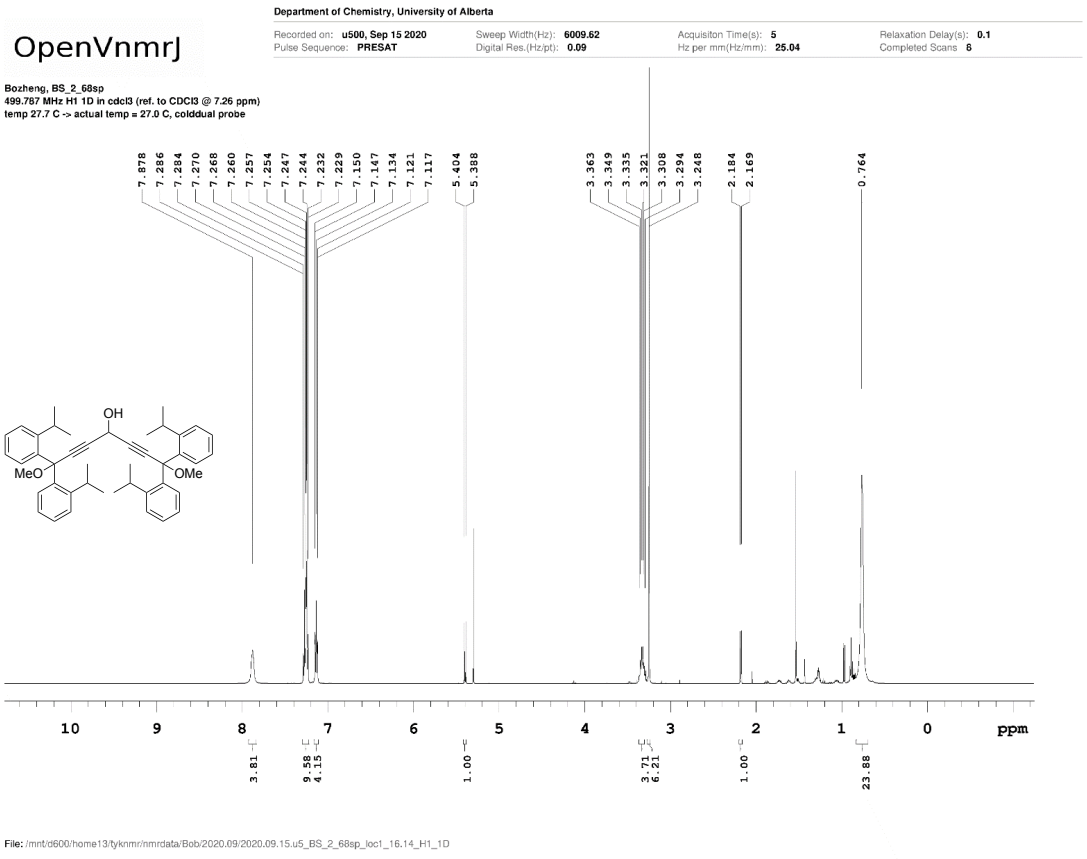

Figure S19. ^{1}H NMR spectrum of compound **S2** in $CDCl_3$.

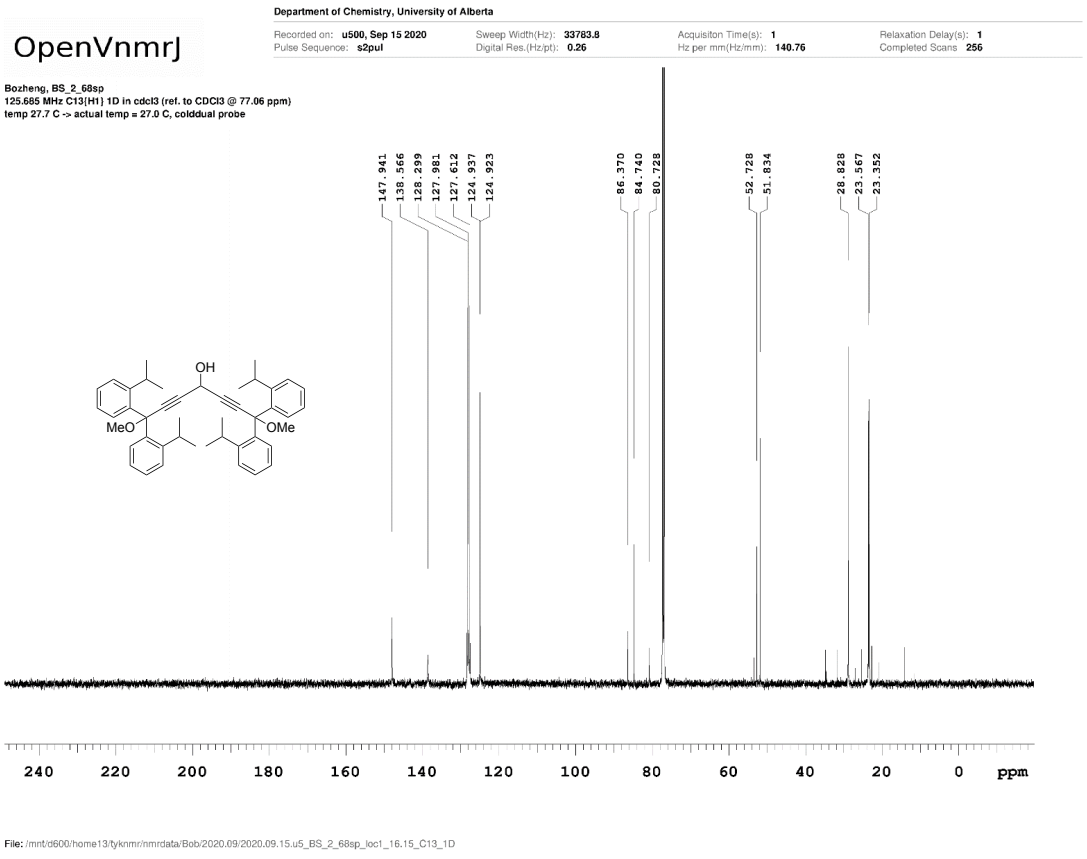

Figure S20. ^{13}C NMR spectrum of compound **S2** in $CDCl_3$.

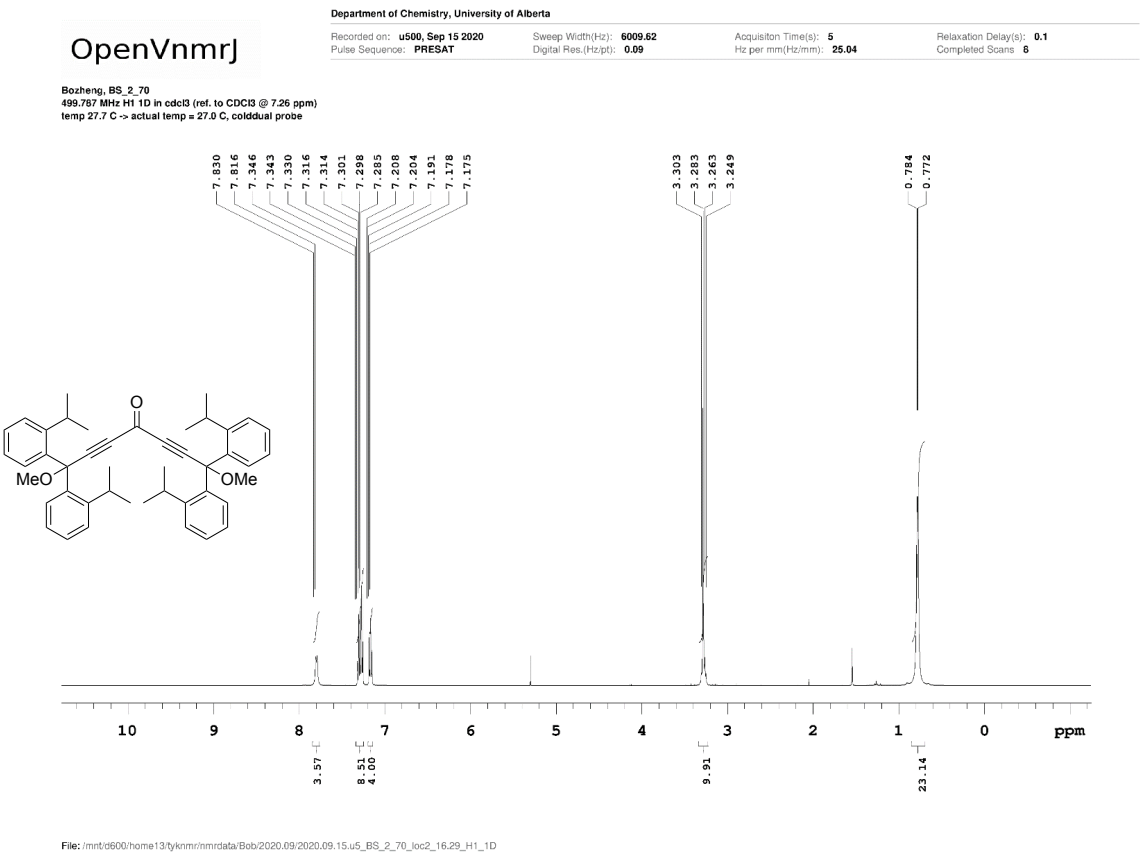

Figure S21. ^{1}H NMR spectrum of compound **6** in $CDCl_3$.

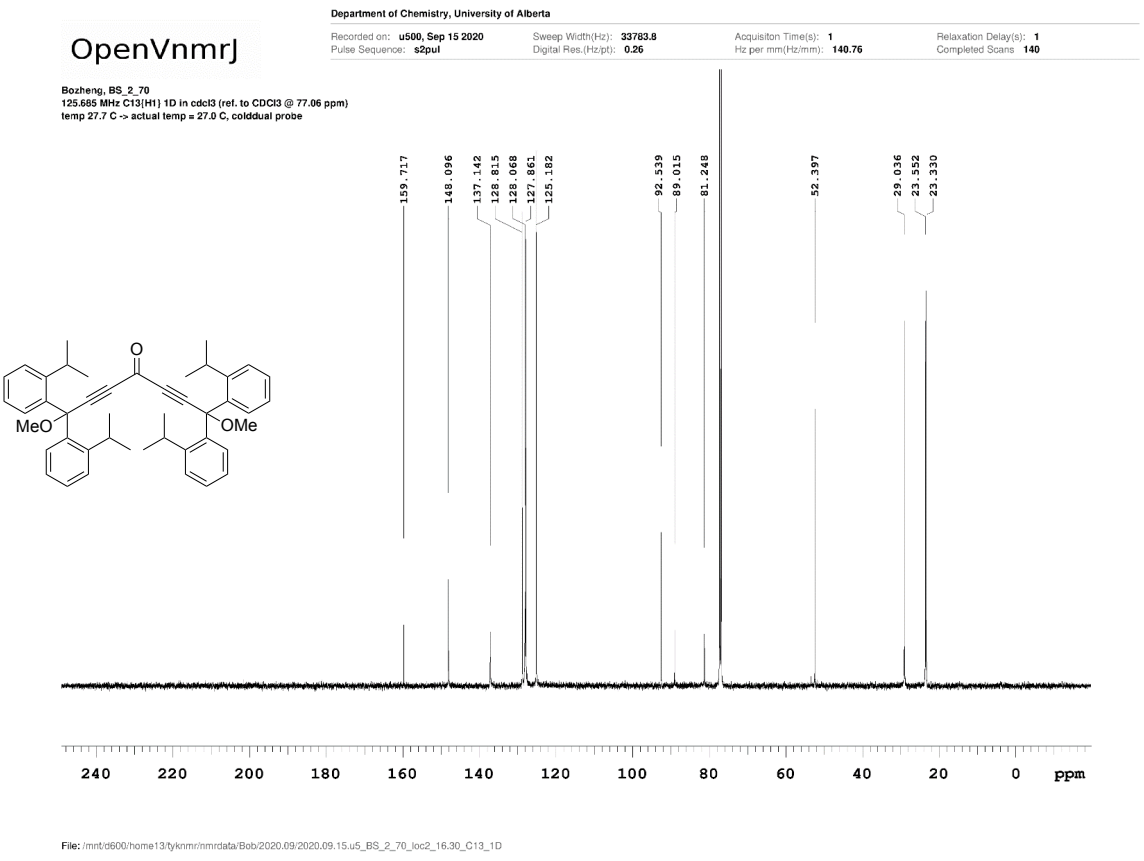

Figure S22. ^{13}C NMR spectrum of compound **6** in $CDCl_3$.

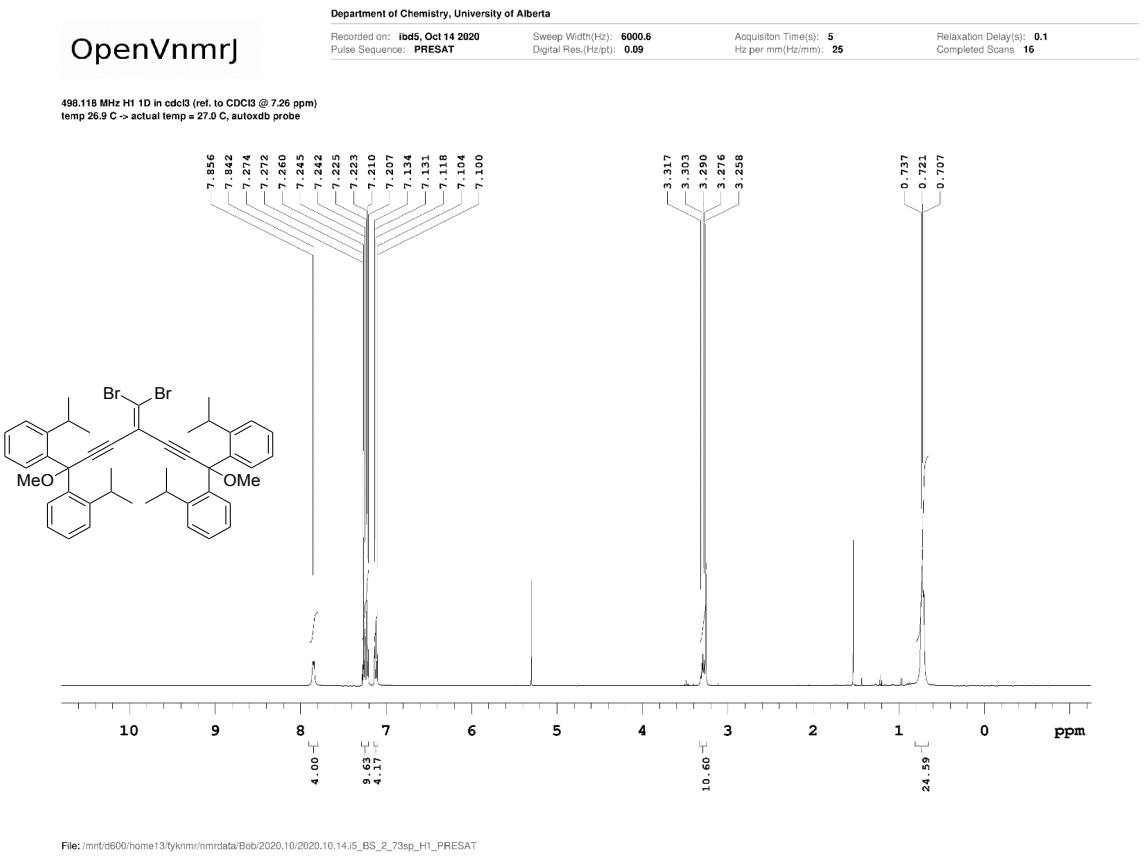

Figure S23. ^{1}H NMR spectrum of compound **7** in $CDCl_3$.

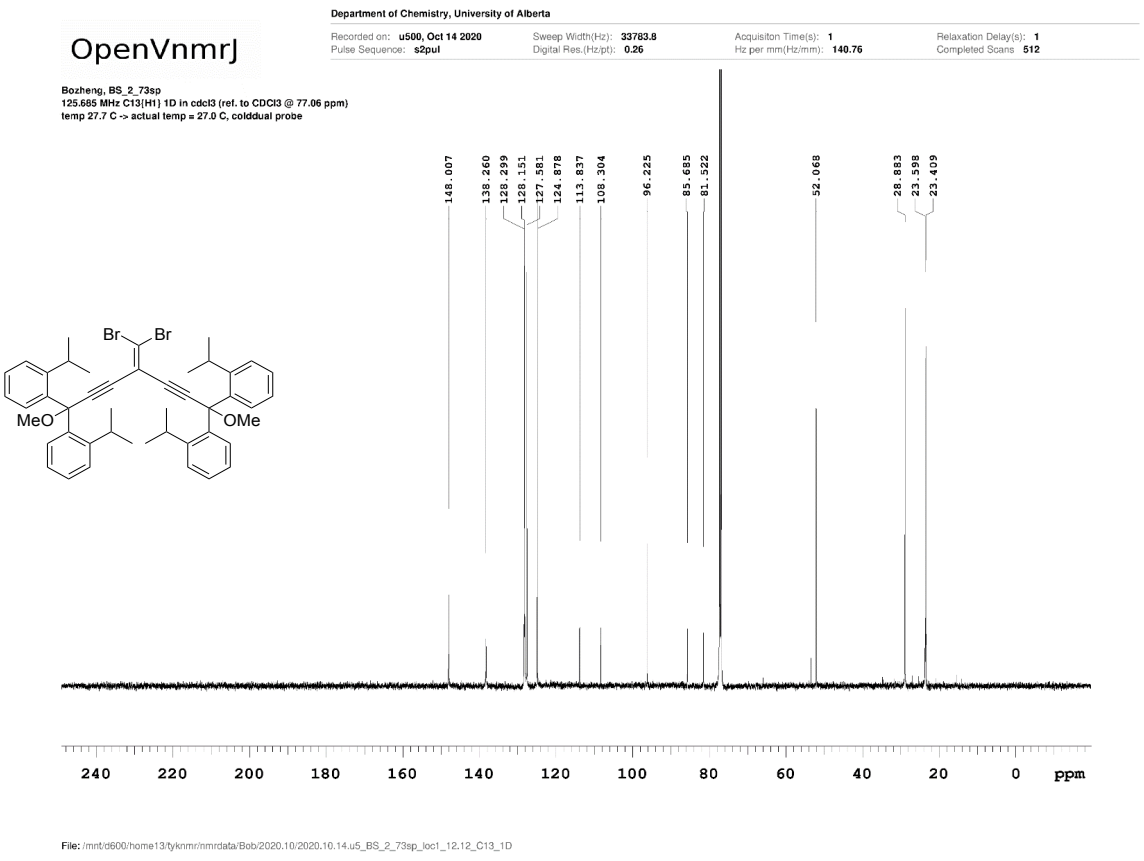

Figure S24. ^{13}C NMR spectrum of compound **7** in $CDCl_3$.

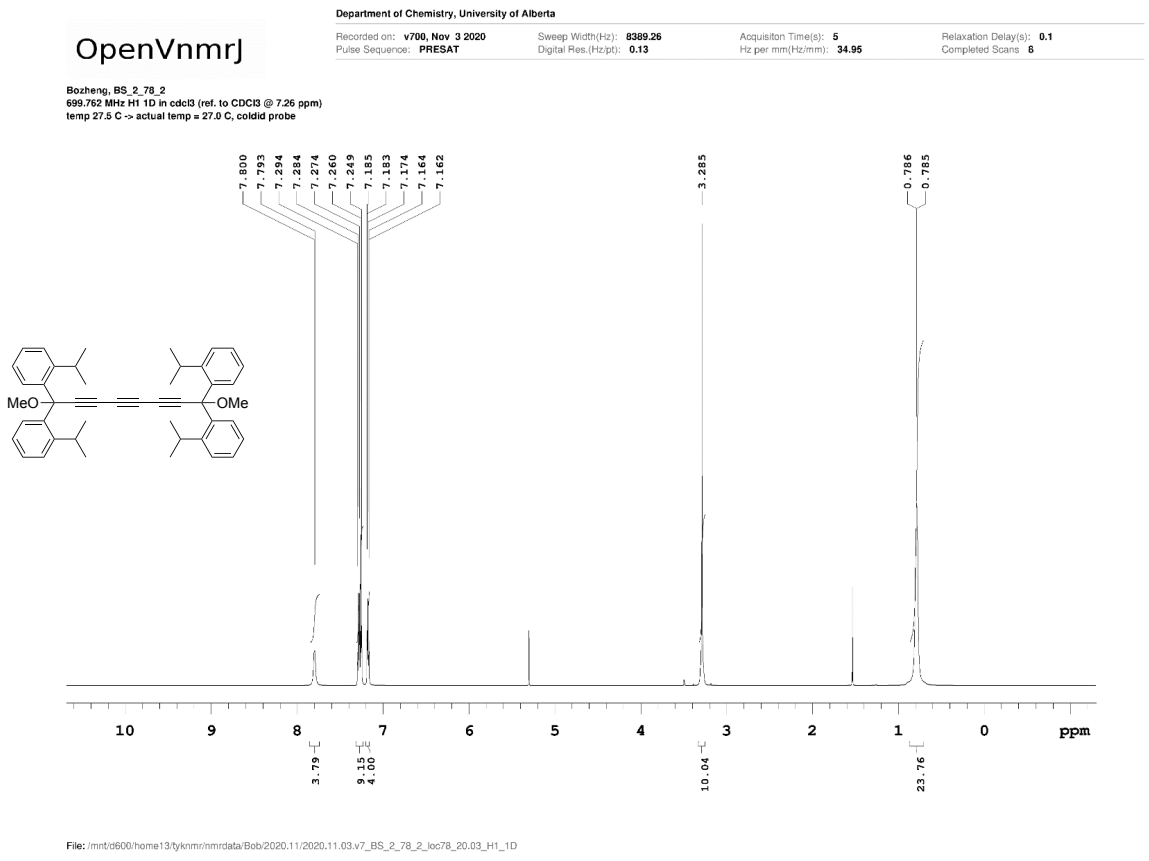

Figure S25. ^{1}H NMR spectrum of compound **8** in $CDCl_3$.

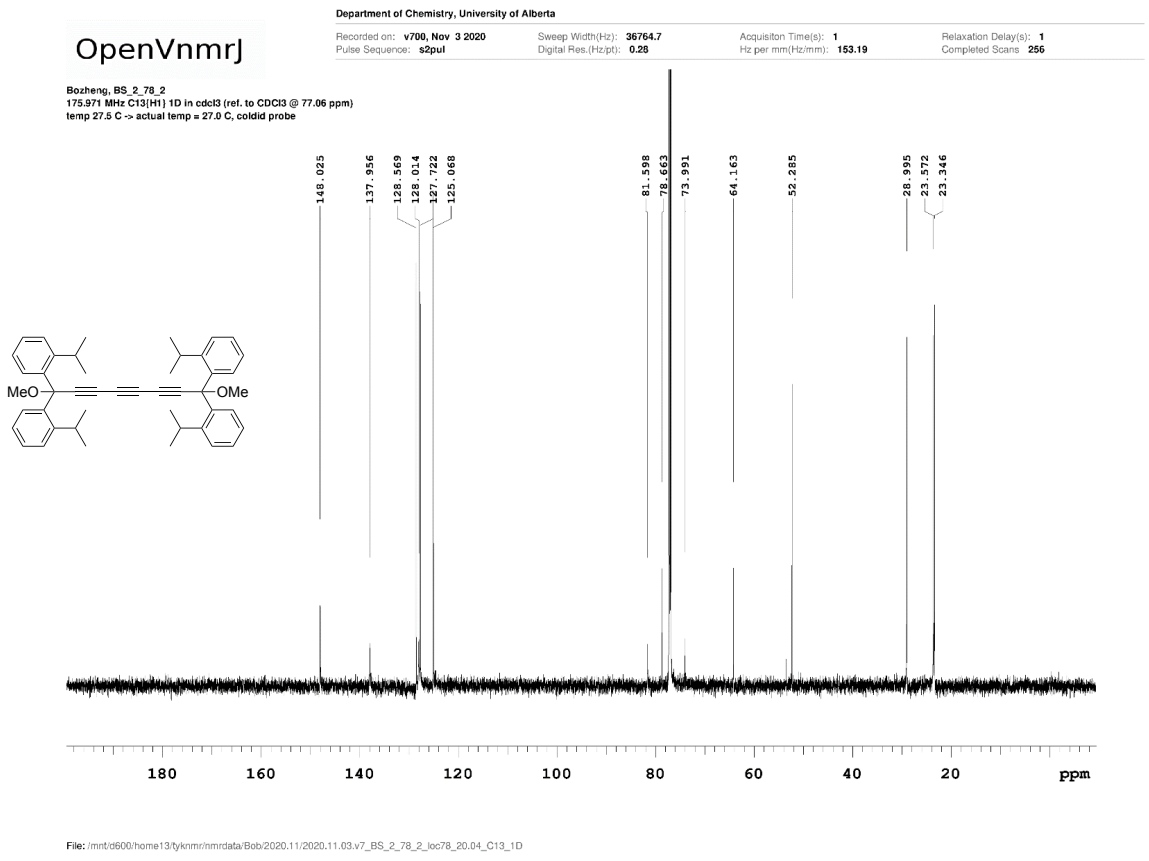

Figure S26. ^{13}C NMR spectrum of compound **8** in $CDCl_3$.

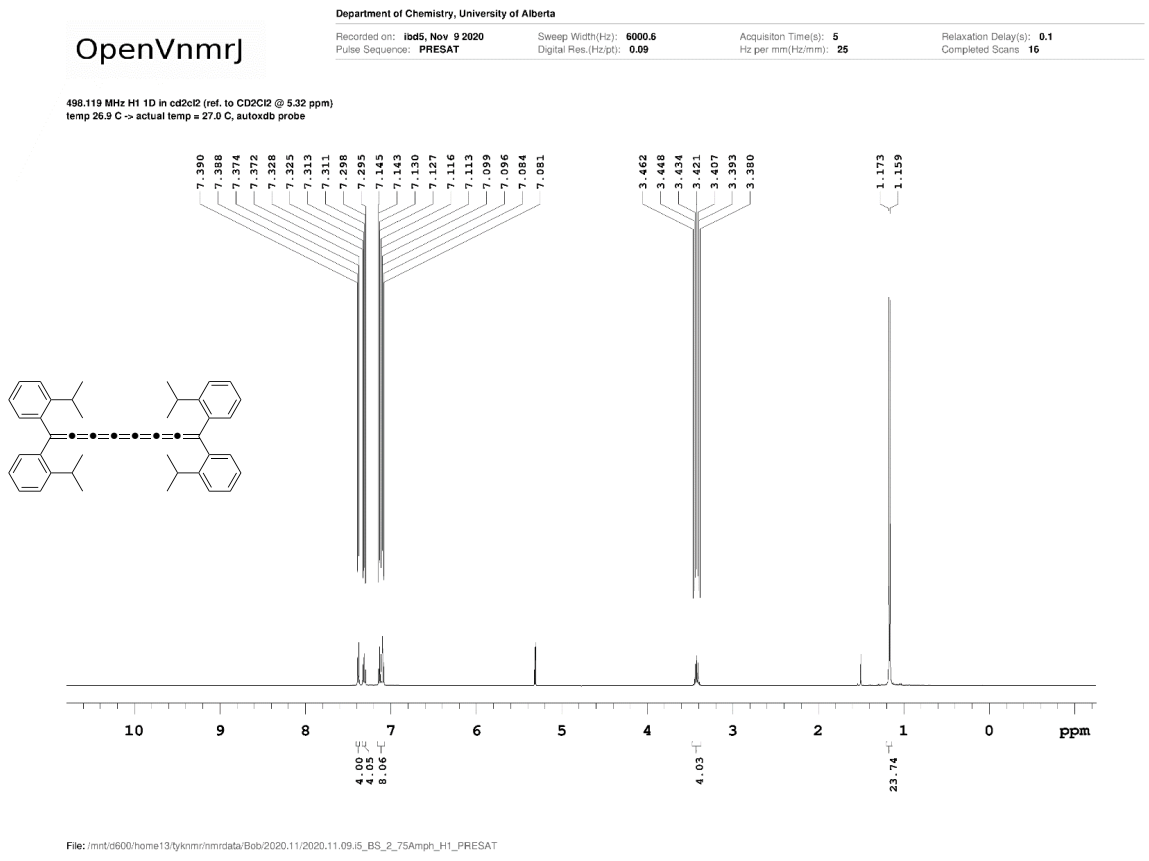

Figure S27. ^{1}H NMR spectrum of compound **[7]*oi*Pr** in CD_2Cl_2.

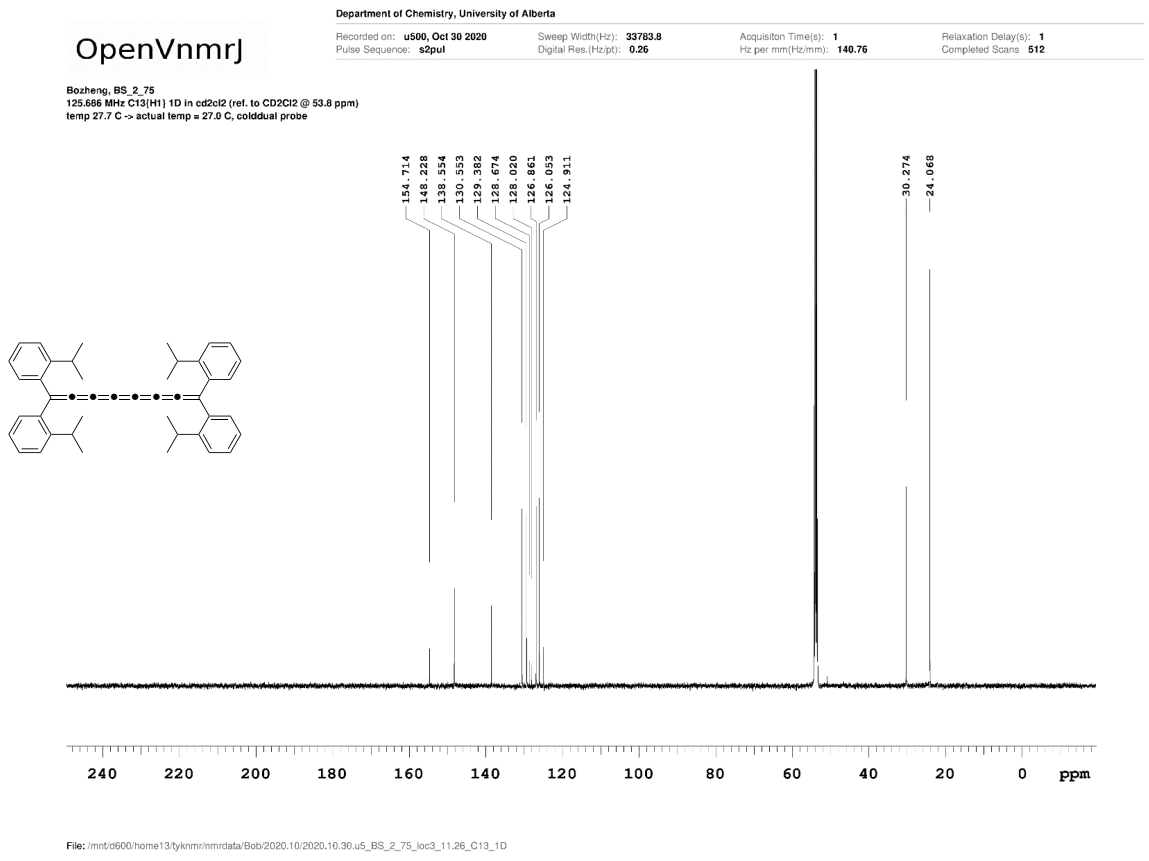

Figure S28. ^{13}C NMR spectrum of compound **[7]*oi*Pr** in CD_2Cl_2.

Spectroscopic Investigations

General Methods

Throughout all photophysical experiments, 3-methylpentane was used as solvent, since it forms an optical transparent glass at cryogenic temperatures. For temperature dependent measurements, quartz cuvettes were placed in a liquid dinitrogen cryostat Optistat DN from Oxford Instruments. All samples were degassed with argon for 15 minutes prior to each experiment.

Steady state absorption spectra were recorded by using a Varian Cary 5000 spectrometer. Steady-state emission spectra were acquired using an FS5 spectrofluorometer from Edinburgh Instruments.

FT-IR measurements were performed in a Shimadzu Prestige 21 equipped with an ATR unit. Raman spectra were acquired with a WiTec alpha 300r confocal Raman microscope using a HeNe Laser with an output of 633 nm for sample excitation to avoid fluorescence background.

Emission lifetimes and ns time resolved emission spectroscopy (TRES) were measured using a Fluorolog 3 time-correlated single photon counting (TCSPC) instrument from Horiba Jovin Yvon, a SuperK Fianium FIU6PP supercontinuum laser from NKT Photonics as the excitation source, and a R3809U-50 MCP photomultiplier from Hammamatsu.

All fs- and ns-TA spectra were carried out with an amplified Ti:Sapphire CPA 2110 fs laser system from Clark MXR, Inc. (central wavelength 775 nm, repetition rate 1 kHz, 150 fs pulse duration) using a customized TA pump/probe detection system (Ultrafast systems: Helios, Eos). The excitation pulses were generated via a home-built non-collinear parametric amplifier (NOPA) and second harmonic generation. Energy per pulse was reduced to 200 and 500 nJ, respectively. The concentration was chosen to achieve an optical density of around 0.2 in the spectral region of the excitation wavelength, if not mentioned otherwise. Triplet sensitization experiments were performed with anthracene, purchased from a common supplier and further purified by sublimation. All fs- and ns-TA data were fitted via global analysis, performed with the open-source software package GloTarAn. Therefore, a sequential kinetic model was applied to fit the data. The dispersion of the instrument response function was modeled and taken into account. In the case of **[7]*oi*Pr**, the fs-TA data were modelled by applying a target analysis to account for the parallel deactivation from S_3 into S_2 and S_1.

Transient IR spectroscopy was performed using an Astrella-F-1K Ti:Sa amplifier from Coherent, Inc. (5 mJ pulse energy, 1 kHz repetition rate, 800 nm central wavelength, 80 fs pulse duration). A fraction of 1.2 mJ was used for pump beam generation by a Topas Prime with standard NirUVis extension module from Light Conversion. Another fraction of 3.0 mJ was guided through a delay line from Ultrafast, Inc. providing a temporal time window between pump and probe beam of 8 ns. Afterwards, the IR probe pulse was generated by a Topas Prime with nDFG extension module from Light Conversion. Both visible pump and IR probe beam were guided into a commercial Helios IR spectrometer from Ultrafast, Inc. Inside the transient IR spectrometer the IR probe pulse was divided in a reference and probe beam, which are detected by nitrogen cooled 32 x 2 pixel MCT detector. Before each transient IR experiment the Helios IR spectrometer and the optical path of the IR probe pulse were purged with argon for 30 min. The sample (concentration of around 1 mM to achieve an optical density of 1.0 in

water and oxygen free 3-methylpentane) was prepared in a home-built IR cell using two CaF_2 windows and a Teflon spacer of 250 μm. Pump pulse energy was reduced to 1.5 μJ and a depolarizer was placed in the pump beam to average rotational dynamics.

Temperature- and excitation-dependent steady-state emission spectroscopy

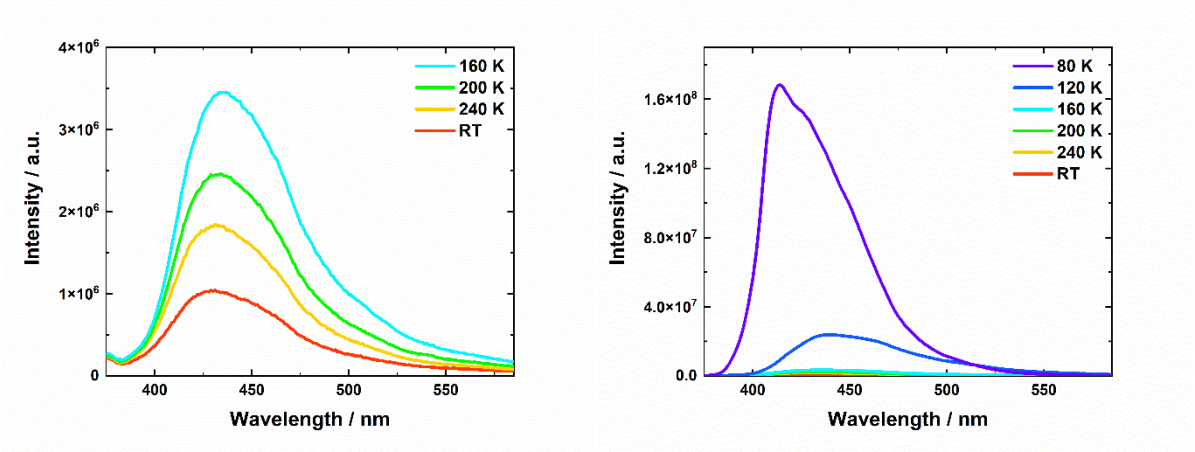

Figure S29. Temperature dependent steady-state emission spectra of **[3]*oi*Pr** (c = $2.5 \cdot 10^{-6}$ M) obtained upon photoexcitation at 340 nm.

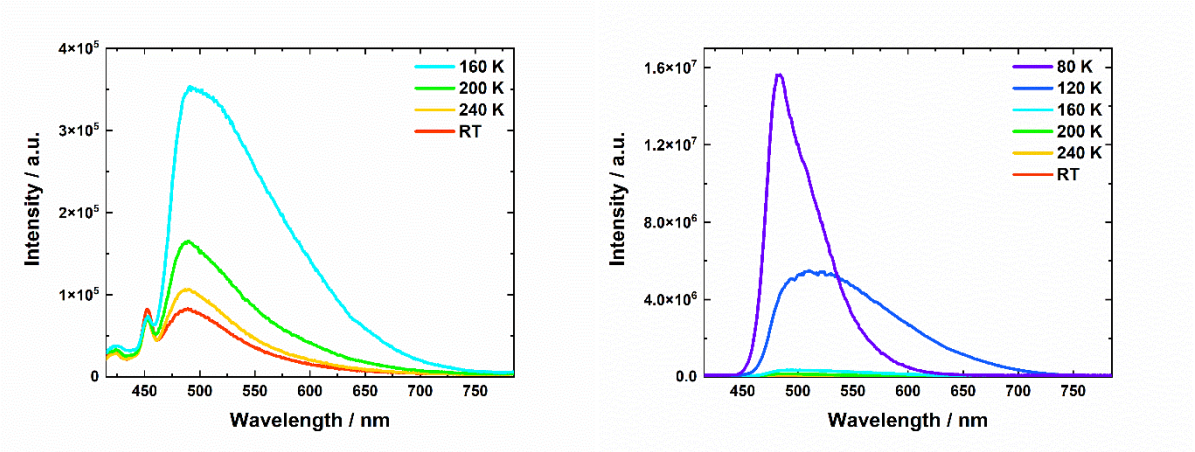

Figure S30. Temperature dependent steady-state emission spectra of **[5]*oi*Pr** (c = $2.5 \cdot 10^{-6}$ M) obtained upon photoexcitation at 340 nm.

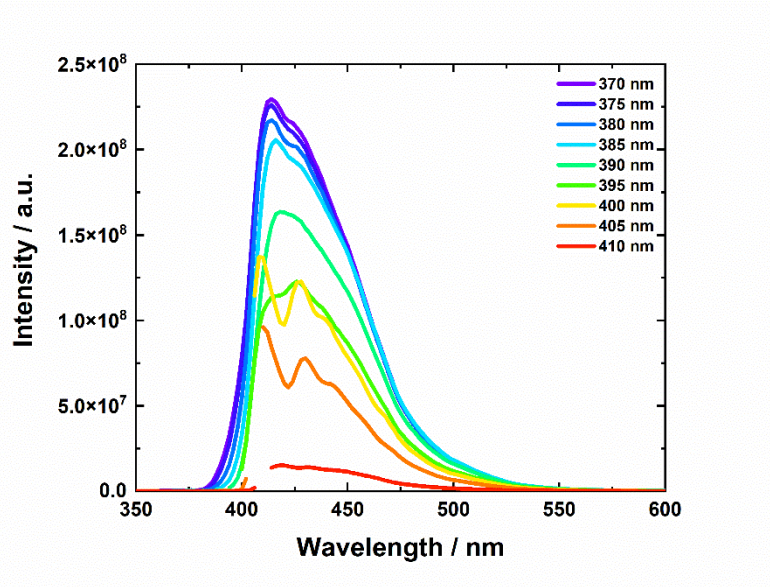

Figure S31. Excitation dependent steady-state emission spectra of **[3]*oi*Pr** (c = $2.5 \cdot 10^{-6}$ M) obtained at 80 K.

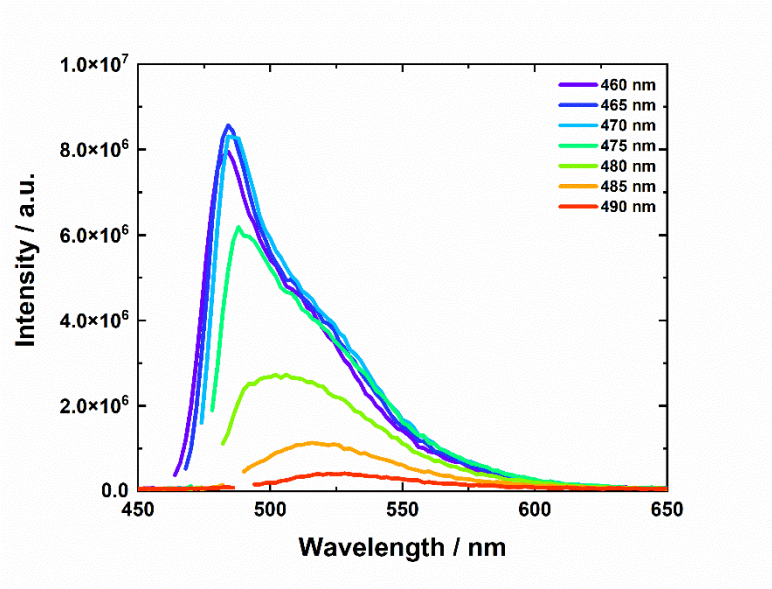

Figure S32. Excitation dependent steady-state emission spectra of **[5]*oi*Pr** ($c = 2.5 \cdot 10^{-6}$ M) obtained at 80 K.

Nanosecond time-resolved emission spectroscopy (TRES)

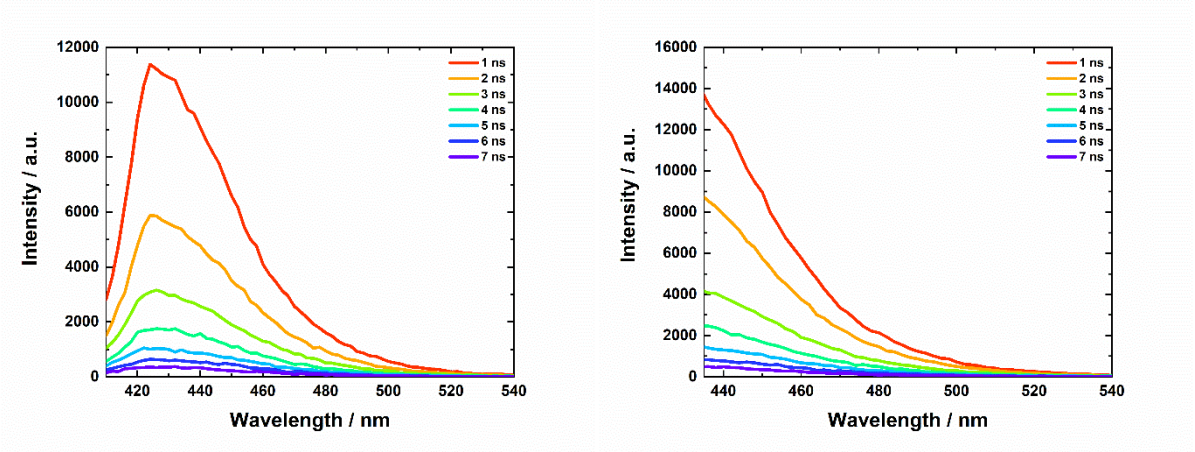

Figure S33. Selected ns time resolved fluorescence spectra at various deactivation/delay times for **[3]*oi*Pr** (c = $2.5 \cdot 10^{-6}$ M) with photoexcitation at 400 nm (left) and 420 nm (right) at 80 K.

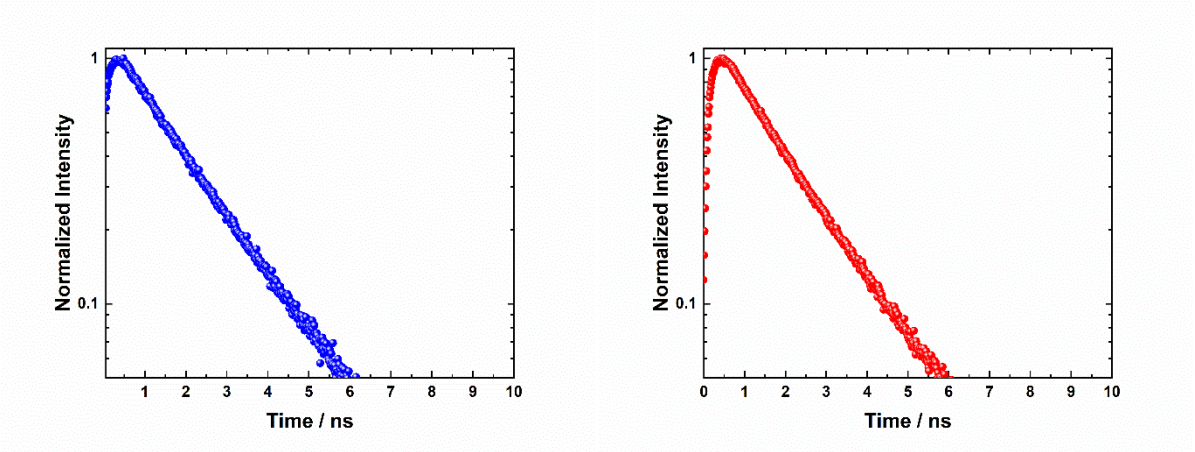

Figure S34. Normalized kinetic traces obtained at 450 nm emission wavelength by ns time resolved fluorescence spectroscopy experiments for **[3]*oi*Pr** ($c = 2.5 \cdot 10^{-6}$ M) with photoexcitation at 400 nm (left) and 420 nm (right) at 80 K.

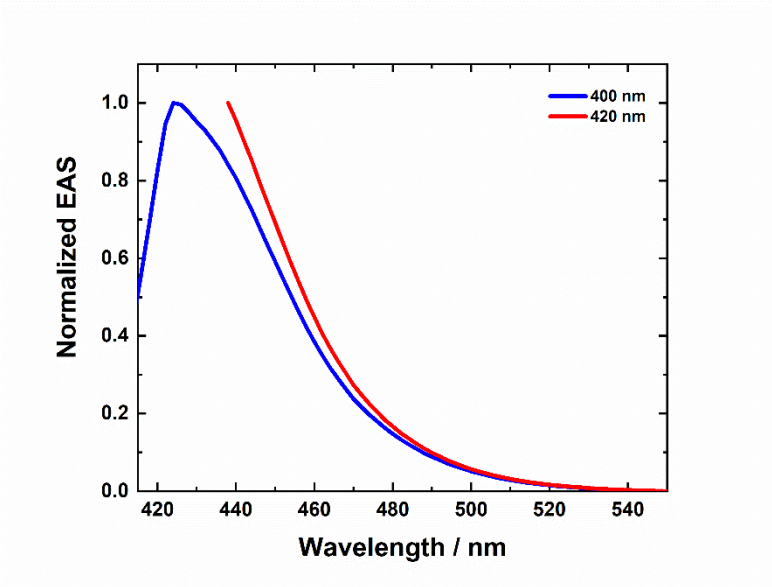

Figure S35. Normalized EAS of the ns time resolved fluorescence spectroscopy results obtained by global fitting of the raw data for **[3]*oi*Pr** ($c = 2.5 \cdot 10^{-6}$ M) with photoexcitation at 400 nm (blue) and 420 nm (red) at 80 K.

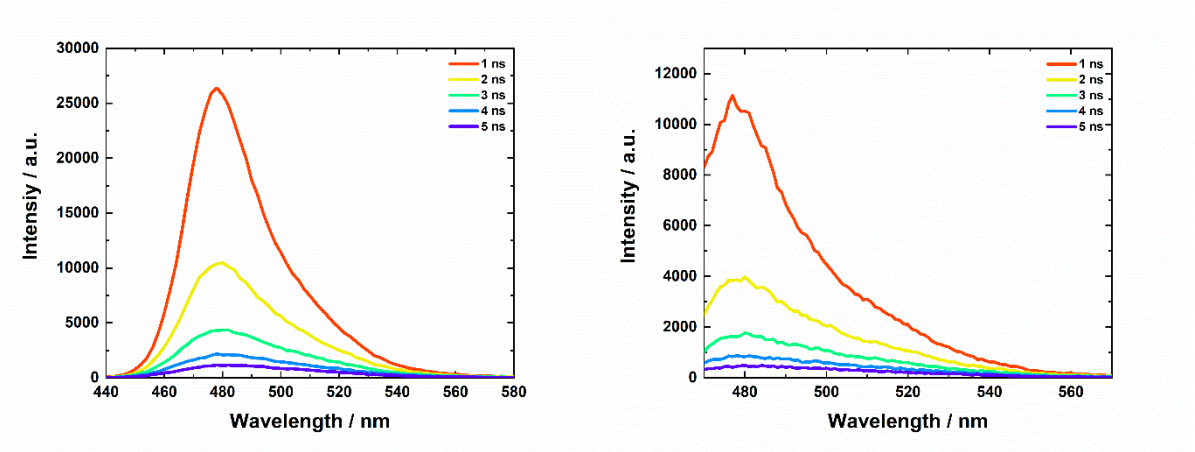

Figure S36. Selected ns time resolved fluorescence spectra at various deactivation/delay times for **[5]*oi*Pr** (c = $2.5 \cdot 10^{-6}$ M) with photoexcitation at 420 nm (left) and 460 nm (right) at 80 K.

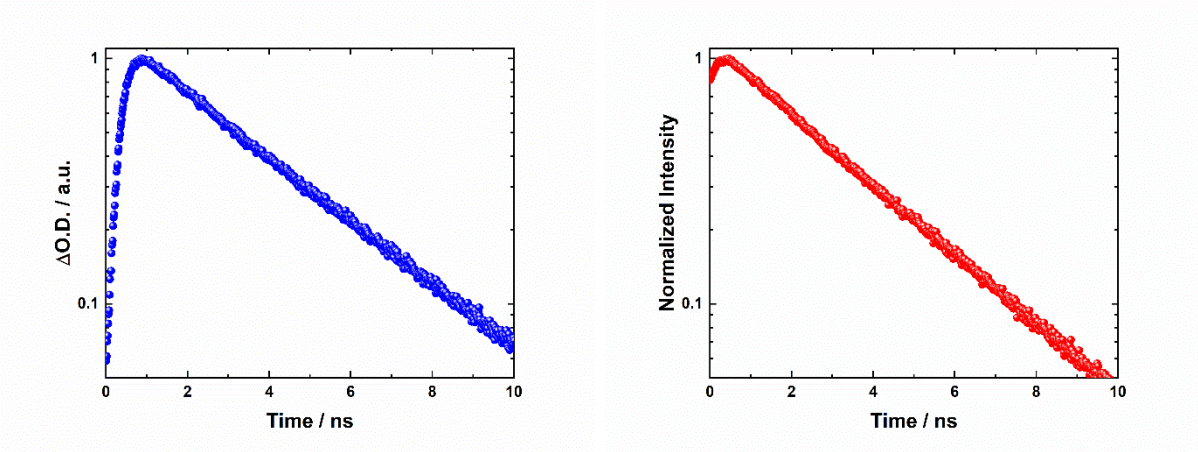

Figure S37. Normalized kinetic traces obtained at 485 nm emission wavelength by ns time resolved fluorescence spectroscopy experiments for **[5]*oi*Pr** ($c = 2.5 \cdot 10^{-6}$ M) with photoexcitation at 420 nm (left) and 460 nm (right) at 80 K.

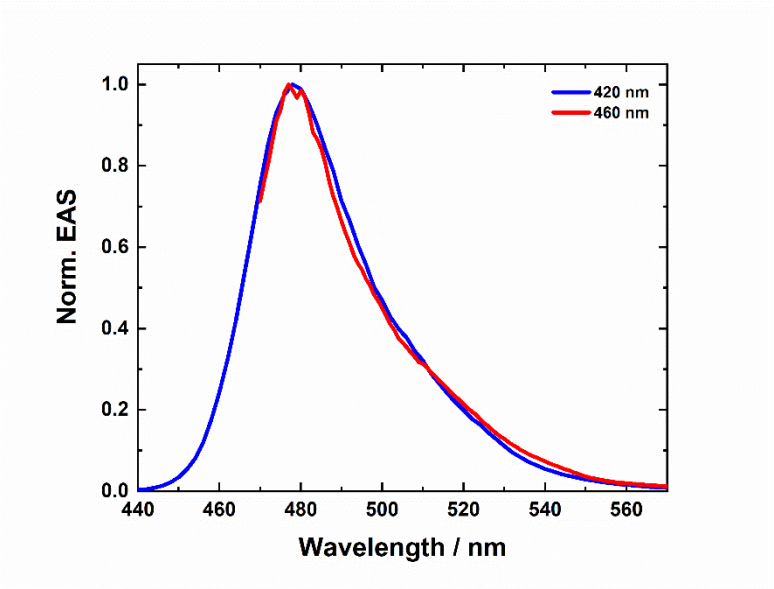

Figure S38. Normalized EAS of the ns time resolved fluorescence spectroscopy results obtained by global fitting of the raw data for **[5]*oi*Pr** ($c = 2.5 \cdot 10^{-6}$ M) with photoexcitation at 420 nm (blue) and 460 nm (red) at 80 K.

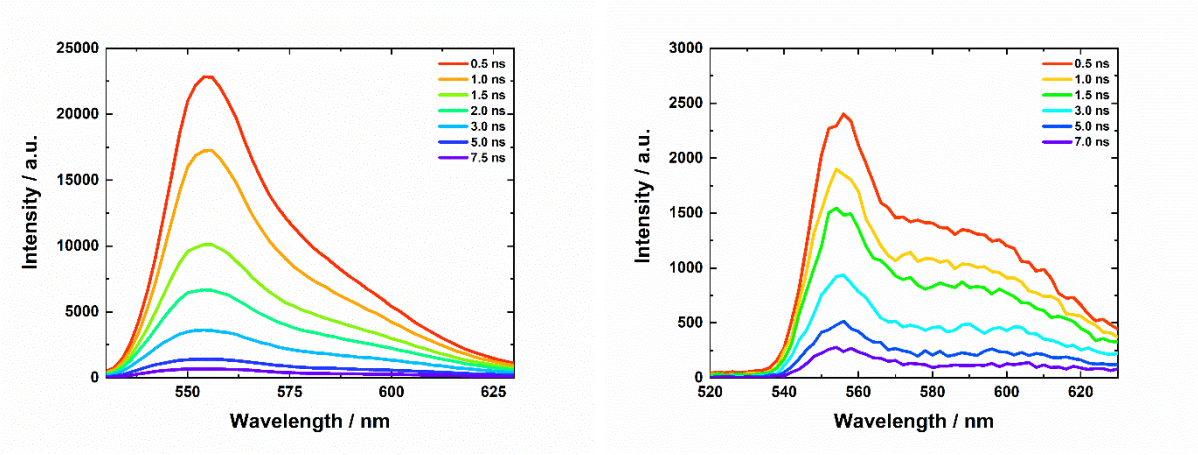

Figure S39. Selected ns time resolved fluorescence spectra at various deactivation/delay times for **[7]*oi*Pr** (c = $2.5 \cdot 10^{-6}$ M) with photoexcitation at 440 nm (left) and 520 nm (right) at 80 K.

In contrast to **[7]*oi*Pr**, the EAS of **[3]*oi*Pr** and **[5]*oi*Pr** obtained by global fitting of the ns resolved fluorescence data at 80 K revealed no significant differences upon changing the excitation wavelength. In the case of **[3]*oi*Pr**, the observed fine structure in the steady state fluorescence experiment upon exciting in the red edge of the lowest energy absorption band could not be detected in the ns time resolved emission experiments, while for **[5]*oi*Pr** the excitation dependent emission maximum shift was not observable. We explain this discrepancy between both emission experiments by the difference in excitation bandwidth (1 nm vs. 10 nm) and the possible spectral resolution given by the slit width of the detection monochromator (1 nm vs. 3 nm). As mentioned in the main text of this paper, the cumulenes with smaller CAW size reveal a smaller conformational distribution due to increased steric hinderance of the bulky end groups, which leads to less pronounced spectral changes in both emission and transient absorption experiments upon changing the excitation energy compared to **[7]*oi*Pr**. Accordingly, only for **[7]*oi*Pr** a clear excitation dependence could be resolved in the ns time resolved emission spectra with our current experimental setup.

Table S1. Summary of the ns time resolved emission lifetimes obtained upon global fitting of the data.

	Excitation wavelength	τ / ns
[3]*oi*Pr	400 nm	1.73 ±0.01
	420 nm	1.69 ±0.02
[5]*oi*Pr	420 nm	2.59 ±0.05
	460 nm	2.73 ±0.07
[7]*oi*Pr	440 nm	2.58 ±0.03
	520 nm	2.35 ±0.04

fs-Transient absorption spectroscopy

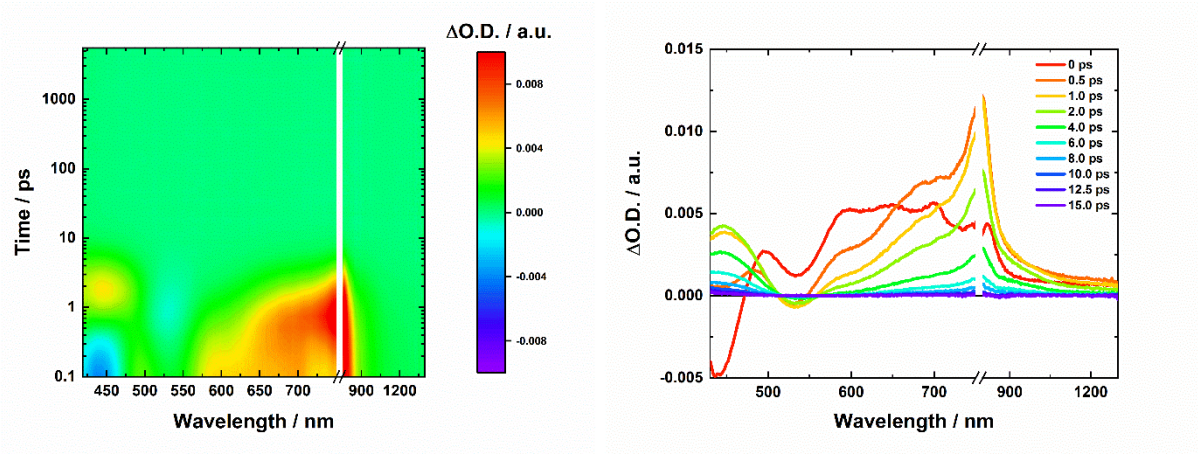

Figure S40. fs-TA contour plot (left) together with selected fs-TA spectra at various time delays (right) for **[3]*oi*Pr** obtained upon photoexcitation at 390 nm at 240 K. fs-TA raw data were chirp as well as zero point corrected.

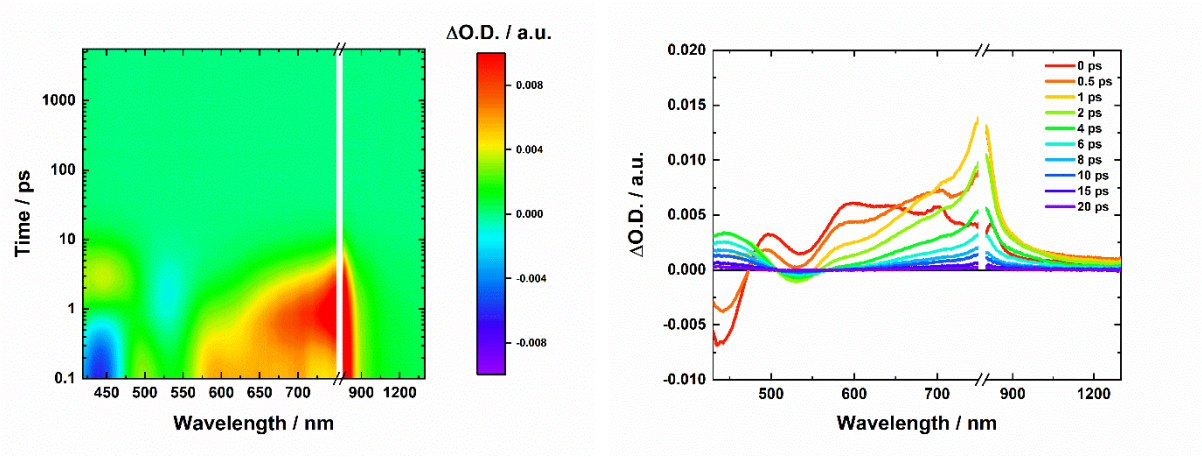

Figure S41. fs-TA contour plot (left) together with selected fs-TA spectra at various time delays (right) for [**3**]***oi*Pr** obtained upon photoexcitation at 390 nm at 200 K. fs-TA raw data were chirp as well as zero point corrected.

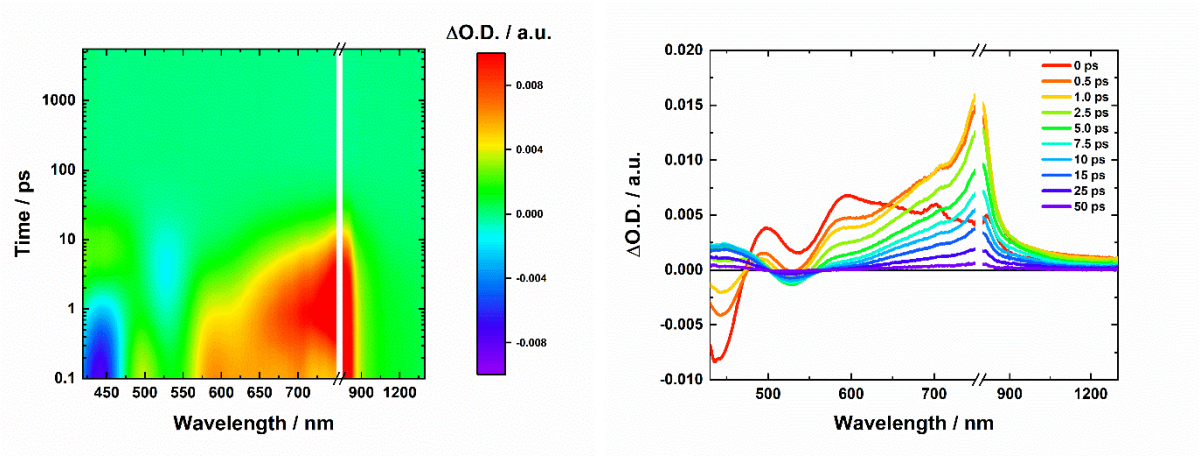

Figure S42. fs-TA contour plot (left) together with selected fs-TA spectra at various time delays (right) for **[3]*oi*Pr** obtained upon photoexcitation at 390 nm at 160 K. fs-TA raw data were chirp as well as zero point corrected.

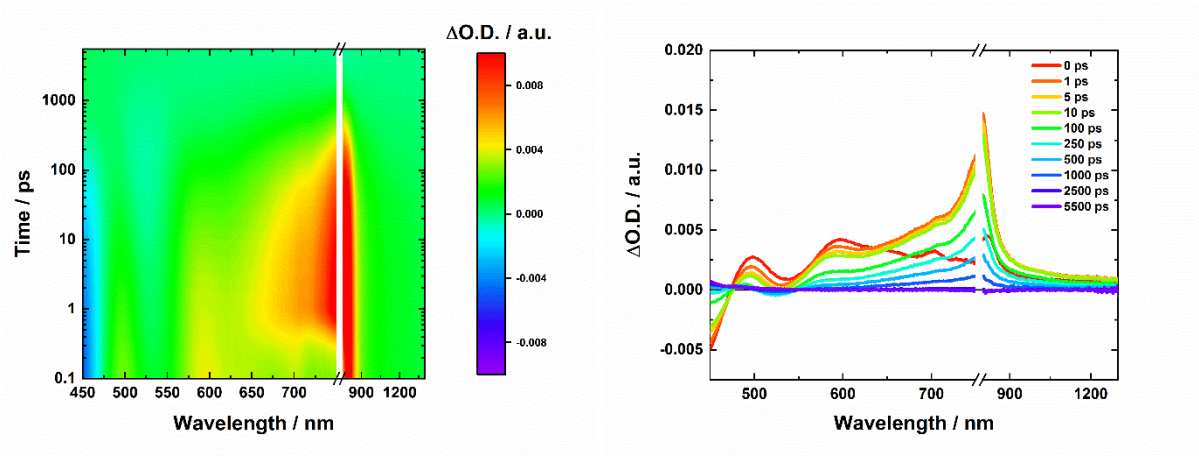

Figure S43. fs-TA contour plot (left) together with selected fs-TA spectra at various time delays (right) for **[3]*oi*Pr** obtained upon photoexcitation at 390 nm at 120 K. fs-TA raw data were chirp as well as zero point corrected.

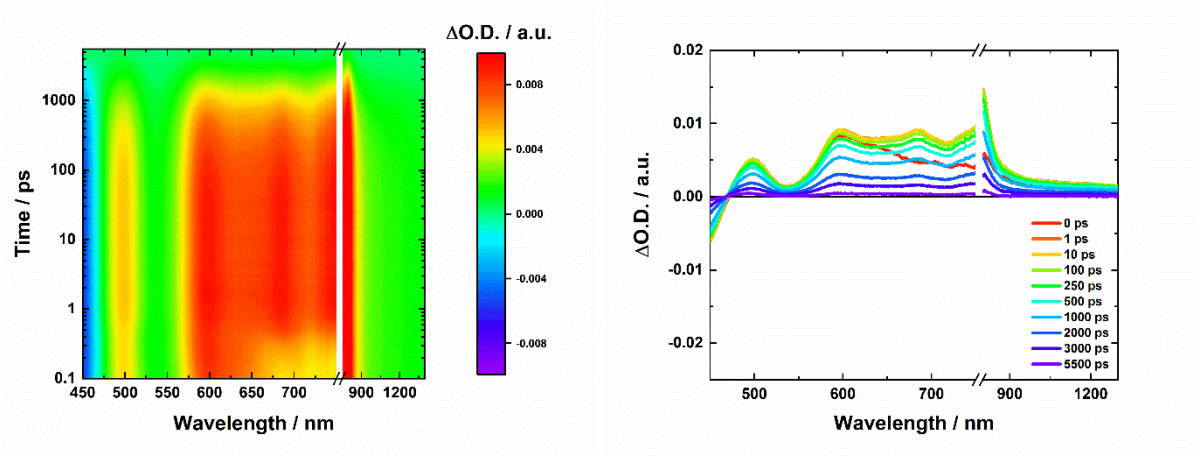

Figure S44. fs-TA contour plot (left) together with selected fs-TA spectra at various time delays (right) for **[3]*oi*Pr** obtained upon photoexcitation at 390 nm at 80 K. fs-TA raw data were chirp as well as zero point corrected.

Table S2. Summary of the fs-TA spectroscopy lifetimes obtained upon global fitting of the data for **[3]*oi*Pr** with photoexcitation at 390 nm.

[3]*oi*Pr	τ_1 / ps	τ_2 / ps	τ_3 / ps
rt	~ 0.3	0.6	1.7
240 K	~ 0.4	0.9	3.5
200 K	~ 0.5	1.5	5.5
160 K	~ 0.6	2.7	16.0
120 K	~ 0.6	45.6	539
80 K	~ 0.6	-	1770

For the assignment of the corresponding lifetimes see main text.

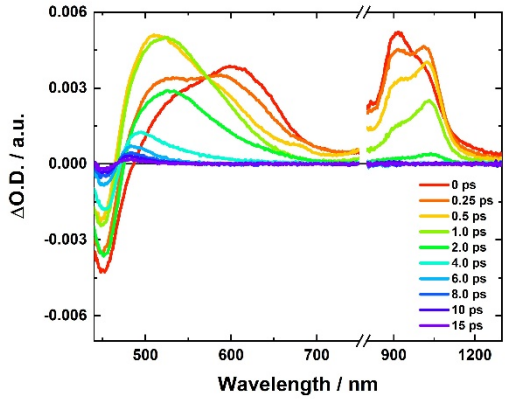

Figure S45. fs-TA spectra at various time delays for **[5]*oi*Pr** obtained upon photoexcitation at 390 nm at rt. fs-TA raw data were chirp as well as zero point corrected.

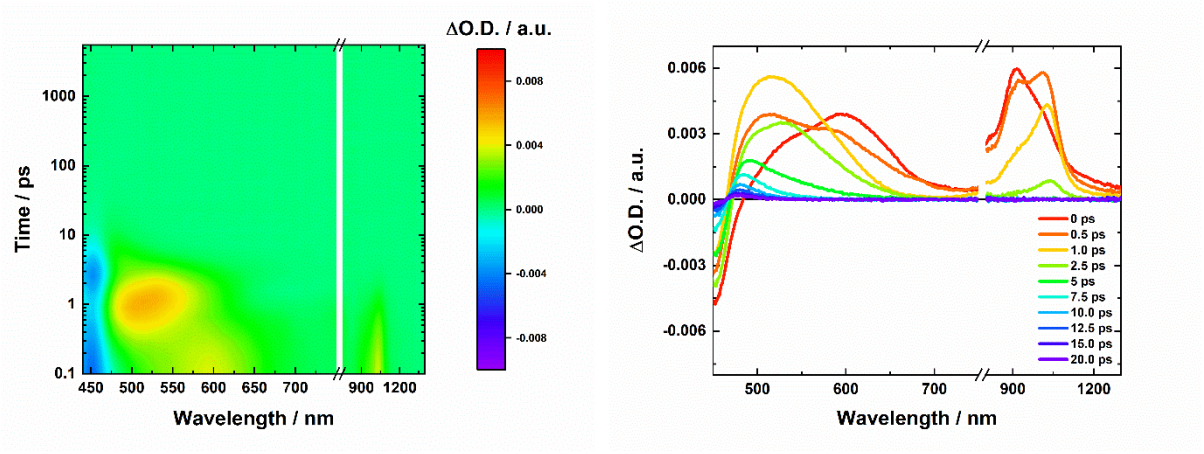

Figure S46. fs-TA contour plot (left) together with selected fs-TA spectra at various time delays (right) for **[5]*oi*Pr** obtained upon photoexcitation at 390 nm at 240 K. fs-TA raw data were chirp as well as zero point corrected.

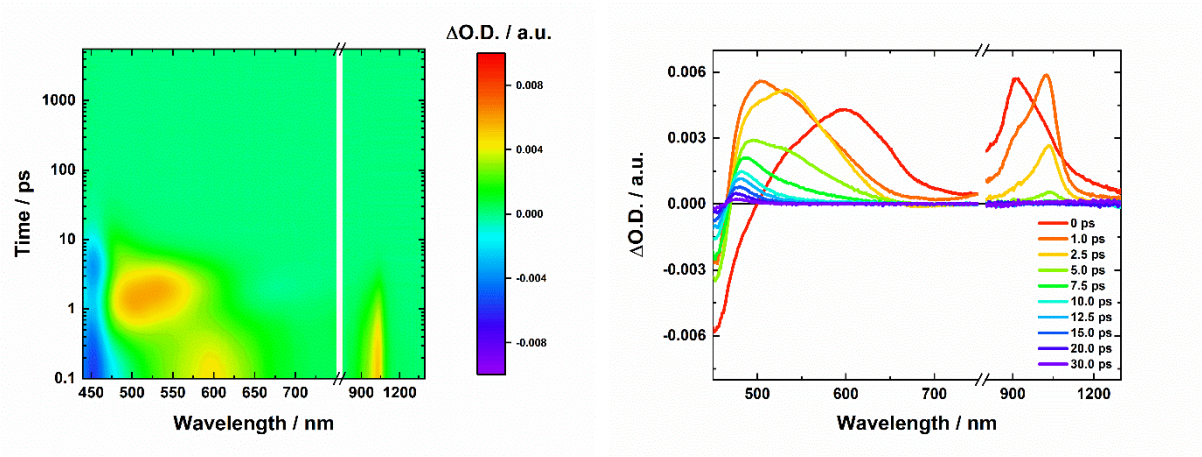

Figure S47. fs-TA contour plot (left) together with selected fs-TA spectra at various time delays (right) for **[5]*oi*Pr** obtained upon photoexcitation at 390 nm at 200 K. fs-TA raw data were chirp as well as zero point corrected.

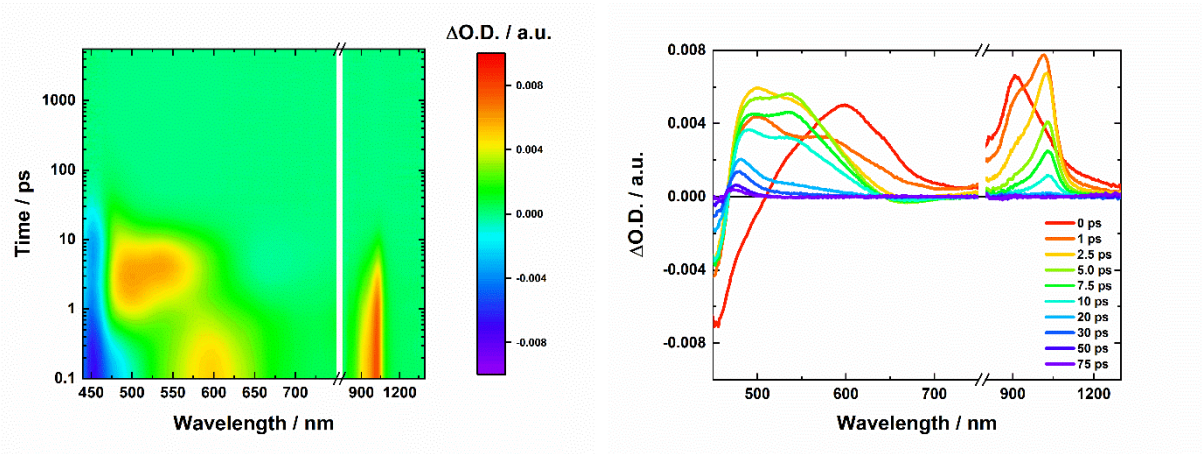

Figure S48. fs-TA contour plot (left) together with selected fs-TA spectra at various time delays (right) for **[5]*oi*Pr** obtained upon photoexcitation at 390 nm at 160 K. fs-TA raw data were chirp as well as zero point corrected.

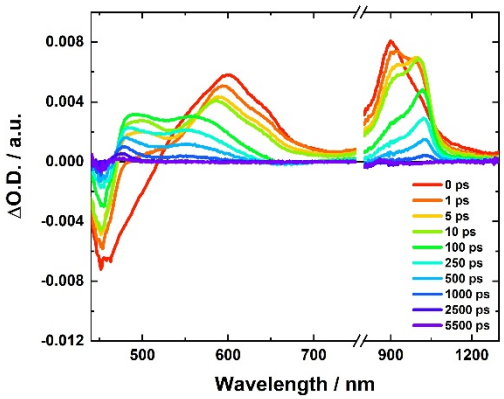

Figure S49. fs-TA spectra at various time delays for **[5]*oi*Pr** obtained upon photoexcitation at 390 nm at 120 K. fs-TA raw data were chirp as well as zero point corrected.

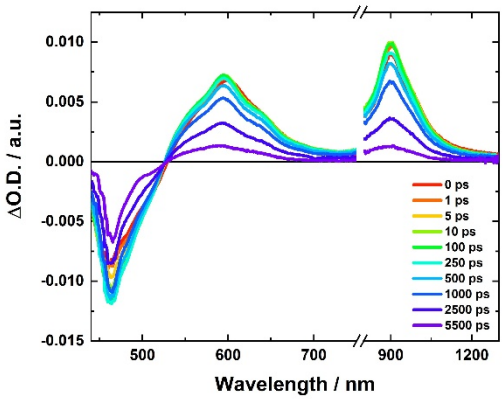

Figure S50. fs-TA spectra at various time delays for **[5]*oi*Pr** obtained upon photoexcitation at 390 nm at rt. fs-TA raw data were chirp as well as zero point corrected.

Table S3. Summary of the fs-TA spectroscopy lifetimes obtained upon global fitting of the data for **[5]*oi*Pr** upon photoexcitation at 390 nm.

[5]*oi*Pr	τ_1 / ps	τ_2 / ps	τ_3 / ps	τ_4 / ps	τ_5 / ps
rt	~ 0.2	~ 0.6	1.3	2.3	6.3
240 K	~ 0.2	~ 0.7	1.5	2.5	8.4
200 K	~ 0.3	1.3	2.0	3.6	10.0
160 K	~ 0.3	1.9	2.6	9.1	25.6
120 K	~ 0.5	7.0	57.6	379	951
80 K	~ 0.6	-	2540	-	-

The fs-TA of **[5]*oi*Pr** were modelled using a sequential five step global fit (except 80 K). The physical interpretation of these lifetimes is as follows: The first lifetime τ_1 reflects the BLA modulation together with other ultrafast relaxation processes. τ_2 indicates relaxation of the S_2 state due to twisting around C=C torsion. τ_3 describes the internal conversion rate of the relaxed S_2. τ_4 indicates relaxation of the S_1 and τ_5 deactivation of the relaxed S_1 back into the electronic ground state. We would like to emphasize, that the ongoing structural relaxation dynamics, which in turn heavily impact the excited state electronic structure, are likely to be way more complex to be modeled with just applying exponential fit functions.[2] Therefore, the presented lifetimes have to be taken as approximations to a way more complex situation. Here, one-dimensional electronic spectroscopy is at its limits due to the overall significantly present spectral congestion. Unraveling the exact kinetics will be subject to future research.

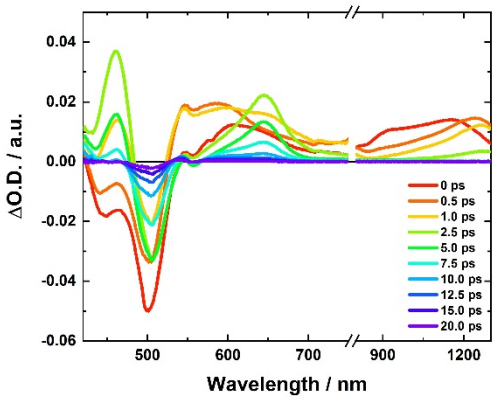

Figure S51. fs-TA spectra at various time delays for **[7]*oi*Pr** obtained upon photoexcitation at 390 nm at rt. fs-TA raw data were chirp as well as zero point corrected.

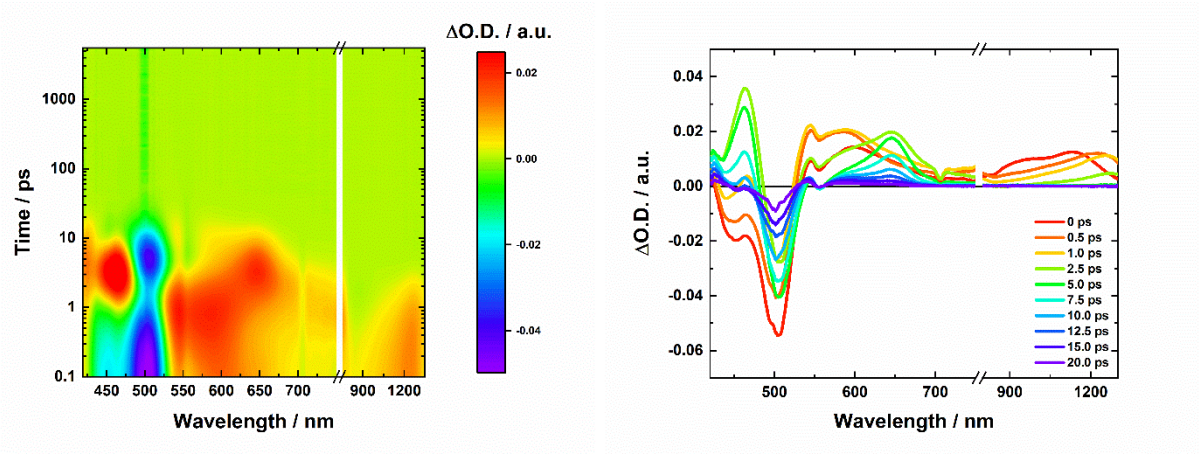

Figure S52. fs-TA contour plot (left) together with selected fs-TA spectra at various time delays (right) for **[7]*oi*Pr** obtained upon photoexcitation at 500 nm at 240 K. fs-TA raw data were chirp as well as zero point corrected.

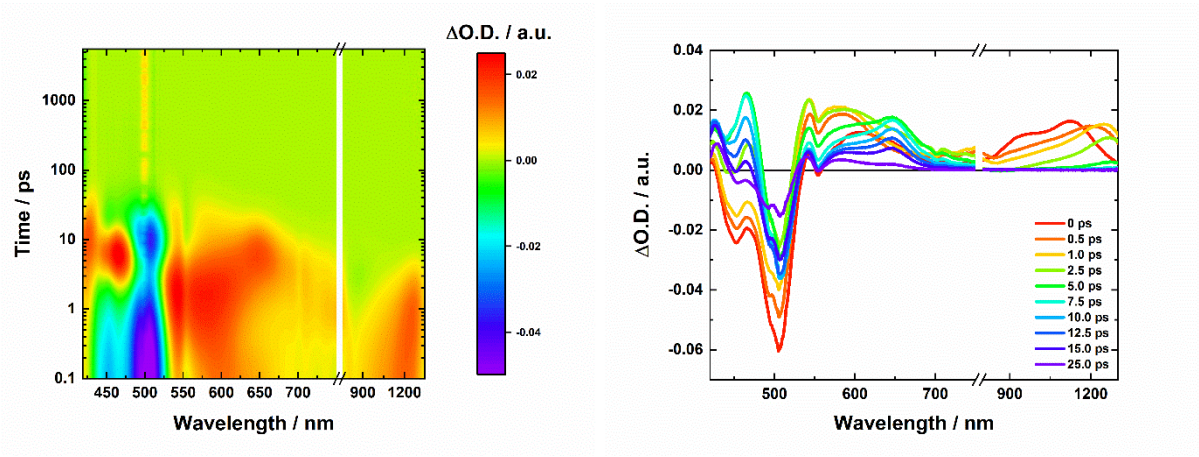

Figure S53. fs-TA contour plot (left) together with selected fs-TA spectra at various time delays (right) for **[7]*oi*Pr** obtained upon photoexcitation at 500 nm at 200 K. fs-TA raw data were chirp as well as zero point corrected.

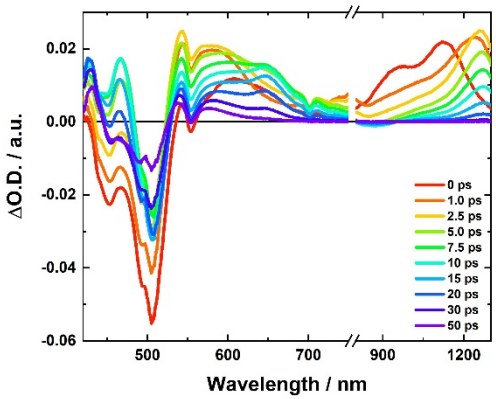

Figure S54. fs-TA spectra at various time delays for **[7]*oi*Pr** obtained upon photoexcitation at 390 nm at 160 K. fs-TA raw data were chirp as well as zero point corrected.

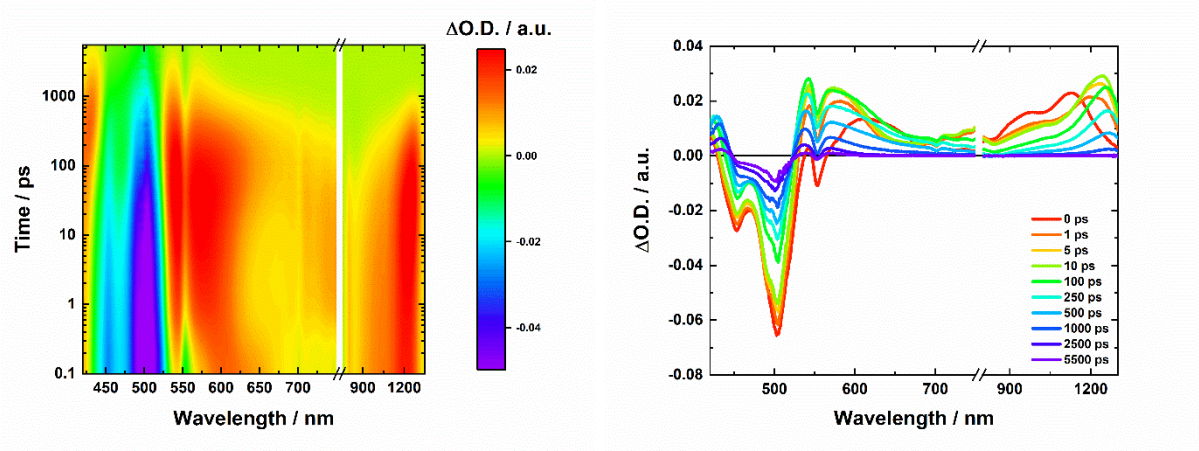

Figure S55. fs-TA contour plot (left) together with selected fs-TA spectra at various time delays (right) for **[7]*oi*Pr** obtained upon photoexcitation at 500 nm at 120 K. fs-TA raw data were chirp as well as zero point corrected.

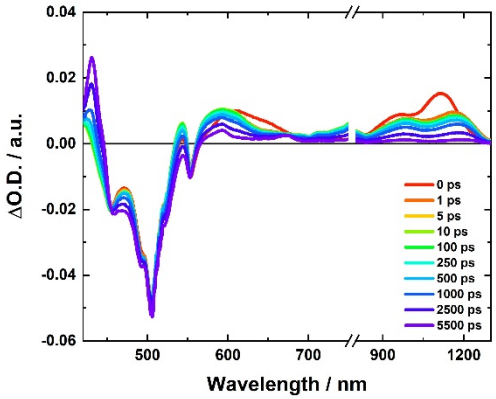

Figure S56. fs-TA spectra at various time delays for **[7]*oi*Pr** obtained upon photoexcitation at 390 nm at 80 K. fs-TA raw data were chirp as well as zero point corrected.

Table S4. Summary of the fs-TA spectroscopy lifetimes obtained upon global fitting of the data for **[7]*oi*Pr** upon photoexcitation at 500 nm.

[7]*oi*Pr	τ_1 / ps	τ_2 / ps	τ_3 / ps	τ_4 / ps	τ_5 / ps
rt	~ 0.3	~ 0.7	1.1	1.7	4.2
240 K	~ 0.3	1.0	1.3	2.9	6.6
200 K	~ 0.4	2.4	2.7	9.3	17.3
160 K	~ 0.6	3.1	3.6	9.5	17.3
120 K	~ 0.6	15.1	96.5	485	3660
80 K	~ 0.6	-	2740	-	infinite

The fs-TA of **[7]*oi*Pr** were modelled using a target fit comprising five total rate constants/lifetimes (except 80 K). These lifetimes are assigned to the following deactivation steps: The first lifetime τ_1 reflects the BLA modulation together with other ultrafast relaxation processes. τ_2 indicates structural relaxation of the S_3 state due to twisting of the endgroups around the C=C cumulene chain. τ_3 describes the parallel internal conversion rate of the relaxed S_3 into S_2, S_1 and S_0. The lifetime τ_4 indicates deactivation of the S_2 and τ_5 deactivation of S_1 back into the electronic ground state. Again, like for **[5]*oi*Pr**, the ongoing structural relaxation dynamics are expected to be too complex to be modeled with just applying exponential fit functions. The presented lifetimes have to be taken as approximations and the exact determination will be subject to future research. According to our computational results, a parallel excitation in all singlet excited states S_3, S_2 and S_1 is present. However, according to the calculated oscillator strengths major contribution is the bright S_0-S_3 excitation and our fs-TA spectra show no hints towards significant parallel excitations of the lower singlet excited states. We therefore simplified our kinetic model to a single excitation in the S_3 state.

ns-Transient absorption spectroscopy

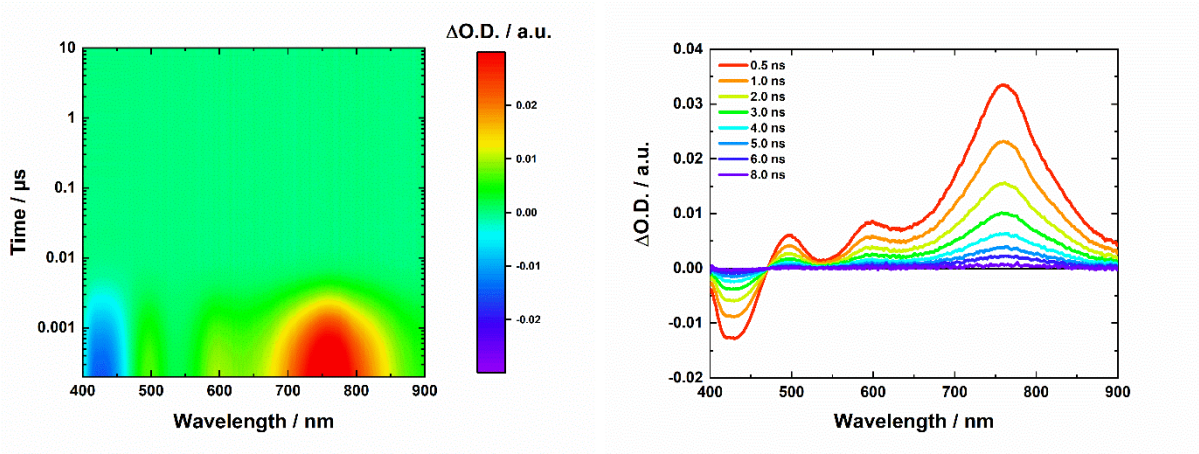

Figure S57. ns-TA contour plot (left) together with selected ns-TA spectra at various time delays (right) for **[3]*oi*Pr** obtained upon photoexcitation at 390 nm at 80 K. ns-TA raw data were zero point corrected. A monoexponential global fit of the ns-TA data yields a lifetime of 1.88 ns.

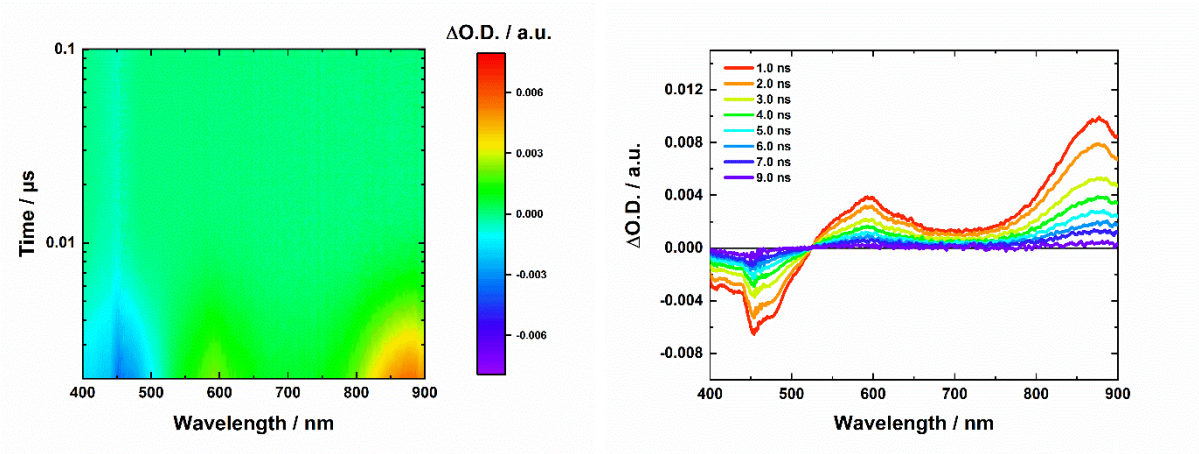

Figure S58. ns-TA contour plot (left) together with selected ns-TA spectra at various time delays (right) for **[5]*oi*Pr** obtained upon photoexcitation at 390 nm at 80 K. ns-TA raw data were zero point corrected. A monoexponential global fit of the ns-TA data yields a lifetime of 2.75 ns.

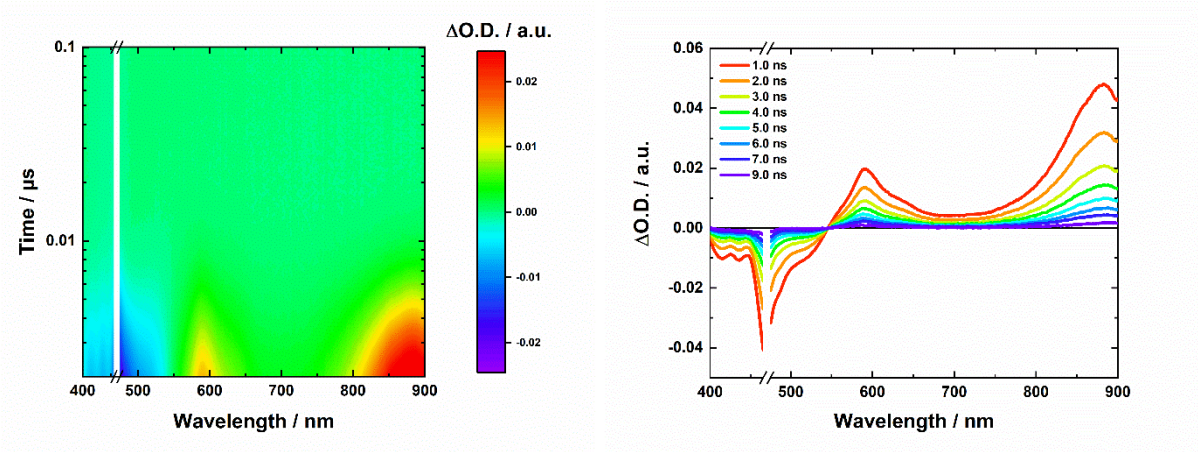

Figure S59. ns-TA contour plot (left) together with selected ns-TA spectra at various time delays (right) for **[5]*oi*Pr** obtained upon photoexcitation at 470 nm at 80 K. ns-TA raw data were zero point corrected. A monoexponential global fit of the ns-TA data yields a lifetime of 2.52 ns.

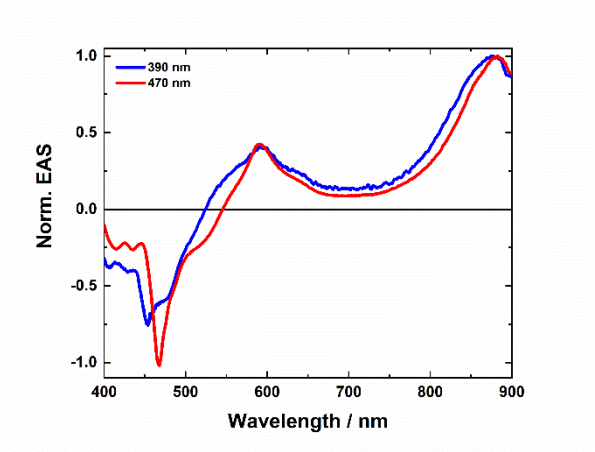

Figure S60. Normalized EAS for **[5]*oi*Pr** at 80 K obtained upon photoexcitation at 390 nm (blue) or 470 nm (red). EAS corresponding to S_2 obtained *via* global fit of ns-TA data.

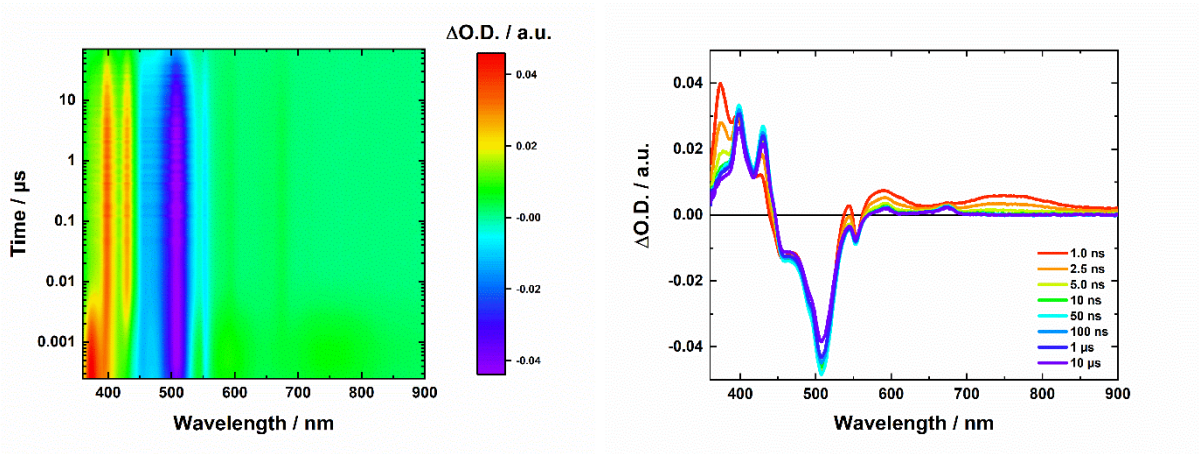

Figure S61. ns-TA contour plot (left) together with selected ns-TA spectra at various time delays (right) for **[7]*oi*Pr** obtained upon photoexcitation at 500 nm at 90 K. ns-TA raw data were zero point corrected.

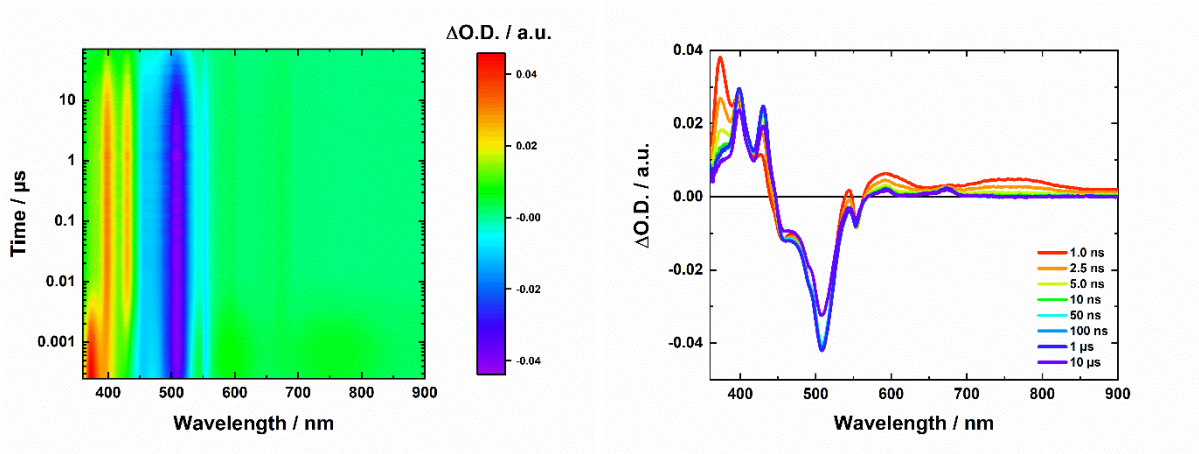

Figure S62. ns-TA contour plot (left) together with selected ns-TA spectra at various time delays (right) for **[7]*oi*Pr** obtained upon photoexcitation at 500 nm at 80 K. ns-TA raw data were zero point corrected.

Table S5. Summary of the ns-TA spectroscopy lifetimes obtained upon global fitting of the data for **[7]*oi*Pr** upon photoexcitation at 500 nm.

[7]*oi*Pr	τ_1 / ns	τ_2 / ns	τ_3 / ns	τ_4 / ns
120 K	~ 0.6	1.1	6.9	279
110 K	~ 0.6	2.8	30.0	498
100 K	-	2.7	35400	-
90 K	-	2.7	55200	-
80 K	-	2.7	55800	-

The ns-TA of **[7]*oi*Pr** were modelled using a sequential global fit comprising 4 (120 and 110 K) and 2 (100, 90 and 80 K) total rate constants/lifetimes, respectively. These lifetimes are assigned to the following deactivation steps: The first lifetime τ_1 reflects relaxation of S_3. τ_2 indicates internal conversion into S_1 and S_0 of S_3. τ_3 describes the lifetime of S_1 and τ_4 indicates the intersystem crossing rate of T_1 back into the electronic ground state.

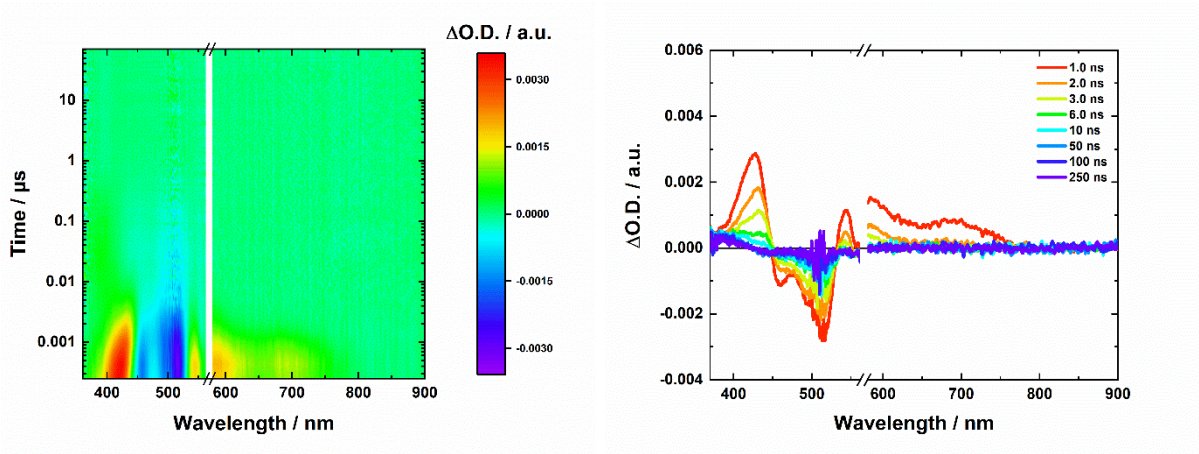

Figure S63. ns-TA contour plot (left) together with selected ns-TA spectra at various time delays (right) for **[7]*oi*Pr** obtained upon photoexcitation at 570 nm at 120 K. ns-TA raw data were zero point corrected.

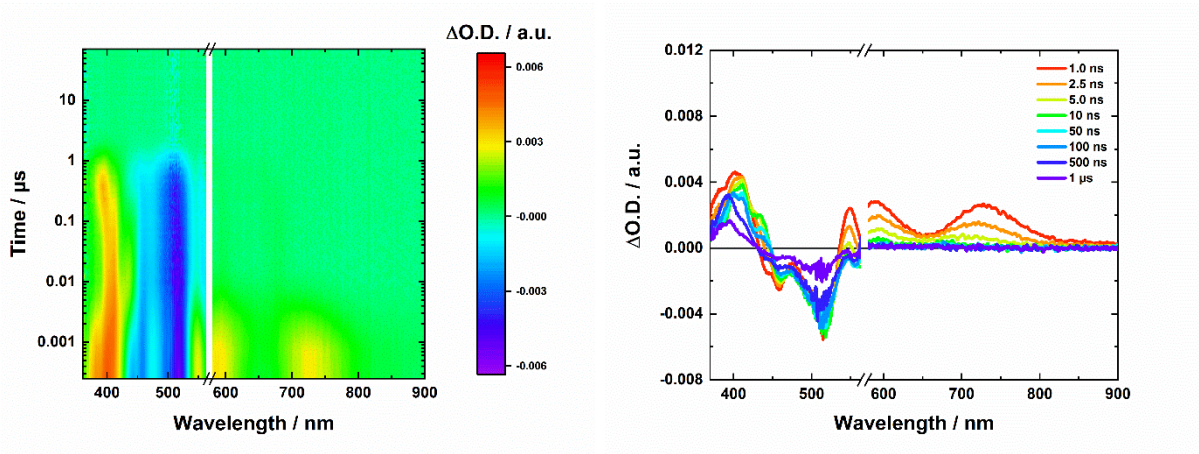

Figure S64. ns-TA contour plot (left) together with selected ns-TA spectra at various time delays (right) for **[7]*oi*Pr** obtained upon photoexcitation at 570 nm at 110 K. ns-TA raw data were zero point corrected.

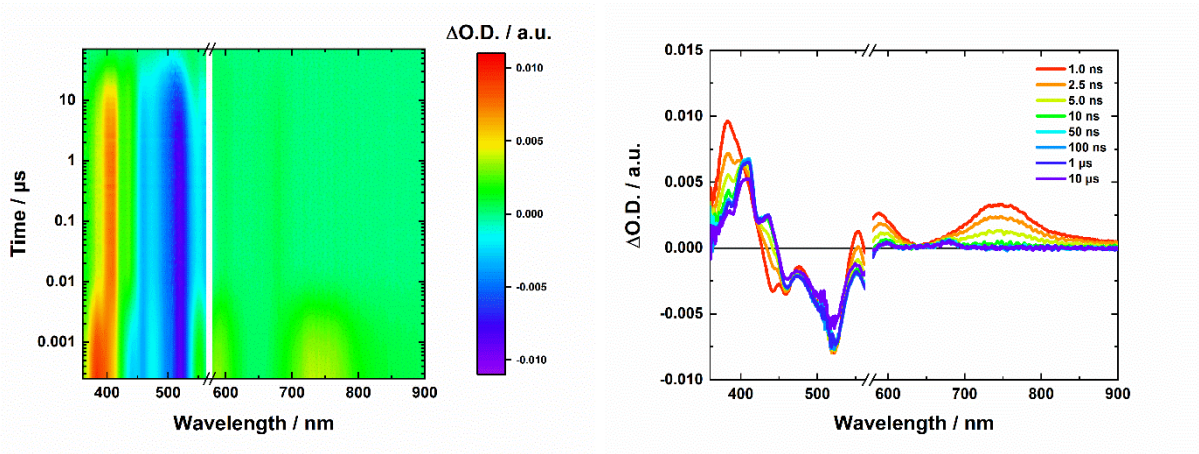

Figure S65. ns-TA contour plot (left) together with selected ns-TA spectra at various time delays (right) for **[7]*oi*Pr** obtained upon photoexcitation at 570 nm at 100 K. ns-TA raw data were zero point corrected.

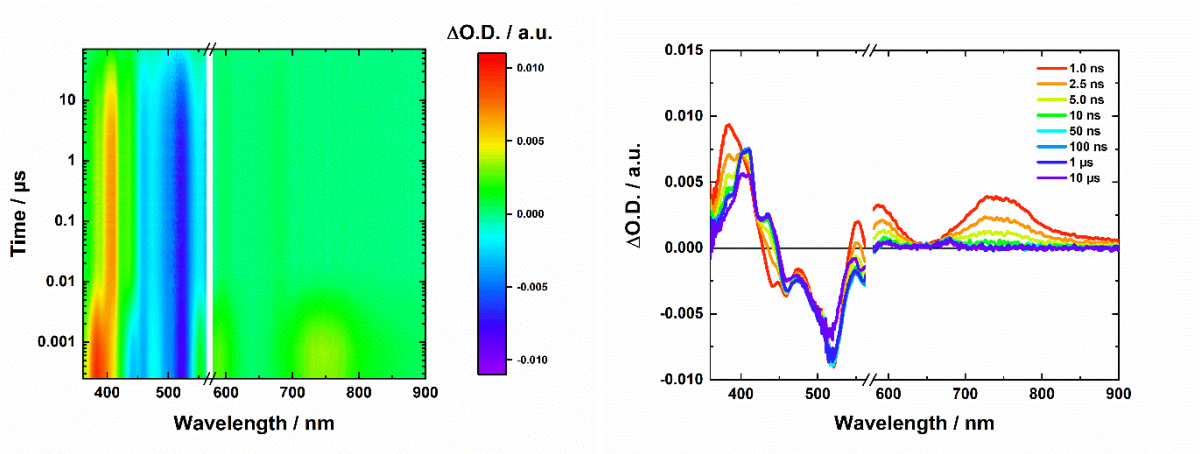

Figure S66. ns-TA contour plot (left) together with selected ns-TA spectra at various time delays (right) for **[7]*oi*Pr** obtained upon photoexcitation at 570 nm at 90 K. ns-TA raw data were zero point corrected.

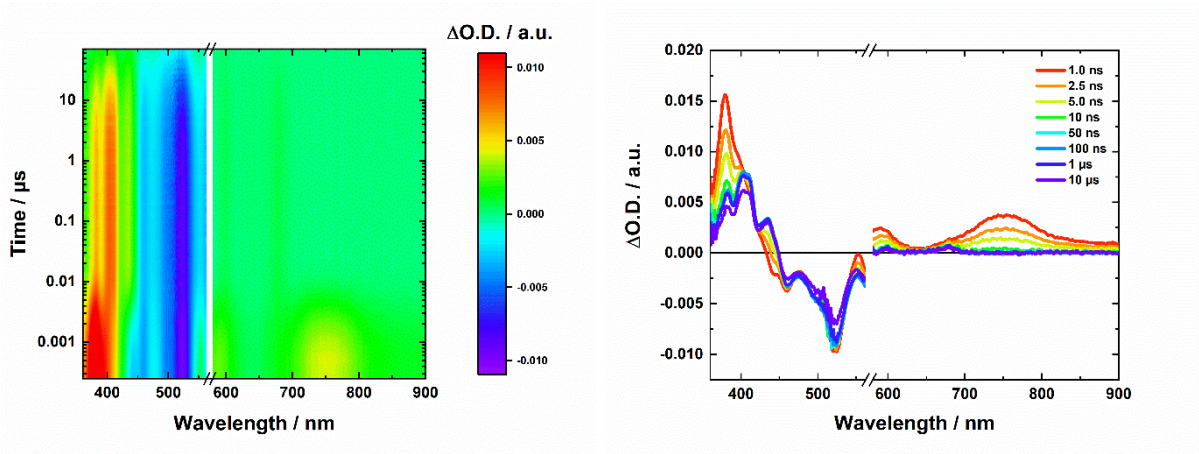

Figure S67. ns-TA contour plot (left) together with selected ns-TA spectra at various time delays (right) for **[7]*oi*Pr** obtained upon photoexcitation at 570 nm at 80 K. ns-TA raw data were zero point corrected.

Table S6. Summary of the fs-TA spectroscopy lifetimes obtained upon global fitting of the data for **[7]*oi*Pr** upon photoexcitation at 570 nm.

[7]*oi*Pr	τ_1 / ns	τ_2 / ns	τ_3 / ns	τ_4 / ns
120 K	~ 0.6	1.3	7.4	254
110 K	~ 0.5	2.4	33.3	489
100 K	-	2.8	32400	-
90 K	-	3.0	55500	-
80 K	-	2.9	57000	-

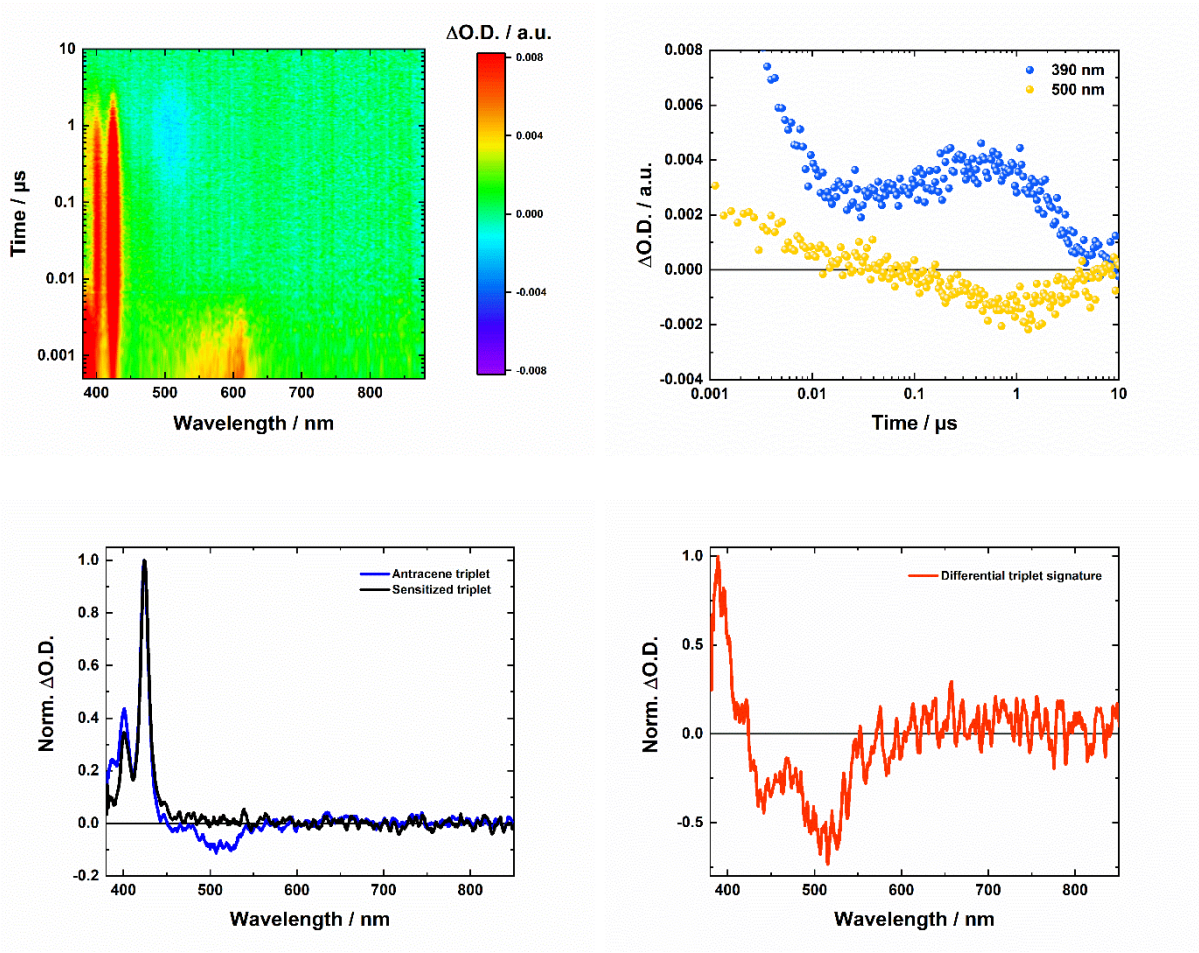

Figure S68. ns-TA contour plots (top, left) of the triplet sensitization experiment for **[7]*oi*Pr** ($c = 1.0 \cdot 10^{-5}$ M) with anthracene ($c = 6.0 \cdot 10^{-5}$ M) as sensitizer obtained upon photoexcitation at 370 nm. Representative kinetics at 390 and 500 nm (top, right) show a successful triplet-triplet energy transfer from anthracene to **[7]*oi*Pr**. The obtained normalized triplet signature (bottom, left) as well as the **[7]*oi*Pr** triplet spectrum with subtracted anthracene triplet (bottom, right).

Vibrational spectroscopy and transient infrared spectroscopy

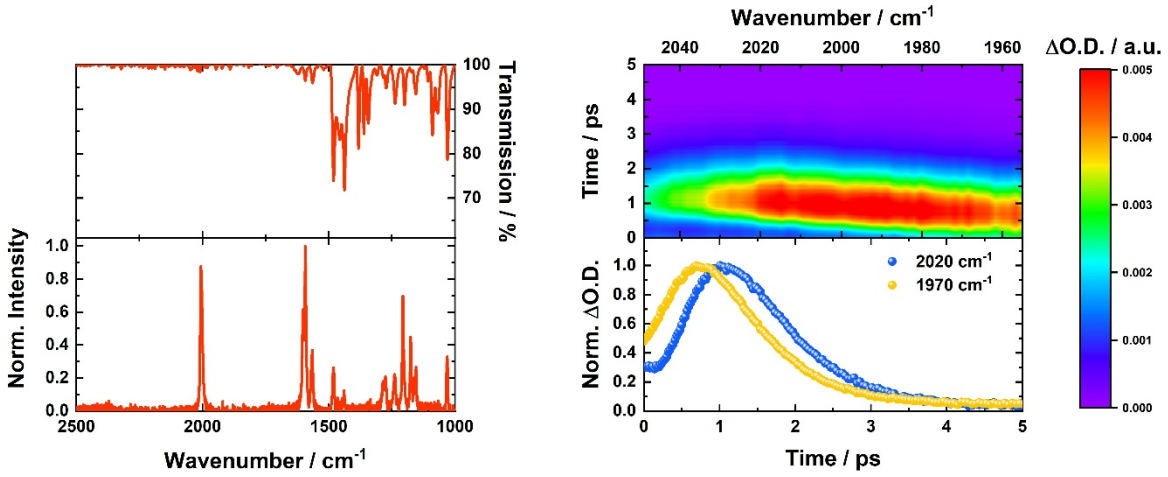

Figure S69. Steady state IR and normalized Raman spectrum of **[5]*oi*Pr** (left). Both spectra are obtained in the solid state. Transient IR contour map obtained in 3-methylpentane upon photoexcitation at 370 nm together with representative kinetics at 1970 and 2040 cm^{-1}.

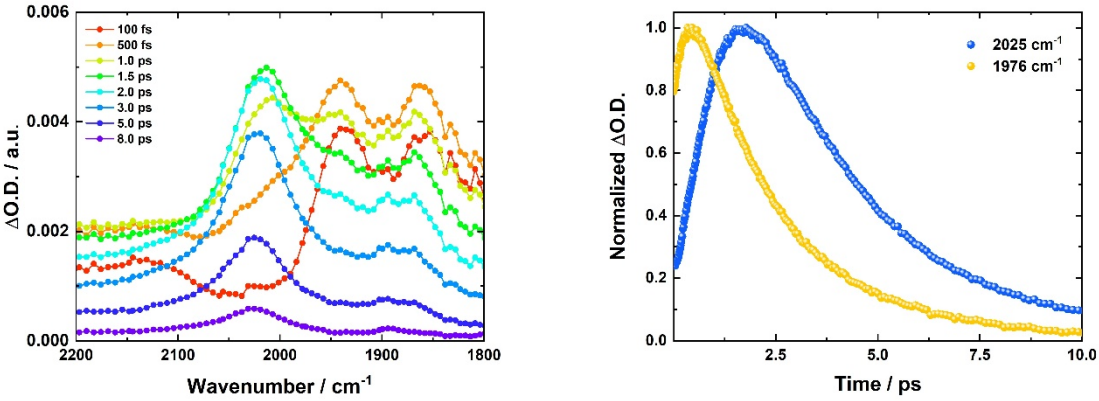

Figure S70. Transient IR spectra of **[7]*oi*Pr** (left) obtained in 3-methylpentane upon photoexcitation at 370 nm together with representative kinetics at 1976 and 2025 cm^{-1} (right).

Table S7. Summary of the obtained transient IR spectroscopy lifetimes.

	τ_1 / ps	τ_2 / ps	τ_3 / ps	τ_4 / ps
[3]*oi*Pr	~ 0.2	2.51 ±0.04		
[5]*oiP*r	~ 0.2	~ 0.4	0.81 ±0.09	
[7]*oi*Pr	~ 0.2	0.85 ±0.07	2.15 ±0.06	2.85 ±0.07

It should be noted, that there is an overall discrepancy between the obtained lifetimes from TAS and transient IR spectroscopy. This is due to the fact that the structural changes due to the rotation of the terminal endgroups are not reflected in the transient IR experiments, since the expected shifts of the IR band are below the resolution of our transient IR experiment (8.65 cm^{-1}).

Aggregation studies

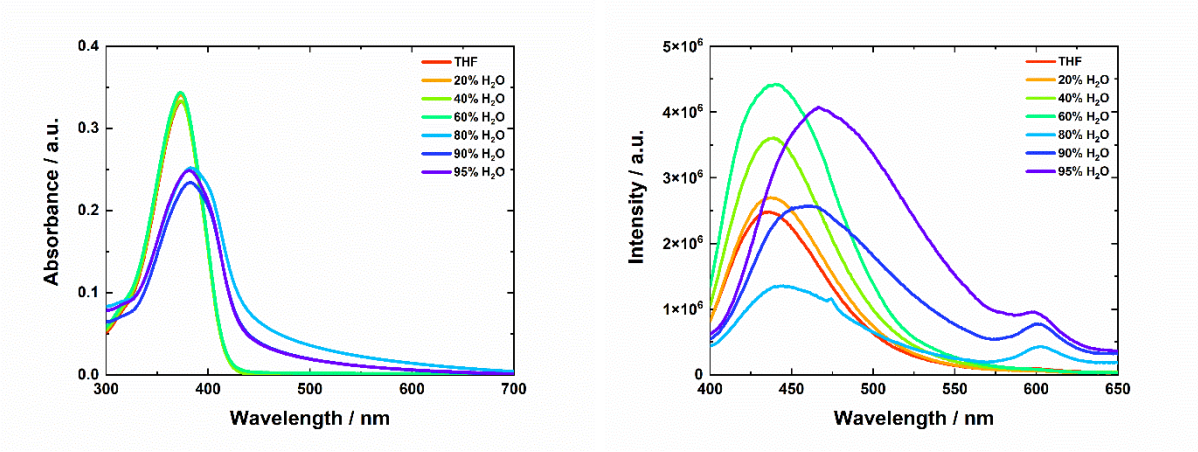

Figure S71. Steady-state absorption (left) and emission spectra (right) of **[3]*oi*Pr** (c = $1.5 \cdot 10^{-5}$ M) upon photoexcitation at 370 nm recorded in different THF/water ratios.

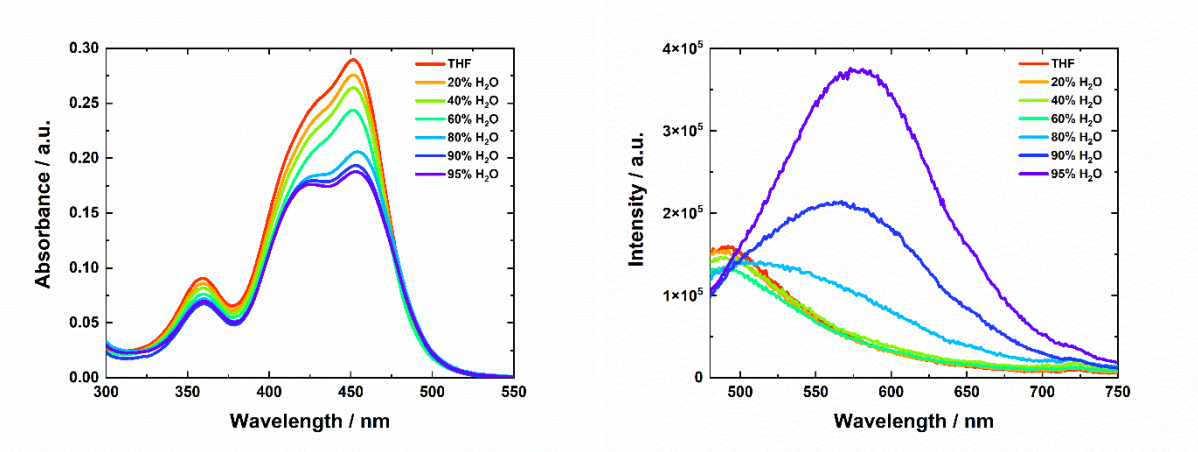

Figure S72. Steady-state absorption (left) and emission spectra (right) of **[5]*oi*Pr** (c = $1 \cdot 10^{-5}$ M) upon photoexcitation at 410 nm recorded in different THF/water ratios.

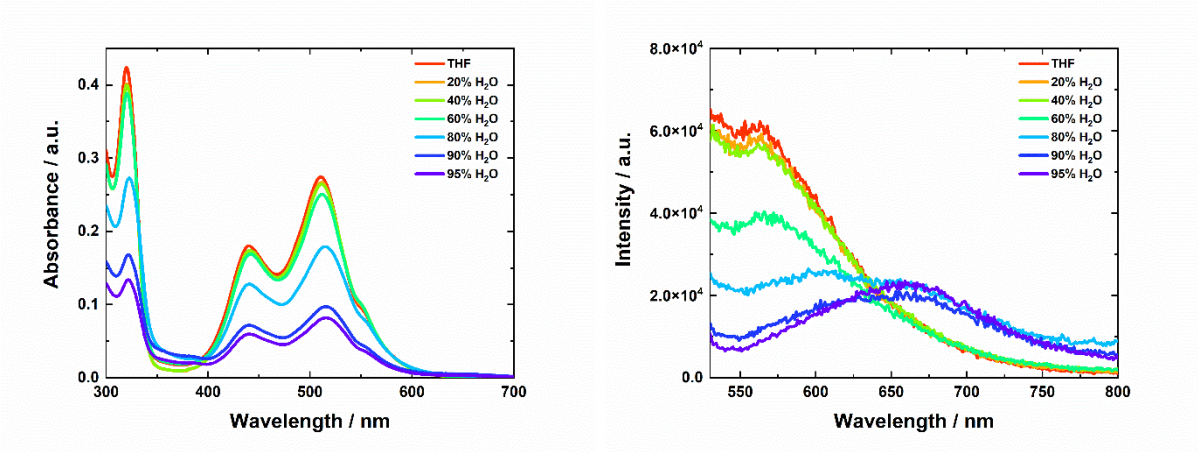

Figure S73. Steady-state absorption (left) and emission spectra (right) of **[5]*oi*Pr** (c = $2 \cdot 10^{-5}$ M) upon photoexcitation at 440 nm recorded in different THF/water ratios.

It should be noted that upon forcing aggregation of the investigated **[*n*]*oi*Pr** cumulenes, they begin to rapidly decompose. In particular, **[7]*oi*Pr** decomposed within several minutes.

Computational Methods

The equilibrium molecular structures of the electronic ground state were firstly computed at the semi-empirical tight-binding density functional theory level (GFN2-xTB). GFN2-xTB meta-dynamics were carried out with the algorithm CREST (v 2.11) for sampling the conformational space. Most stable conformers were optimized at the GFN2-xTB level with very tight geometry convergence thresholds, and further re-optimized at the DFT level. For DFT calculations different exchange correlation functional were considered, namely: i) the hybrid B3LYP-D3, ii) the double hybrid B2PLYP and iii) the range-separated wB97X-D3. The basis sets adopted were the cc-pVTZ for B3LYP-D3 and wB97X-D3, and the def2-TZVP for B2PLYP.

Electronic excited state calculations were performed within the frame of the time-dependent (TD-DFT) and Tamm-Dancoff Approximation (TDA) approaches. Vertical (i.e., Franck-Condon, FC) electronic excitations were computed on top of ground state (S_0) equilibrium structures. The relaxed equilibrium geometry of the dipole allowed excited states were determined at the TD-DFT level. For the excited state geometry optimizations both cc-pVTZ and cc-pVDZ basis sets were considered. For the systems here investigated the effect of the basis set (TZ vs. DZ) onto the excited state energies and geometries was minimal, therefore to save computational time and resources we opted, especially for the longest cumulene species (**[5]*oi*Pr** and **[7]*oi*Pr**) for the reduced (cc-pVDZ) basis set.

Transient absorption spectra (TA), specifically excitations amongst the *i*-th and *j*-th electronic excited states (S_i-S_j, with $i,j = 0, 1, 2, 3, \ldots$), were computed at the TDA level. All calculations were performed in gas-phase.

In addition, the multireference nature of the ground and lowest excited states was assessed by performing DFT/-/MRCI calculations [3]. This method is a powerful tool that combines the dynamic and static electron correlations. It is a combination of DFT (which gives information about dynamic correlation) and truncated MRCI expansions (to take the static correlation into account). DFT/-/MRCI calculations were carried out on model systems **[5]H** and **[7]H** of **[5]*oi*Pr** and **[7]*oi*Pr**, featuring H instead of iPr substituents, and on **[5]*oi*Pr** itself. Beside DFT/-/MRCI calculations, ground and excited states were determined with the complete active space self-consistent field (CASSCF)[4] calculations, followed by NEVPT2[5,6] corrections to include dynamical correlation. The orbital space considered for CASSCF calculations included 10 electrons in 10 orbitals (10,10). Due to the negligible effect of iPr substituents on the wavefunction composition documented by DFT/-/MRCI calculations, the NEVPT2 calculations were carried out only on the model systems **[5]H** and **[7]H**. The results show that both the ground electronic state and the lowest excited states are dominated by a single reference configuration. More specifically, the role of multiple excitations (double excitations and more) is almost negligible for the lowest bright excited state which is dominated by the HOMO→LUMO excitation and in some case it is the mixing of two singly excited configurations (HOMO→LUMO and HOMO–1→LUMO). As for the ground electronic state, a modest contribution of the doubly excited H,H→L,L configuration is detected (less than 2% of the total wavefunction at DFT/-/MRCI level and less than 6% at CASSCF level) which slightly increases to for the longest cumulene, as expected due to the HOMO/LUMO gap reduction. Overall, these results, collected in Tables S11-S13, confirm that DFT and TDDFT are suitable methods to describe the nature of the ground and lowest lying electronic states in these systems.

Beside the DFT/-/MRCI software package, the quantum chemical codes used for the computational investigation are the open source xTB (v. 6.4.1), ORCA (v. 5.0.3) and the program package Gaussian16 (v. C.01).

Ground-state conformers and equilibrium geometries

The *XYZ* coordinate files are reported at the end of the ESI. For **[3]*oi*Pr** two low-energy conformers were found, here named *conf1* and *conf2*. *conf1* is more stable than *conf2* by 1.735 kcal/mol (DFT(ωB97X-D3) energy). *conf1* shows the aryl groups tilted with respect to the *sp*-carbon chain, resulting on an average torsional angle $<\varphi>$ ~53° as computed at the wB97X-D3/cc-pVTZ level of theory. The result is in line with the calculations carried by explicitly taking into account the solvent molecules (*vide infra*). *conf2*, contrarily, shows one aryl group (one at each end) which lies almost flat within the plane of the carbon chain (φ ~14°), with the nearest neighbor aryl unit which is tilted (φ ~74°). In **Figure S74** are reported the optimized ground state molecular structures for *conf1* and *conf2* of (**[3]*oi*Pr** along with different views.

[3]*oi*Pr	*Lateral view*	*Top view*	*Side view (along the sp-chain)*
conf1	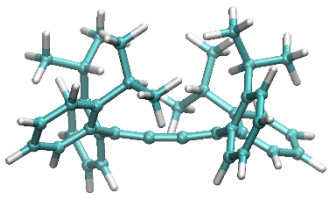	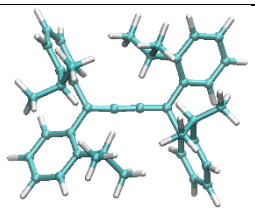	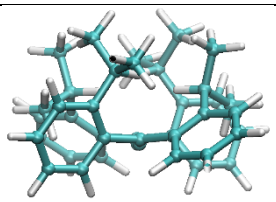
conf2	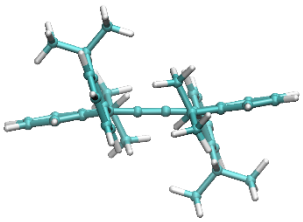	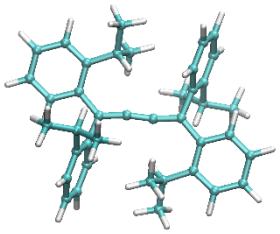	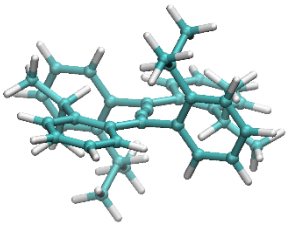

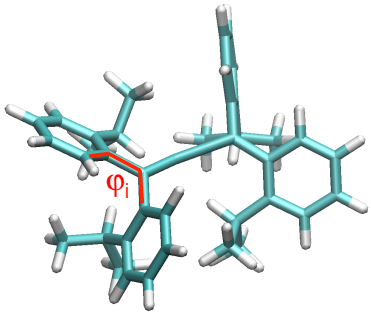

Figure S74. DFT (wB97X-D3/cc-pVTZ) gas-phase optimized ground state molecular structures of **[3]*oi*Pr** *conf1* and *conf2*. Bottom: definition of the aryl dihedral angle (φ_i).

The computed DFT bond lengths and bond length alternation parameter ($BLA = (r_1+r_3)/2 - r_2$) of *conf1* are reported in **Table S8**. Notably, as documented in **section "conformational effects of solvation and their influence on the electronic structure"** a local variation of φ_i modulates the π-electron conjugation extension between the terminal sp^2-carbons of the cumulenic chain and the neighboring sp^2 carbons belonging to the aryl units, thus affecting the local extension of the electron conjugation, the local bond orders and ultimately the BLA of the cumulene carbon chain.

Amongst the DFT functional used, B3LYP and B2PLYP result in a better agreement with the experimental XRD structural data than wB97X-D, however the latter is considered for its superior performance in describing the character and order of the excited states, especially those featuring a charge transfer or Rydberg character.

Table S8. Bond lengths, BLA and ξ ($\xi = \frac{1}{4}(\cos\varphi_1 + \cos\varphi_2 + \cos\varphi_3 + \cos\varphi_4)$ parameters as computed at different DFT levels for **[3]*oi*Pr** *conf1* (gas phase).

[3]*oi*Pr	*conf1*			
	r_1/r_3	r_2	BLA	ξ
wB97X-D3/cc-pVTZ	1.317	1.258	0.059	0.58
B3LYP-D3/cc-pVTZ	1.325	1.253	0.072	0.60
B2PLYP/def2-TZVP	1.332	1.256	0.076	0.61

Also for **[5]*oi*Pr,** two low-lying energy conformers were found (*conf1* and *conf2*), with *conf2* slightly more stable than *conf1* by 0.3 kcal/mol (DFT energy).

In **Figure S75** are reported the DFT optimized structures of **[5]*oi*Pr** *conf1* and *conf2*.

[5]*oi*Pr	*Lateral view*	*Top view*	*Side view (along the sp-chain)*
conf1	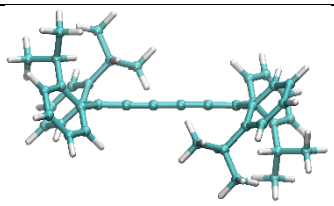	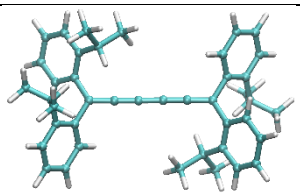	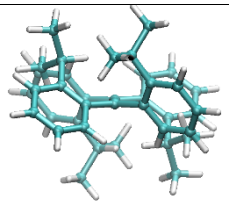
conf2	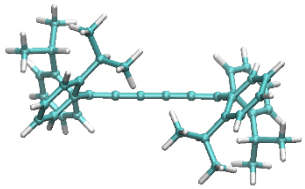	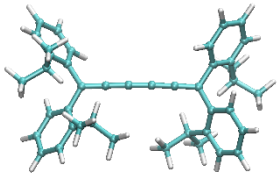	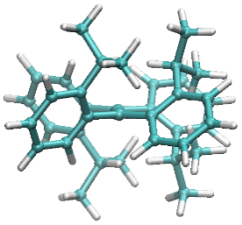

Figure S75. DFT (wB97X-D3/cc-pVTZ) gas-phase optimized ground state molecular structures of **[5]*oi*Pr** *conf1* and *conf2*.

As already observed for **[3]*oi*Pr**, the aryl groups for **[5]*oi*Pr** are also tilted with respect to the *sp*-carbon chain, showing an average torsional angle $< \varphi > \sim 53°$ ($\xi \sim 0.59$).

Table S9. Bond lengths, BLA and ξ parameters as computed at different DFT levels for **[5]*oi*Pr** *conf1* gas phase. Experimental data refer to cumulenes showing the same chain length however different aryl functionalization.

[5]*oi*Pr	*conf1*				
DFT	r_1	r_2	r_3	BLA	ξ
wB97X-D3/cc-pVTZ	1.317	1.261	1.284	0.039	0.59

For **[7]*oi*Pr**, one conformer is considered and in **Table S10** are reported the bond lengths, BLA and *ξ parameters.*

Table S10. Bond lengths, BLA and ξ parameters as computed at different DFT levels for **[7]*oi*Pr** *conf1* gas phase. Experimental data refer to cumulenes showing the same chain length however different aryl functionalization.

[7]*oi*Pr						
DFT	r_1	r_2	r_3	r_4	BLA	ξ
wB97X-D3/cc-pVTZ	1.317	1.262	1.281	1.265	0.036	0.59

TDDFT and TDA excited states and transient absorption spectra: [3]*oi*Pr species

For **[3]*oi*Pr t**he first and second singlet excited states (S_1 and S_2) are both dipole allowed.

The brightest state, S_1 (3.89 eV, 318 nm, f = 0.77) can be described as a HOMO - LUMO single particle excitation, characterized by the symmetry allowed π_x-π^*_x orbital transition (with x an axis perpendicular to the *sp*-chain, see **Figure S76**). Notably, the frontier molecular orbitals are delocalized over the entire molecule, involving both the *sp*-carbon atoms as well as the sp^2 carbons at the end of the chains and those belonging to the aryl units. The degree of delocalization is affected by the dihedral angles φ_i, which locally couples the π_x orbitals of the terminal sp^2 carbon atoms of the chain, with respect to the nearest neighbor π orbitals of the sp^2 carbons belonging to the aryl groups.

S_2 (4.13 eV, 300 nm, f = 0.13) can be described as a combination of HOMO-8 (π_y) and HOMO-5 (π_y) to LUMO (π^*_x) excitations, including also a small (but not negligible) contribution given by the HOMO (π_x) to LUMO (π^*_x) transition. The latter is responsible for the low oscillator strength of S_2, which would otherwise result in a dark (or very weak) state being HOMO-8 and HOMO-5 symmetrically perpendicular (y axis) with respect to LUMO (x axis).

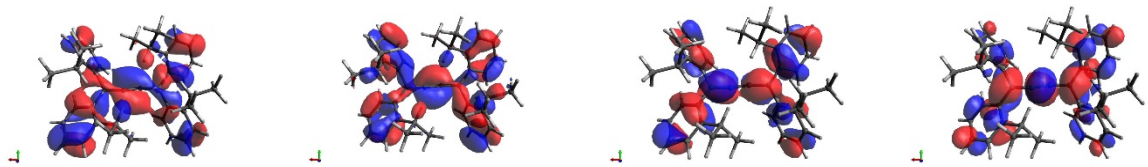

HOMO-8 (π_y) HOMO-5 (π_y) HOMO (π_x) LUMO (π^*_x)

Figure S76. DFT (wB97X-D3/cc-pVTZ) molecular orbitals involved in the description of S_1 and S_2 of **[3]*oi*Pr**.

TDDFT and TDA calculations provide very similar pictures (see data below) for the excited states, with TDA resulting - as expected - in higher vertical excitation energies than TDDFT.

We computed up to 40–50 excited states for each species. Here below are reported the 10 lowest-energy excited states.

TDDFT

State	Energy (cm-1)	Wavelength (nm)	fosc	T2 (au**2)	TX (au)	TY (au)	TZ (au)
1	**31377.5**	**318.7**	**0.770274106**	**8.08171**	**-2.82532**	**0.31508**	**-0.00085**
2	**33310.7**	**300.2**	**0.134889274**	**1.33312**	**-1.11697**	**0.29239**	**-0.00038**
3	40986.6	244.0	0.003898434	0.03131	0.16792	-0.05583	0.00011
4	41282.5	242.2	0.000617967	0.00493	0.00006	0.00018	0.07020
5	42450.1	235.6	0.055995920	0.43426	0.01055	-0.65890	0.00022
6	42525.7	235.2	0.000101813	0.00079	-0.00026	-0.00106	0.02805
7	42565.8	234.9	0.030633070	0.23692	-0.15382	-0.46180	0.00006
8	43653.0	229.1	0.007626372	0.05751	-0.00008	0.00007	0.23982
9	44610.0	224.2	0.002563418	0.01892	0.00003	-0.00025	-0.13754
10	45351.0	220.5	0.240735781	1.74755	-0.29109	-1.28950	0.00031

TDA

State	Energy (cm-1)	Wavelength (nm)	fosc	T2 (au**2)	TX (au)	TY (au)	TZ (au)
1	**32526.8**	**307.4**	**0.670988717**	**6.79125**	**-2.59457**	**0.24389**	**-0.00077**
2	**34177.9**	**292.6**	**0.473198742**	**4.55800**	**-2.09266**	**0.42283**	**-0.00068**
3	41519.7	240.8	0.007627850	0.06048	-0.23451	0.07407	-0.00013
4	41828.5	239.1	0.000515950	0.00406	0.00005	0.00016	0.06372
5	43047.8	232.3	0.036882459	0.28206	0.15972	-0.50651	0.00021
6	43110.8	232.0	0.000026292	0.00020	-0.00001	-0.00145	0.01409
7	43150.9	231.7	0.046631648	0.35577	-0.07576	-0.59163	0.00015
8	44726.0	223.6	0.010155294	0.07475	-0.00011	0.00005	0.27340
9	45433.1	220.1	0.000343240	0.00249	-0.00002	0.00014	0.04987
10	46188.0	216.5	0.267714311	1.90817	-0.18955	-1.36830	0.00034

As reported in the main text, the transient absorption spectra (TA, i.e., the S_1->S_n electronic transitions) have been computed at the TDA level by considering the following cases:

1) S_1->S_n transitions computed at the FC region, i.e., at the S_0 equilibrium geometry*;*
2) S_1->S_n transitions computed by displacing the carbon bonds of the chain (r_1, r_2, r_3) by following a stretching/shrinking pattern (different values of the displacement parameter δ), while keeping the end-to-end torsional angle τ = 0°;
3) S_1->S_n transitions computed for a slightly distorted end-to-end S_1 geometry (τ = 37°);
4) S_1->S_n transitions computed for a perpendicular end-to-end S_1 geometry (τ = 90°).

Case 1) can represent the very early stage of the photoexcitation, which is the creation of the excited state wavepacket in the S_1 FC region. Case 2) can describe the first ultrafast relaxation, where only *fast* carbon bonds stretching/shrinking changes occur. Case 3) can mimic the second *slow* relaxation, taking place on a longer time scale than the first, where the end groups start to rotate around terminal CC bonds of the cumulene chain, as facilitated by the reduced bond-order of the terminal carbon-carbon bonds (r_1 and r_3). Case 4) can represent the final relaxation steps, where the system starts to decay non-radiatively to S_0.

In **Figure S77** are reported the computed TDA transient absorption spectra (S_1-S_n) for the previous cases (1-4). For case 2), three spectra are reported differing by the displacement parameter (δ), namely by the amount of stretching for r_1/r_3 and shrinking for r_2 bonds (δ = 0.01 Å, δ = 0.03 Å, δ = 0.06 Å). In **Figure S77** is also reported the absorption spectrum related to the ground state electronic transitions (S_0->S_n).

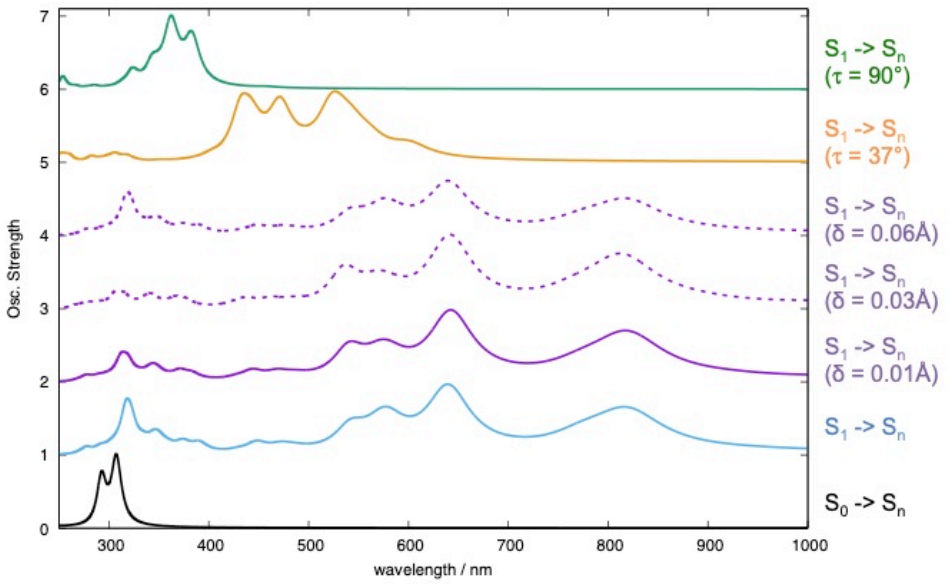

Figure S77. Computed TDA transient absorption spectra for S_i-S_j transitions of **[3]*oi*Pr** gas phase. Black line: S_0-S_n transitions calculated at the S_0 equilibrium geometry. Light blue line: S_1-S_n transitions calculated at the FC region (S_0 geometry). Purple (solid and dotted) lines: S_1-S_n transitions calculated by stretching r_1/r_3 and shrinking

r_2 according to a certain displacement δ. Yellow line: S_1-S_n transitions calculated for τ = 37°. Green line: S_1-S_n transitions calculated for τ = 90°. TDA energies are not scaled.

TDDFT and TDA excited states and transient absorption spectra: [5]*oi*Pr species.

For **[5]*oi*Pr** the first excited state S_1 is dark (2.9 eV, 426 nm, f = 0.0), being a HOMO-1 - LUMO transition, that is a π_y-π^*_x forbidden orbital excitation. The second excited state S_2 is dipole allowed (3.2 eV, 383 nm, f = 1.3) being described as a HOMO - LUMO allowed transition (π_x-π^*_x), **Figure S78**.

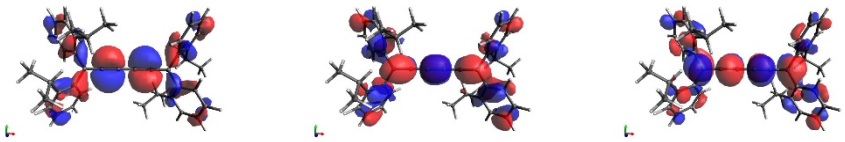

HOMO-1 (π_y) HOMO (π_x) LUMO (π^*_x)

Figure S78. DFT (wB97X-D3/cc-pVTZ) molecular orbitals involved in the description of S_1 and S_2 of **[5]*oi*Pr**.

TDDFT and TDA calculations provide very similar pictures (see data below) for the excited states, with TDA resulting - as expected - in higher vertical excitation energies than TDDFT.

We computed up to 40-50 excited states for each species. Here below are reported the 10 lowest-energy excited states.

TDDFT

Excited State	1:	Singlet-A	2.9134 eV	425.57 nm	f= 0.0000 <S**2>=0.000
Excited State	**2:**	**Singlet-A**	**3.2368 eV**	**383.05 nm**	**f= 1.2983 <S**2>=0.000**
Excited State	3:	Singlet-A	3.5424 eV	350.00 nm	f= 0.0000 <S**2>=0.000
Excited State	4:	Singlet-A	4.6864 eV	264.56 nm	f= 0.0000 <S**2>=0.000
Excited State	5:	Singlet-A	4.7950 eV	258.57 nm	f= 0.0643 <S**2>=0.000
Excited State	6:	Singlet-A	4.8019 eV	258.20 nm	f= 0.0000 <S**2>=0.000
Excited State	7:	Singlet-A	4.9068 eV	252.68 nm	f= 0.4217 <S**2>=0.000
Excited State	8:	Singlet-A	4.9656 eV	249.69 nm	f= 0.4779 <S**2>=0.000
Excited State	9:	Singlet-A	4.9742 eV	249.26 nm	f= 0.0000 <S**2>=0.000
Excited State	10:	Singlet-A	5.1025 eV	242.99 nm	f= 0.0000 <S**2>=0.000

TDA

State	Energy (cm-1)	Wavelength (nm)	fosc (au**2)	T2	TX (au)	TY (au)	TZ (au)
1	24693.8	405.0	0.000000087	0.00000	-0.00107	-0.00002	-0.00011
2	**28777.7**	**347.5**	**1.697917627**	**19.42390**	**4.37153**	**-0.00293**	**0.55999**
3	29948.7	333.9	0.000006205	0.00007	0.00819	0.00001	0.00104
4	41126.4	243.2	0.000030316	0.00024	-0.01435	0.00588	-0.00143
5	41170.2	242.9	0.120801032	0.96597	-0.91015	0.35967	-0.09070
6	41458.4	241.2	0.000000661	0.00001	0.00226	-0.00028	0.00020
7	42176.5	237.1	0.910988950	7.11080	2.63902	0.20750	0.32143
8	42360.9	236.1	0.185577450	1.44223	-1.14245	-0.36749	0.04462
9	42459.5	235.5	0.000001805	0.00001	0.00343	0.00146	-0.00027
10	44010.0	227.2	0.000040826	0.00031	0.00537	-0.01599	0.00456

In **Figure S79** are reported the computed TA spectra (S_2 -> S_n and S_1 -> S_n) at the TDA level of theory.

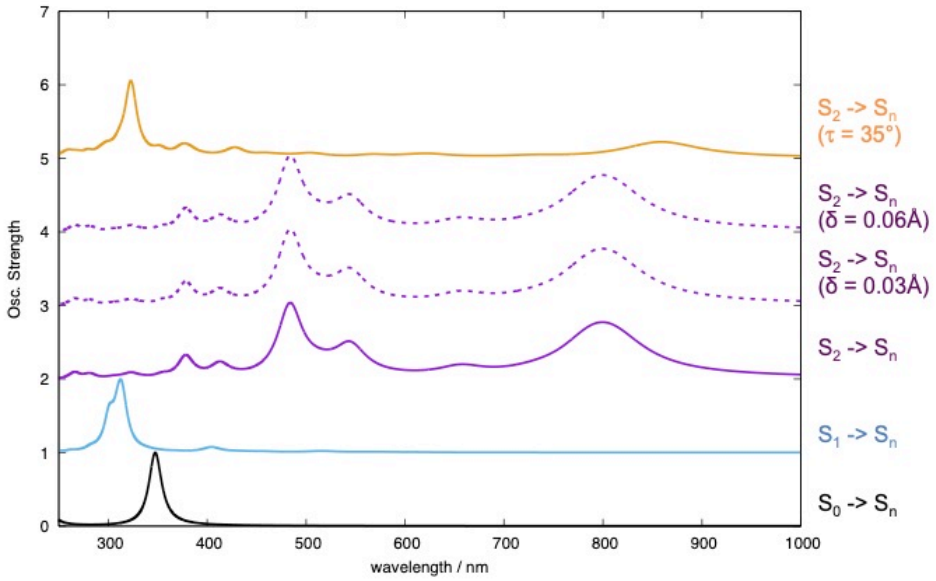

Figure S79. Computed TDA transient absorption spectra for S_1-S_n (light blue) and S_2-S_n (purple) transitions of **[5]*oi*Pr** at the equilibrium geometry of S_0. Black line: S_0-S_n transitions calculated at S_0. Purple (solid and dotted) lines: S_2-S_n transitions calculated by stretching bonds $r_1/r_3/r_5$ and shrinking r_2/r_4 according to a certain displacement δ. Yellow line: S_2-S_n transitions calculated for τ = 35°. TDA energies are not scaled.

TDDFT and TDA excited states and transient absorption spectra: [7]*oi*Pr species.

For **[7]*oi*Pr** the dipole allowed excited states are S_1 (2.28 eV, f = 0.039, H-1 -> L), S_2 (2.67 eV, f = 0.19, H -> L+1) and S_3 (2.84 eV, f = 1.11, H -> L), with the latter the brightest one (**Figure S80**).

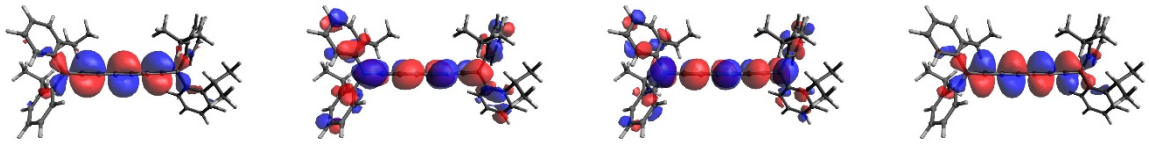

HOMO-1 (π_y) HOMO (π_x) LUMO (π^*_x) LUMO+1 (π^*_y)

Figure S80. DFT (wB97X-D3/cc-pVTZ) molecular orbitals involved in the description of S_1, S_2 and S_3 of [7]*oi*Pr.

TDDFT and TDA calculations provide very similar pictures (see data below) for the excited states, with TDA resulting - as expected - in higher vertical excitation energies than TDDFT.

We computed up to 40-50 excited states for each species. Here below are reported the 10 lowest-energy excited states.

TDDFT

Excited State 1:	**Singlet-A**	**2.2873 eV**	**542.05 nm**	**f= 0.0396**	**<S**2>=0.000**
Excited State 2:	**Singlet-A**	**2.6727 eV**	**463.90 nm**	**f= 0.1919**	**<S**2>=0.000**
Excited State 3:	**Singlet-A**	**2.8440 eV**	**435.94 nm**	**f= 1.1123**	**<S**2>=0.000**
Excited State 4:	Singlet-A	4.1868 eV	296.13 nm	f= 2.7595	<S**2>=0.000
Excited State 5:	Singlet-A	4.3085 eV	287.77 nm	f= 0.0064	<S**2>=0.000
Excited State 6:	Singlet-A	4.5620 eV	271.78 nm	f= 0.0032	<S**2>=0.000
Excited State 7:	Singlet-A	4.6472 eV	266.80 nm	f= 0.0635	<S**2>=0.000
Excited State 8:	Singlet-A	4.6476 eV	266.77 nm	f= 0.0283	<S**2>=0.000
Excited State 9:	Singlet-A	4.7060 eV	263.46 nm	f= 0.0004	<S**2>=0.000
Excited State 10:	Singlet-A	4.7913 eV	258.77 nm	f= 0.1273	<S**2>=0.000

TDA

ABSORPTION SPECTRUM VIA TRANSITION ELECTRIC DIPOLE MOMENTS

State	Energy (cm-1)	Wavelength (nm)	fosc	T2 (au**2)	TX (au)	TY (au)	TZ (au)
1	**19996.6**	**500.1**	**0.035515745**	**0.58471**	**-0.76039**	**-0.00001**	**-0.08077**
2	**23382.6**	**427.7**	**0.121113140**	**1.70520**	**-1.29923**	**-0.00001**	**-0.13114**
3	**25447.9**	**393.0**	**1.590975785**	**20.58199**	**-4.51785**	**-0.00002**	**-0.41352**
4	36103.8	277.0	3.260979054	29.73519	5.43306	0.00000	0.46590
5	37491.9	266.7	0.000669410	0.00588	0.00026	0.07667	0.00002
6	38638.4	258.8	0.016153469	0.13763	-0.00006	-0.37099	0.00000
7	39687.8	252.0	0.000808578	0.00671	-0.00026	-0.08190	-0.00001
8	40726.4	245.5	0.044728525	0.36156	-0.57226	-0.00018	-0.18462
9	40763.9	245.3	0.051577264	0.41654	0.00018	-0.64540	0.00006
10	41766.0	239.4	0.025578055	0.20161	-0.38465	0.00025	-0.23164

Following the previous cases (**[3]*oi*Pr** and **[5]*oi*Pr**) we computed the TA spectra - at the FC region - by assuming to populate both S_2 (S_2 -> S_n transitions) and S_3 (S_3 -> S_n). Furthermore, we have also computed the TA spectra from S_3 (S_3->S_n) by considering different displacement parameters δ (δ = 0.01 Å, 0.03 Å and 0.06 Å) and an end-to-end torsional angle τ (τ = 47°). Data are reported in **Figure S81**.

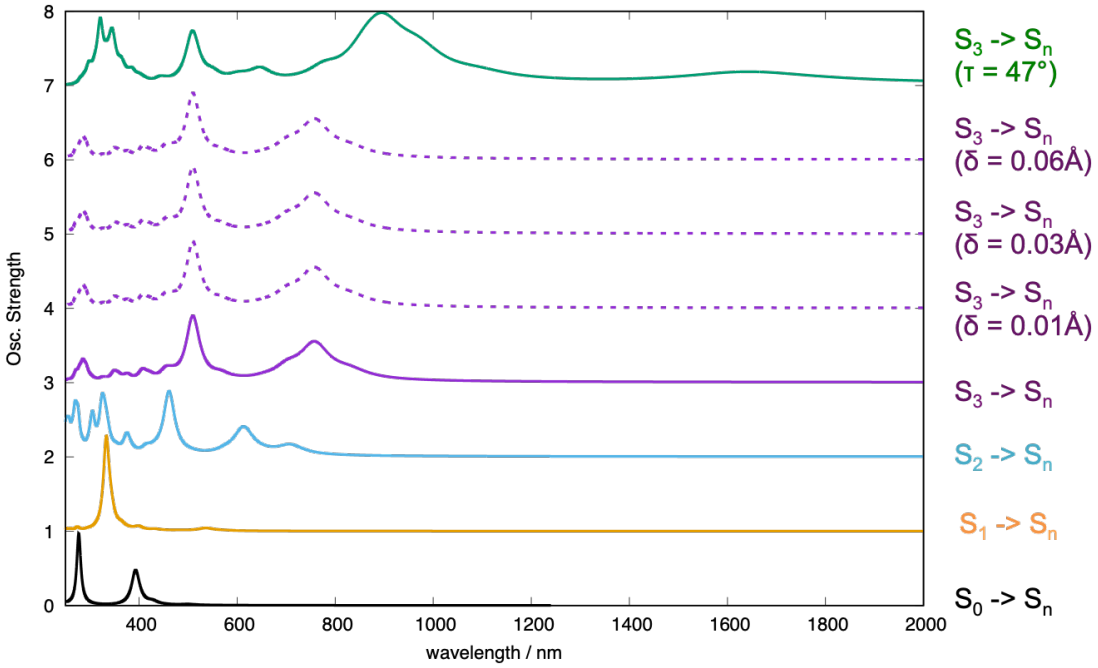

Figure S81. Computed TDA transient absorption spectra for S_1-S_n (yellow) S_2-S_n (light blue) and S_3-S_n (purple) transitions of **[7]*oi*Pr** at the equilibrium geometry of S_0. Black line: S_0-S_n transitions calculated at S_0. Purple (solid and dotted) lines: S_3-S_n transitions calculated by stretching bonds $r_1/r_3/r_5/r_7$ and shrinking $r_2/r_4/r_6$ according to a certain displacement δ. Green line: S_3-S_n transitions calculated for $\tau = 47°$. TDA energies are not scaled.

DFT/-/MRCI and CASSCF/NEVPT2 calculations

Table S11. Ground state wavefunction composition of **[5]*oi*Pr** and of the models **[5]H and [7]H.** From DFT/-/MRCI calculations.

[5]*oi*Pr

state	method	energy	delta e	eV	cm-1	nm
# 1 1a	DFTCI	-1624.722517		0.0000	0.	0.0

correlation energy (highest level) -0.065735

R	-0.9310150	(0.866789)	[GS, 0]	csf	1				
R	0.1074910	(0.011554)	[D , 0]	csf	1	148	148	149	149
R	0.0616602	(0.003802)	[D , 2]	csf	1	148	139	149	149
R	0.0413553	(0.001710)	[D , 0]	csf	1	147	147	150	150
R	-0.0259847	(0.000675)	[D , 4]	csf	1	147	148	149	150
R	0.0249010	(0.000620)	[D , 4]	csf	1	146	148	149	150
R	0.0186452	(0.000348)	[D , 4]	csf	2	147	148	149	150
R	0.0045063	(0.000020)	[D , 4]	csf	2	146	148	149	150

[5]*H*

# 1	1a	DFTCI	-1153.634938		0.0000	0.	0.0		

correlation energy (highest level) -0.065670

R	-0.9230466	(0.852015)	[GS, 0]	csf	1				
R	0.1326836	(0.017605)	[D , 0]	csf	1	290	290	417	417
R	0.0643997	(0.004147)	[D , 0]	csf	1	289	289	418	418
R	-0.0601009	(0.003612)	[D , 4]	csf	1	416	290	417	291
R	0.0441386	(0.001948)	[D , 4]	csf	1	289	290	417	418
R	-0.0431562	(0.001862)	[D , 4]	csf	2	416	290	417	291
R	0.0325924	(0.001062)	[S , 2]	csf	1	290	291		
R	-0.0316167	(0.001000)	[S , 2]	csf	1	416	417		
R	0.0287466	(0.000826)	[D , 0]	csf	1	416	416	417	417
R	-0.0254161	(0.000646)	[D , 4]	csf	1	416	289	418	291
R	0.0226021	(0.000511)	[D , 4]	csf	2	416	289	418	291
R	-0.0140449	(0.000197)	[D , 4]	csf	2	289	290	417	418

[7]*H*

state	method	energy	delta e	eV	cm-1	nm
# 1 1a	DFTCI	-1229.694207		0.0000	0.	0.0

correlation energy (highest level) -0.073799

R	0.9048958	(0.818836)	[GS, 0]	csf	1				
R	-0.1550454	(0.024039)	[D , 0]	csf	1	440	440	307	307
R	-0.0867462	(0.007525)	[D , 0]	csf	1	439	439	308	308
R	-0.0757031	(0.005731)	[D , 4]	csf	1	306	440	307	441
R	0.0608478	(0.003702)	[D , 4]	csf	1	439	440	307	308
R	-0.0588404	(0.003462)	[D , 4]	csf	2	306	440	307	441
R	-0.0537587	(0.002890)	[D , 2]	csf	1	437	440	307	307
R	0.0527024	(0.002778)	[S , 2]	csf	1	440	441		
R	0.0469678	(0.002206)	[S , 2]	csf	1	306	307		
R	0.0361073	(0.001304)	[D , 4]	csf	1	306	439	308	441
R	0.0325687	(0.001061)	[D , 4]	csf	1	437	439	307	308
R	-0.0311734	(0.000972)	[D , 0]	csf	1	306	306	307	307
R	-0.0304247	(0.000926)	[D , 4]	csf	2	306	439	308	441
R	-0.0273673	(0.000749)	[D , 0]	csf	1	440	440	441	441
R	-0.0196224	(0.000385)	[D , 4]	csf	2	439	440	307	308
R	0.0170074	(0.000289)	[D , 4]	csf	2	437	439	307	308

Table S12. Excited state wavefunction composition of **[5]*oi*Pr** and of the models **[5]H and [7]H**. From DFT/-/MRCI calculations. The state responsible for the absorption spectrum, dominated by the HOMO→ LUMO excitation, is considered.

[5]*oi*Pr

state	method	energy	delta e	eV	cm-1	nm
# 3	3a	DFTCI	-1624.616192	2.8933	23336.	428.5

correlation energy (highest level) -0.088286

R	0.9127050	(0.833030)	[S , 2]	csf 1	148 149	
R	0.1120775	(0.012561)	[S , 2]	csf 1	147 150	
R	-0.0637200	(0.004060)	[S , 2]	csf 1	146 150	
R	0.0400437	(0.001604)	[D , 2]	csf 1	147 148	149 149
R	-0.0293034	(0.000859)	[D , 4]	csf 1	146 147	149 150
R	0.0282511	(0.000798)	[D , 2]	csf 1	146 148	149 149
R	-0.0115409	(0.000133)	[D , 4]	csf 2	146 147	149 150

[5]*H*

state	method	energy	delta e	eV	cm-1	nm
# 2	1b1	DFTCI	-1153.547517	2.3789	19187.	521.2

correlation energy (highest level) -0.082433

R	-0.9076141	(0.823763)	[S , 2]	csf 1	290 417	
R	0.1141496	(0.013030)	[S , 2]	csf 1	289 418	
R	0.1090626	(0.011895)	[S , 2]	csf 1	289 417	
R	-0.0613063	(0.003758)	[S , 2]	csf 1	416 291	
R	-0.0581090	(0.003377)	[D , 2]	csf 1	416 290	417 417
R	0.0527750	(0.002785)	[S , 2]	csf 1	290 418	
R	-0.0412043	(0.001698)	[D , 4]	csf 1	416 289	417 418
R	-0.0344483	(0.001187)	[D , 2]	csf 1	290 290	417 291
R	0.0331655	(0.001100)	[D , 4]	csf 1	289 290	418 291
R	-0.0286538	(0.000821)	[D , 4]	csf 2	416 289	417 418
R	0.0226237	(0.000512)	[D , 4]	csf 2	289 290	418 291

[7]*H*

state	method	energy	delta e	eV	cm-1	nm
# 2	1b1	DFTCI	-1229.619603	2.0301	16374.	610.7

correlation energy (highest level) -0.089863

R	-0.8625980	(0.744075)	[S , 2]	csf 1	440 307	
R	-0.1954348	(0.038195)	[S , 2]	csf 1	439 307	
R	-0.1778657	(0.031636)	[S , 2]	csf 1	439 308	
R	0.1234448	(0.015239)	[S , 2]	csf 1	440 308	
R	-0.0624999	(0.003906)	[D , 2]	csf 1	306 440	307 307
R	0.0580041	(0.003364)	[T , 2]	csf 1	439 439	440 307 308 308
R	0.0578469	(0.003346)	[D , 4]	csf 1	306 439	307 308
R	0.0528035	(0.002788)	[D , 4]	csf 1	439 440	308 441
R	0.0524589	(0.002752)	[S , 2]	csf 1	306 441	
R	0.0459178	(0.002108)	[D , 2]	csf 1	440 440	307 441
R	0.0406392	(0.001652)	[D , 4]	csf 2	306 439	307 308
R	-0.0362525	(0.001314)	[D , 4]	csf 1	303 439	307 308
R	0.0359966	(0.001296)	[D , 4]	csf 2	439 440	308 441
R	-0.0267116	(0.000714)	[T , 2]	csf 1	439 440	440 307 307 308
R	-0.0235877	(0.000556)	[D , 4]	csf 2	303 439	307 308

Table S13. Ground state and excited state wavefunction composition (weights) of **[5]H and [7]H** from CASSCF(10,10)/def2SVP calculations.

[5]H
Ground state
0.84129 GR
0.05640 H,H→ L,L
Excited State (Bright)
0.70156 H→ L
0.10519 H-1→ L
0.04015 H→ L+2

[7]H
Ground state
0.82498 GR
0.07249 H,H→ L,L
Excited State (Bright)
0.69543 H→ L
0.05901 H-1→ L+1
0.04436 H-1→ L

Increased BLA in excited states of cumulenes dominated by the HOMO→LUMO excitation.

The following Figure shows the frontier orbital shapes for a model [7]cumulene **[7]H** and the corresponding oligoyne. The HOMO →LUMO excitation dominates the lowest bright excited states in these systems, however, the HOMO (and LUMO) of the cumulene and oligoyne have opposite bonding character, which justifies the decrease of BLA upon photoexcitation in oligoynes and the increase of BLA for the cumulenes investigated in this work. Specifically, in cumulene the HOMO is bonding on those CC bonds featuring longer bond length while the LUMO is bonding over the shorter (ground state) bonds. Upon excitation, the depletion of the HOMO and filling of the LUMO reinforces the bond order of shorter bonds which further shorten and reduces the bond order of longer bonds which further elongate, leading to an increased BLA in the excited state. The opposite occurs for the oligoyne.

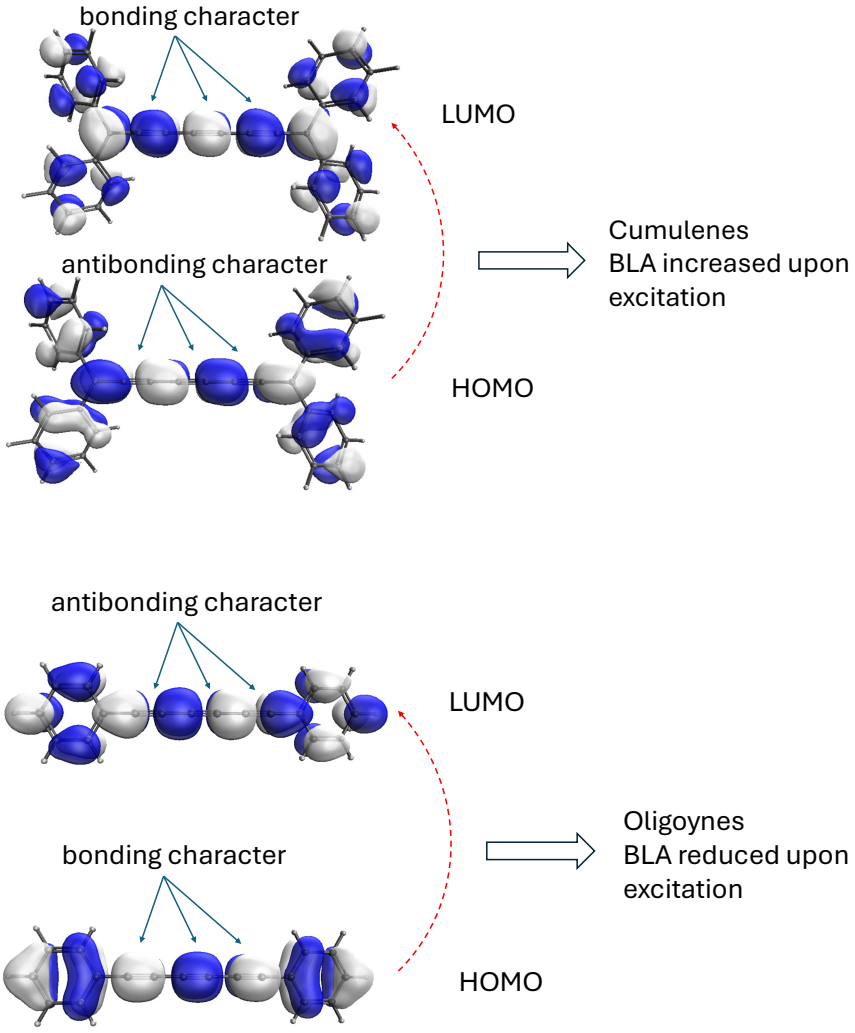

Figure S82. Frontier (HOMO and LUMO) molecular orbital shapes underscoring the local bonding and antibonding character for a model [7]cumulene and the corresponding oligoyne. The red dashed arrow schematically represents the electronic excitation dominating the bright excited state.

Conformational effects of solvation and their influence on the electronic structure

Methods.

To determine a reasonable set of explicitly solvated models of **[3]*oi*Pr** and **[5]*oi*Pr** we have added 25 solvent molecules around each solute. For computational simplicity, we have considered for both cumulenes just the two lowest energy conformations (see DFT section) and the lowest energy conformation of the solvent (trans conformation of 3-methylpentane). Each solvated model has been determined by a custom Monte Carlo approach determined with an in-house code based on OpenBabel and the MMFF94 molecular mechanics force field. Briefly, the solvent molecules are subsequently added to the solute selecting for each step the lowest energy configuration out of 1000 random placements of the solvent molecule in Van der Waals contact with the solute. After each placement of one solvent molecule the whole model is geometry optimized with the MMFF94 force field. Finally, the structure solvated with 25 solvent molecules is subjected to a full structure optimization (in gas phase) with Grimme's GFN2-xTB[7] method through the xtb code.[8] With this procedure, we have determined 1000 solvated models starting from each of the two low-lying conformers of **[3]*oi*Pr** and **[5]*oi*Pr.** The structures of these solvated models have been analyzed by considering the degrees of freedom that are relevant in the modulation of the π-conjugation along the cumulene chain.

We considered tetraphenylbutatriene (TPBT) as a simplified model to examine the effects on the electronic structure of the dihedral angles φ that define the relative position of the aryl planes with respect to the 2p lobes of the terminal sp^2-hybidized C atoms of the cumulene chain [9]. We computed by DFT at the B3LYP/6-31G(d,p) level the potential energy, frontier orbitals, and bond length alternation in TPBT as a function of the collective change of the φ dihedrals. This was done by a series of constrained optimizations in which the four φ angles (all identical) were varied between 130° and 160° with a 5° degrees step.

Results.

As reported in **Figure S83**, **[3]*oi*Pr** and **[5]*oi*Pr** display remarkably different behavior in the scatter plot of the energy of each solvated microstate *vs*. the deviation of each dihedral angle with respect to its average value across the solvated microstates (φ_i-$\langle\varphi_i\rangle$). Indeed, out of the same number of solvated microstates (1000), **[3]*oi*Pr** displays a limited number of states near the average energy (T = 300K). **[5]*oi*Pr** shows a markedly different situation, with a much broader distribution of states, which reflects the much more accessible surface of **[5]*oi*Pr** to the rather bulky solvent molecules (3-methylpentane). This allows the positioning of the solvent molecules in many more different ways, for limited changes of the interaction energy between the solvent and the solute. By converse, the bulky end-groups of **[3]*oi*Pr** are rather close because of the limited length of the cumulene chain, and this causes a significant reduction of the solvent-accessible surface of the solute.

Figure S84 reports the influence that the solvent has on the HOMO-LUMO gap of **[3]*oi*Pr** and [**5]*oi*Pr** because of its capability of influencing the φ dihedral angles. Following ref. [9] we introduce the average cosine of the four φ_i, i.e., $\xi = ¼(\cos\varphi_1 + \cos\varphi_2 + \cos\varphi_3 + \cos\varphi_4)$. For values of ξ approaching 1, the aryl substituents become

almost coplanar. The value $\xi = 1$ cannot be reached because of the steric hindrance of the two nearby aryl groups on each end of the cumulene. In **Figure S84** we recover a trend of decreasing H-L gap for increasing co-planarity. This behavior indicates the increase of π-conjugation across the cumulene and the aryl substituents, and it is consistent with the observed trend of the decreasing wavenumber of the ECC Raman band of aryl capped cumulenes recently reported.[5] Notably, in **Figure S84** it is also clear the much-reduced spread of thermally accessible microstates of **[3]*oi*Pr** compared to **[5]*oi*Pr** (green dots), which reflects the comments made about **Figure S83**.

Finally, by constrained optimization of the four dihedral angles φ_i of tetraphenylbutatriene, we could show how the aryl conformation influences the π-conjugation across the cumulene bridge (see Methods for details). As shown in **Figure S85** the curvature of the PES along the dihedral angle $\theta = \varphi + 180°$ is rather flat, and for a kT value of 0.6 kcal/mol (approximately corresponding to T = 300K) we may expect variations of the dihedral angles of the order of 10°. These variations are compatible with the fluctuations of the φ dihedral angles observed in the solvated microstates described in **Figure S83**. Moreover, as shown in **Figure S85**, the co-planarization of the aryl moieties clearly affects the bond length alternation and the HOMO-LUMO gap, which fully explains the trend observed in **Figure S84**. Notably, the BLA increases for increased conjugation with the terminal aryl groups. This is a rather uncommon behavior in π conjugate molecules, where usually BLA decreases for increasing conjugation. This apparently contrasting trend can be readily rationalized by considering that in cumulenes the effects of two sets of p orbitals, one perpendicular to the other, sum up. As a result, compared to butadiene where the central CC bond is the longest, in **[3]*oi*Pr** the central bond (r_2) is the shortest. In **[3]*oi*Pr**, for increasingly co-planarization of the aryl moieties, the increasing delocalization of the p system perpendicular to the molecular plane will further shorten the central bond r_2 (increased bond order) and elongate the terminal r_1 and r_3 bonds (due to a decreased bond order). As a result, the BLA increases. The second p-system, lying in the molecular plane, will also reinforce the central bond (increase the bond order) since one may assume that the two terminal "p" orbitals of the cumulene chain will be more strongly involved in the formation of the σ C-C bonds to the aryl groups and will reduce their contribution to the p orbital set lying in the molecular plane, that will be therefore strongly localized on the central CC bond of the cumulene chain. Thus, such central bond will shorten also due to this effect, thereby further increasing the BLA.

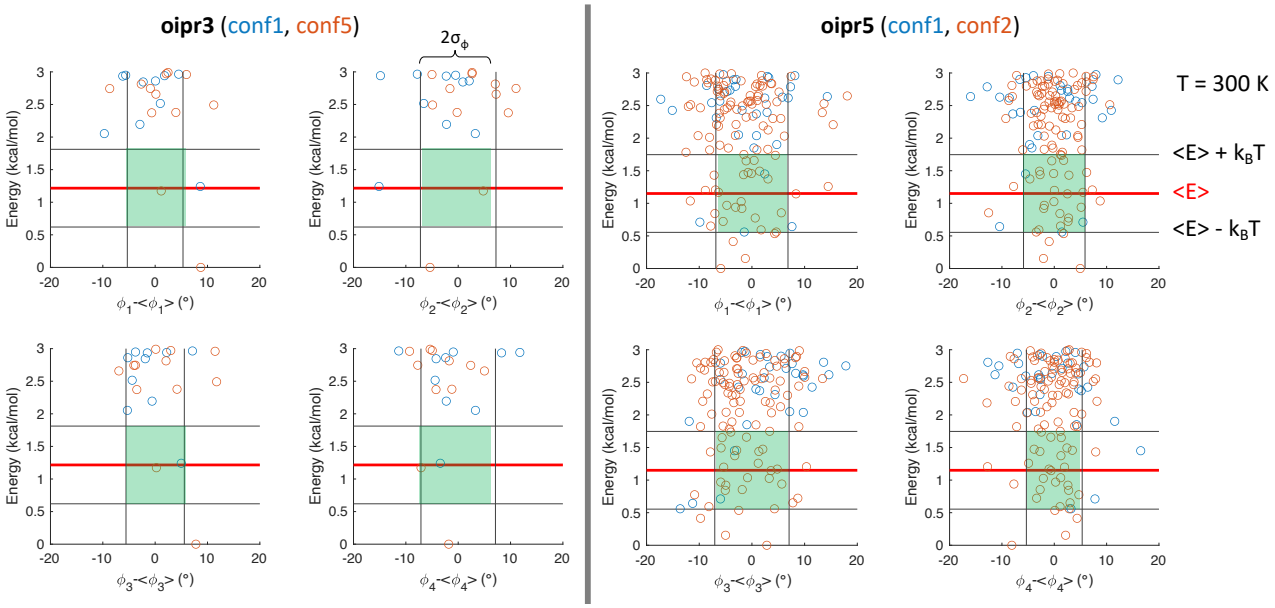

Figure S83. Scatter plot of the energy of the solvated microstates of the two lowest energy conformers of **[3]*oi*Pr** and **[5]*oi*Pr** (for each molecule, the energy is relative to the solvated microstate of minimum energy, min(min(E_a), min(E_b)) – E_a and E_b are the vectors of the energies of the solvated microstates for the two conformers considered for each molecule. The vertical black lines denote the standard deviation interval (±σ) of the φ angles. The energies of the solvated microstates have been computed on structures fully optimized with the GFN2-xTB method.[3] The average energy is defined as $\langle E \rangle = \frac{1}{Z}\sum_j E_j \; e^{-\frac{E_j}{k_B T}}$, where Z is the partition function. The data shown are obtained from 1000 solvation microstates computed for each conformer.

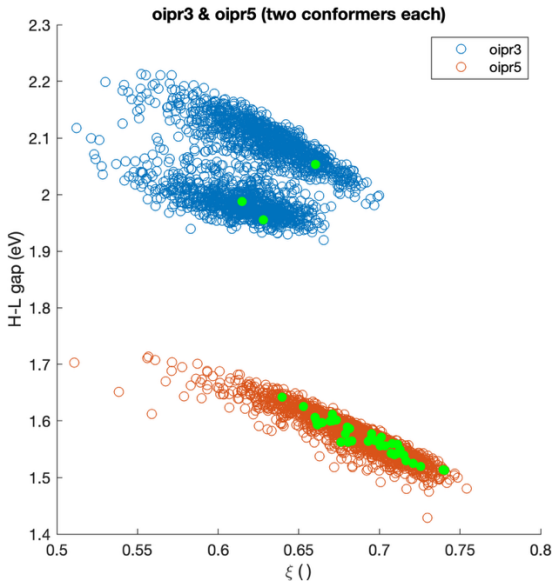

Figure S84. Scatter plot of the HOMO-LUMO gap of the solvated microstates of the two conformers of **[3]*oi*Pr** and **[5]*oi*Pr** here considered (see methods). For **[3]*oi*Pr** the two conformers show distinguishable clustered data, whereas for **[5]*oi*Pr** the two conformers produce an overlapped distribution. The green dots denote those microstates that are comprised between <E> – kT and <E> + kT (they are found within the energy ranges defined in Figure S83).

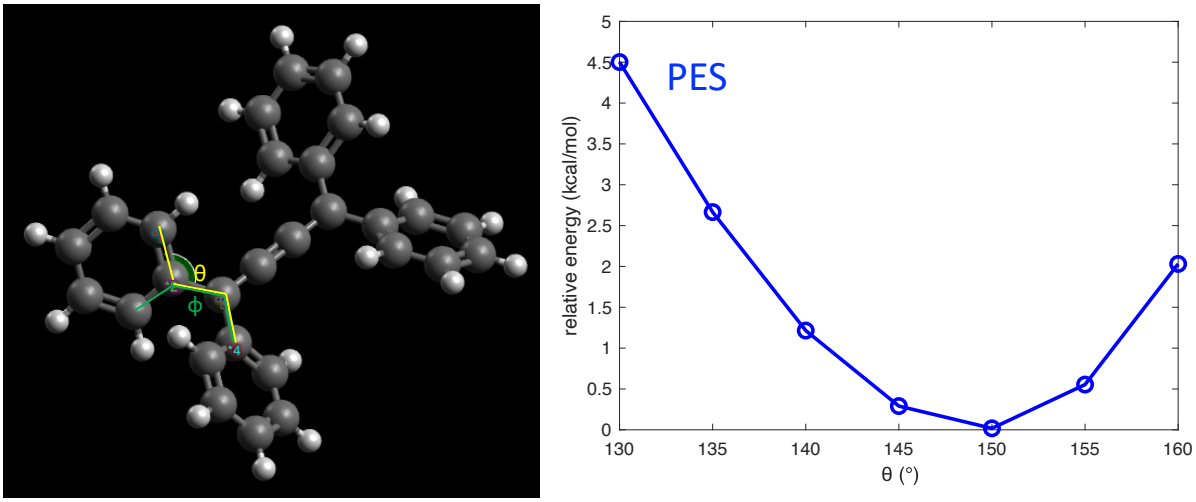

Figure S85. Definition of the dihedral angles φ and θ = φ + 180° (left panel) and the potential energy surface V(θ) obtained by constrained optimization of the four dihedral angles θ (right panel). In the calculation of V(θ) the four dihedral angles have been changed simultaneously.

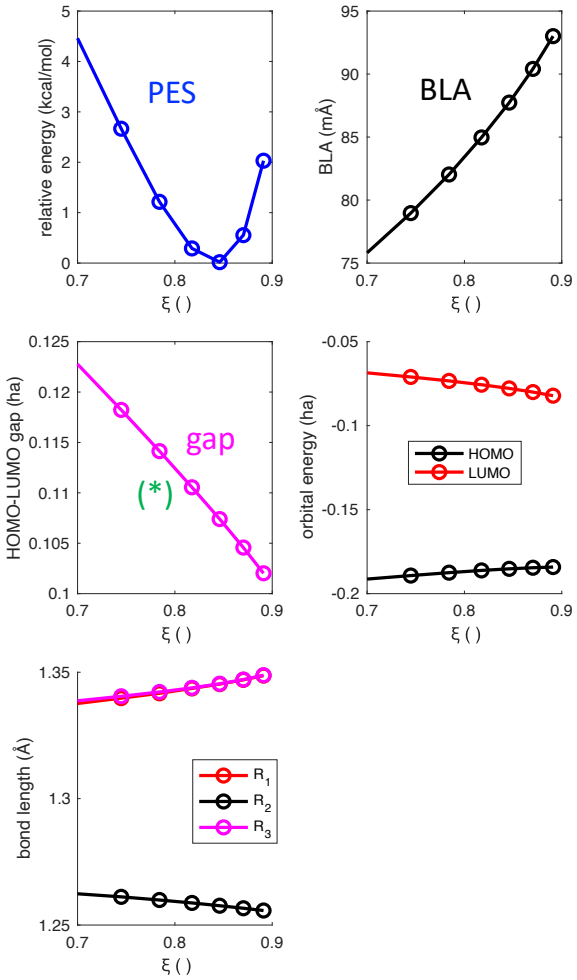

Figure S86. The behavior of different molecular properties as a function of the ξ parameter that describes the planarization of the structure of tetraphenylbutatriene for changing values of the φ dihedrals during the constrained geometry optimization with B3LYP/6-31G(d,p) method (see text for details).

Furthermore, we have considered also the solvation of **[7]*oi*Pr** within the same computational setup adopted for **[3]*oi*Pr** and **[5]*oi*Pr,** and we have compared the behavior of this long cumulene with the shorter **[3]*oi*Pr** and **[5]*oi*Pr**. The results are reported in **Figure 9a** in the main text. As expected for cumulene derivatives of increasing length, the HOMO-LUMO gaps reported in **Figure 9a** follow a decreasing trend moving from **[3]*oi*Pr** to **[7]*oi*Pr**. The center of the distribution of the data points for the three molecules suggest progressive increase of the mean ξ value, which corresponds to a progressive co-planarization of the aryl groups (of course the ξ value of 1 cannot be reached due to hindrance of the adjacent aryl moieties on each end of the cumulenes). This observation may be taken as indication of the progressive relief, for increasing chain length, of the direct interaction between the bulky end groups at the two ends of the cumulenes. The increasing distance between the two ends leaves more space for the solvent molecules to surround the cumulene chain and, at the same time, allow for a more planar conformation at each end. As displayed in Figure 9b of the main text, the distribution of the distances between the center of mass of the cumulenes and the center of mass of the surrounding solvent molecules (defined in **Figure S87**) confirms this scenario. With reference to **Figure 9b** and **S87**, the peak of the distribution at small distances is confirmed (by inspection of representative solvated structures – **Figure S87**) to correspond to the solvent molecules that are nearby the center of the cumulene chain. As the chain length of the cumulene increases, and the end groups progressively get far apart, there is more space available to the solvent for reaching the center of the cumulene chain. This implies a shift of the low-distance peak of the distribution to shorter distances as the chain length increases – which is evident in **Figure 9b**. The direct inspection of the equilibrium geometries of representative solvated structures reveals that the more intense and structured peak at larger distances represents the solvent molecules surrounding the end groups of the cumulenes. As expected, the position of this peak increases for increasing chain length since it is a measure of the distance between the center of the cumulene and its ends.

Finally, the distribution of the end-to-end dihedral angle τ shows a significant broadening moving from **[3]*oi*Pr** to **[5]*oi*Pr** and **[7]*oi*Pr** (**Figure S88**). This clearly indicates the increased intra-molecular conformational freedom of the two longer cumulenes, which is possible because of the larger distance between the end groups, which implies a reduced intramolecular hindrance.

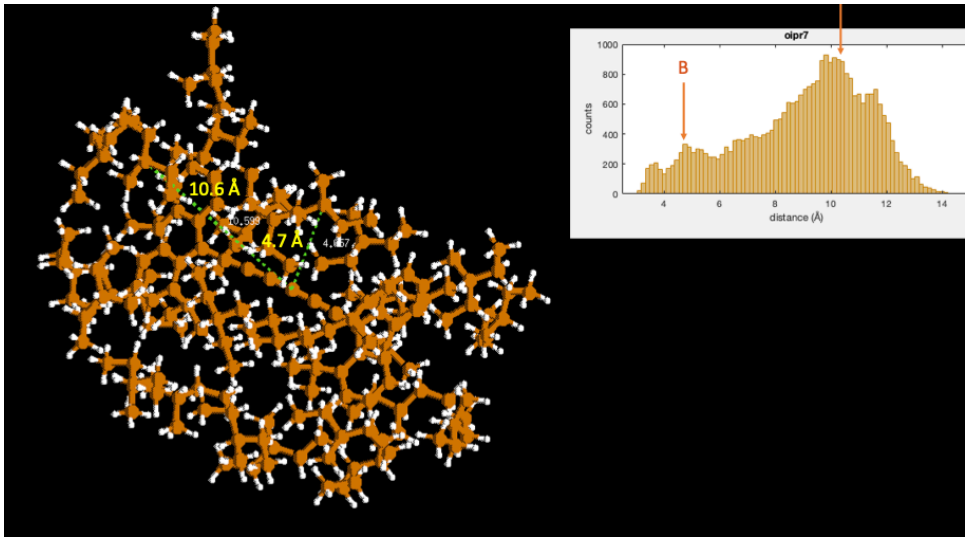

Figure S87. Representative equilibrium structure of solvated **[7]*oi*Pr** showing the distances between the center of mass of the cumulene chain and the center of mass of solvent molecules in the vicinity of the center of the sp-chain (B) and in the vicinity of one of the end groups (A).

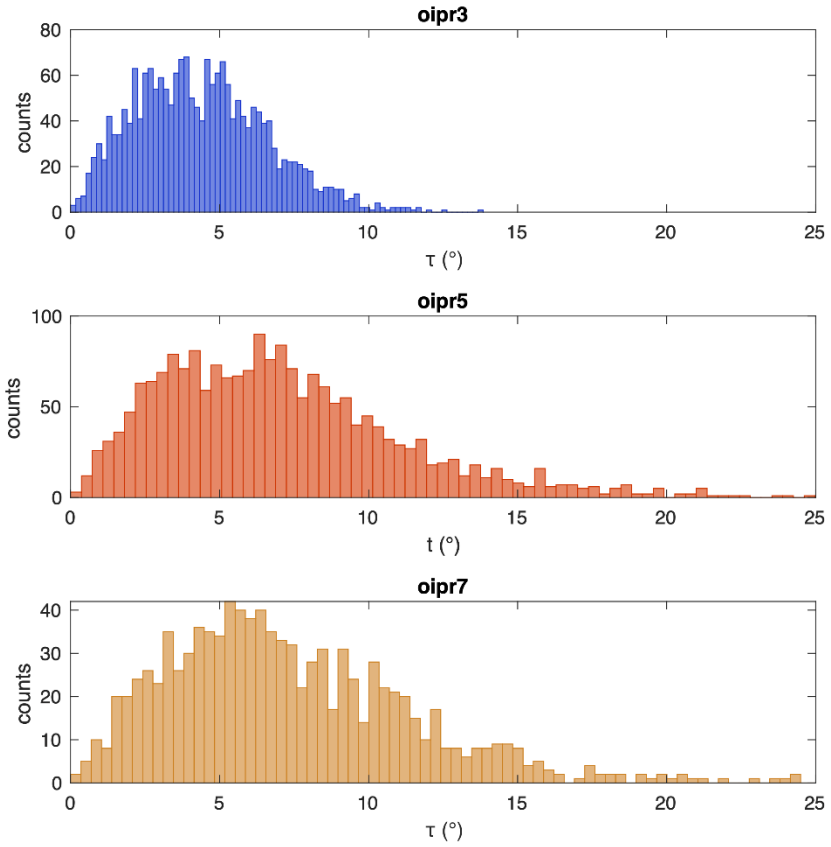

Figure S88. Distribution of the end-to-end dihedral angle τ in the solvated equilibrium structures of the three cumulenes.

XYZ optimized coordinates (ground state)

Equilibrium S_0 structure for **[3]*oi*Pr** *conf1*, wB97X-D/cc-pVTZ

84 Coordinates from ORCA-job oipr3_wb97xd3

C	-0.63125646956199	0.02687457377021	1.05675539277947
C	-1.94153192966708	0.02182393235002	0.90682890366511
C	0.63074156402383	-0.02613592836165	1.05720392644568
C	1.94109567258819	-0.02132843884775	0.90793585441784
C	-2.76316202554988	1.25994442064672	0.80292201138926
C	-2.64805749468655	-1.29465872669867	0.85966671639886
C	2.64764202806411	1.29514660941092	0.86035878340550
C	2.76275390475544	-1.25950947987608	0.80522284629669
C	-3.33029607791393	-1.69439774732318	-0.29666411617449
C	-3.98054224201473	-2.92697843522969	-0.28503875984112
C	-3.94861298321963	-3.75477945212464	0.82834961961102
C	-3.25088375831175	-3.36081072416333	1.96269162093199
C	-2.60549368340240	-2.13338705348322	1.97215057959943
C	-2.41527773799341	2.36351103980793	0.00618000038655
C	-3.96588732299596	1.27609247539336	1.51823784682650
C	-4.81094430260185	2.37097878452727	1.48567589957111
C	-4.46446014518857	3.47215707290690	0.71251972821910
C	-3.28500268421191	3.45530365623211	-0.01439008482112
C	2.41524419067678	-2.36356761783789	0.00901761543122
C	3.28495269936098	-3.45539642788193	-0.01043987564420
C	4.46404627254501	-3.47182370193826	0.71706349117836
C	4.81016372296018	-2.37016670629822	1.48971495955554
C	3.96511611344834	-1.27524547849762	1.52116991490003

C	2.60446328364033	2.13453443189565	1.97232056432012
C	3.24976688471429	3.36200365504951	1.96245036853764
C	3.94801382085596	3.75535590735080	0.82821611933114
C	3.98055986298216	2.92688964246074	-0.28466254401480
C	3.33043232944514	1.69424318279926	-0.29586937541758
C	-1.15818394373251	2.41604005071822	-0.84602979648889
C	-0.13301097815648	3.37204762242222	-0.22825128122115
C	-1.46370006713115	2.79856126283964	-2.29812030082344
C	-3.33779474305928	-0.84164080222900	-1.55384475406355
C	-2.82522781764949	-1.62145069948391	-2.76847371011007
C	-4.72428393263244	-0.24734493008602	-1.81492783643363
C	1.15854618549994	-2.41658941113734	-0.84373353531448
C	1.46471408197794	-2.79998424665871	-2.29544805636356
C	0.13305715769326	-3.37215302381521	-0.22580160622234
C	3.33864634201412	0.84071301256262	-1.55252753606595
C	2.82682234326307	1.61977125048492	-2.76795261838584
C	4.72528111111115	0.24624476550283	-1.81244177269797
H	-4.46131688813168	-4.71040473534651	0.80646133307176
H	-4.51394537160977	-3.25437119387873	-1.17141475760259
H	-3.21045227950824	-4.00397167009542	2.83478900308953
H	-2.05557177771373	-1.80808608602865	2.84883244191429
H	-5.73425822603768	2.36336447437679	2.05418365366285
H	-4.23309457800536	0.40539054148359	2.10691789051231
H	-5.11471218397278	4.33924160474187	0.66905597749739
H	-3.03258755605040	4.31634856399023	-0.62341830416827
H	4.51435391148500	3.25380659149126	-1.17097890082779
H	4.46064546107230	4.71101197251596	0.80600680107626
H	3.20886763692549	4.00567648532788	2.83414815958199

H	2.05413225115379	1.80971843910532	2.84892566249569
H	4.23203758216872	-0.40419121640424	2.10945817179469
H	5.73318020736460	-2.36222181021623	2.05870114827230
H	5.11429098631443	-4.33895591336635	0.67448096455787
H	3.03280514118855	-4.31682999888462	-0.61902932241782
H	-0.71718363555648	1.41936140887893	-0.86149207549363
H	-2.64587162985684	-0.01363463685374	-1.39594972684155
H	0.71758997636377	-1.41990386597308	-0.85998436906627
H	0.10573506938108	3.08002427685421	0.79508658592002
H	-0.52393067130904	4.39369008172037	-0.20949989163759
H	0.79826600994988	3.37360268086915	-0.80003785427976
H	-1.81884970695713	3.82847175557376	-2.38193486476832
H	-2.22622273417816	2.14354387910152	-2.72831291789925
H	-0.55892776162673	2.71432458711572	-2.90582615280882
H	-3.49089835898094	-2.44839526062690	-3.02882470431160
H	-1.83265613589919	-2.03478605971217	-2.57533323044421
H	-2.75671812488482	-0.96327787559998	-3.63889227278839
H	-5.04486334383947	0.37659179991815	-0.97822802715089
H	-5.46597527942143	-1.03922797749895	-1.95450242642569
H	-4.71313717365011	0.36960364833414	-2.71806486384353
H	1.81987804679241	-3.82995498869259	-2.37846893005366
H	2.22745897393363	-2.14525296390333	-2.72567958336722
H	0.56023053476691	-2.71607966480050	-2.90362718539148
H	-0.79797875641921	-3.37402032810958	-0.79797677896350
H	-0.10610485658753	-3.07944264045770	0.79724352346830
H	0.52390100188831	-4.39380936514847	-0.20620691145322
H	3.49278613369125	2.44640588366758	-3.02853924000254
H	1.83422790137971	2.03342496558496	-2.57560846635021

H	2.75863425123962	0.96101269789140	-3.63795190017312
H	4.71466392223426	-0.37122827621154	-2.71522742967541
H	5.04536152499470	-0.37721366700993	-0.97519401374532
H	5.46706344723288	1.03803940946687	-1.95203710385428
H	2.64661962373619	0.01281374405004	-1.39452730100326

Equilibrium S_0 structure for **[3]*oi*Pr** *conf2*, wB97X-D/cc-pVTZ

84 Coordinates from ORCA-job oipr3_conf5_wb97xd3

C	-0.63022941290344	-0.00246138488086	0.02581788984641
C	-1.93412788491755	0.19166314518627	0.14200042646134
C	0.63243170417972	0.00227988854695	-0.02553130526157
C	1.93635830348107	-0.19231645483327	-0.14054100894589
C	-2.31764951175301	1.57519740355651	0.58569173482354
C	-3.01984346755681	-0.79200761741363	-0.10209919914210
C	3.02216474819169	0.79130292897167	0.10347640635647
C	2.31983230255152	-1.57611647506564	-0.58342770134924
C	-2.86528036480300	-2.01160816610476	-0.79888358460922
C	-3.99471115404505	-2.80452638025076	-0.99521653001899
C	-5.24833896718638	-2.44432996209040	-0.52302695780972
C	-5.39706108088532	-1.25636394761248	0.17533990432670
C	-4.29251846264818	-0.44664179717609	0.37426734855862
C	-2.87393673481759	2.49490258344524	-0.30946072974348
C	-2.08391976772641	1.94001239253463	1.91030909409005
C	-2.39884582370600	3.21191299230418	2.36409496666808
C	-2.94594279262792	4.13390575033481	1.48069059285255
C	-3.17493327698329	3.77259139476899	0.16054835914821
C	2.87610048532349	-2.49536304872086	0.31221999071517
C	3.17697540319684	-3.77332826713124	-0.15709010540936
C	2.94778167184715	-4.13544281745759	-1.47697696912258
C	2.40061972203255	-3.21394690640073	-2.36086104523803
C	2.08583463754014	-1.94175839023147	-1.90778665414333
C	4.29467557382482	0.44601167054038	-0.37335680844123
C	5.39928733258477	1.25569535788122	-0.17460650683267

C	5.25078354483871	2.44351083219193	0.52405471314619
C	3.99729758890342	2.80365413909440	0.99667070502183
C	2.86780318787108	2.01079365216154	0.80049980680551
C	-3.12110267154925	2.14072468574763	-1.76465732868152
C	-2.21134896480079	2.95661875397692	-2.68790035348502
C	-4.59469801722113	2.30950404882086	-2.14409613708019
C	-1.51946758580087	-2.51060644178519	-1.28863378390817
C	-0.80903647779290	-3.25823896110778	-0.15234660777274
C	-1.59475723138923	-3.39298709142746	-2.53612131778322
C	3.12325923283278	-2.14047268691444	1.76725393704094
C	2.21358869521444	-2.95599978416500	2.69091238492581
C	4.59686753745553	-2.30897135848269	2.14674051717322
C	1.52213601010461	2.50970192531522	1.29068648641120
C	1.59783940585544	3.39163649417177	2.53847046649235
C	0.81150458493267	3.25775961067193	0.15481924442647
H	-6.10037709105098	-3.09186899027275	-0.70016575660156
H	-3.89299145193600	-3.73675041444887	-1.53675990961656
H	-6.36538432195197	-0.95545332225827	0.55963326003818
H	-4.41491179687199	0.48343470861791	0.91447253051501
H	-2.21578501725235	3.48235736070297	3.39823747028963
H	-1.65025174275405	1.20916487737213	2.58471279602244
H	-3.19312632106859	5.13464372906511	1.81819966165441
H	-3.59420494843970	4.50411197180450	-0.52233826892687
H	3.89576344078092	3.73576796192269	1.53845973799113
H	6.10288536345532	3.09099631091195	0.70108346415591
H	6.36748712120947	0.95486173302663	-0.55927170897860
H	4.41687688844773	-0.48396172775370	-0.91377962574130
H	1.65213583675318	-1.21128408260261	-2.58257258817136

H	2.21739870590027	-3.48498406102376	-3.39481970857909
H	3.19482127211305	-5.13641478745476	-1.81389807639785
H	3.59621901063702	-4.50449139470670	0.52619947436619
H	-2.86575450395796	1.08825638178515	-1.90010815726805
H	-0.91469080161185	-1.64176878857838	-1.55055092238050
H	2.86781303915749	-1.08797835655465	1.90222218323942
H	-1.16034741238810	2.81541744899832	-2.42565631343937
H	-2.43483501110368	4.02490550324489	-2.61708203500584
H	-2.35225628431426	2.65033762904015	-3.72814623659450
H	-4.75972265554627	1.98998237747719	-3.17661254845166
H	-4.90809320215160	3.35396335672847	-2.06247105824150
H	-5.23629959298223	1.70896968208703	-1.49554539130008
H	0.19314207466069	-3.56619072007039	-0.45702546025129
H	-1.38106296228463	-4.15070413265294	0.11950362672910
H	-0.71830938325051	-2.63081269028272	0.73573309759078
H	-2.03677734987472	-4.36974689216786	-2.32305009449301
H	-0.58373259681224	-3.57298409777318	-2.90912455315651
H	-2.17723230585571	-2.91927146091556	-3.33054186507583
H	1.16257367786234	-2.81504706596812	2.42858627979449
H	2.35446764233494	-2.64918298958928	3.73100356679724
H	2.43719227450146	-4.02429901181798	2.62063646320716
H	4.76187900563620	-1.98903295526915	3.17912909063078
H	5.23840919132805	-1.70863831231229	1.49794542441605
H	4.91032693858376	-3.35344360489743	2.06551399727645
H	0.58694842716589	3.57159437077963	2.91185529767167
H	2.03990490135296	4.36842217753911	2.32560753422597
H	2.18049700607788	2.91758491447939	3.33255709584714
H	-0.19067669299074	3.56545858160090	0.45974187709786

H	0.72076013482338	2.63072847810201	-0.73354306492284
H	1.38341719252319	4.15040426014937	-0.11668540103895
H	0.91742113139661	1.64077331636508	1.55242559736378

Equilibrium S_0 structure for **[5]*oi*Pr**, wB97X-D/cc-pVTZ

86 Coordinates from ORCA-job oipr5_wb97xd3

C	1.87822535652567	0.16667097778945	0.30585928059403
C	3.17973438531845	0.25013317500388	0.49961342197623
C	0.63207400790608	0.06129177332683	0.10636727679173
C	-0.63177566914692	-0.06110230387760	-0.10651777649298
C	-1.87791005200481	-0.16655334598000	-0.30606826061166
C	-3.17938694575118	-0.25017755257862	-0.49999193883011
C	3.87373885407738	1.56861013189628	0.39921365842454
C	3.98283877077857	-0.93005797764452	0.93191654029652
C	-3.98262881732057	0.92984158818388	-0.93249769350330
C	-3.87332441513212	-1.56864828301357	-0.39917527899454
C	3.91672469201036	-2.18493480932026	0.30959507359092
C	4.70136224170673	-3.21582000560408	0.83008193485295
C	5.53220022574010	-3.02654758508023	1.92258018662996
C	5.60876949951453	-1.77426194609462	2.52048537888207
C	4.84311722860175	-0.73731053630236	2.01827588703590
C	4.95108048334370	1.75312983624169	-0.47841635701017
C	3.45527408758602	2.61267439019108	1.22399151970353
C	4.11188238718130	3.83374497505954	1.21408160555730
C	5.19909073993088	4.01498544798761	0.36931709456183
C	5.60275670518307	2.98491280220499	-0.46838837283411
C	-4.95052369261782	-1.75290602038702	0.47867089713200
C	-5.60216395194089	-2.98471034440569	0.46915535063734
C	-5.19860145352489	-4.01504435839972	-0.36828124609381
C	-4.11152754053287	-3.83404442508396	-1.21327688963561
C	-3.45494830763214	-2.61296181112124	-1.22368024233319

C	-4.84263651588607	0.73685768936058	-2.01903099416397
C	-5.60845186755713	1.77359267989776	-2.52142843132817
C	-5.53237967173173	3.02589634789479	-1.92350109762014
C	-4.70188883187725	3.21538264459954	-0.83077804942158
C	-3.91706908506647	2.18472529571375	-0.31011095067424
C	5.38550001795355	0.66992129634210	-1.45096811749407
C	6.72678800418626	0.05251449702660	-1.04469587559933
C	5.43043166873056	1.18928476796869	-2.89156236667741
C	3.06099836978101	-2.45755716050741	-0.91503662049977
C	3.88338024936027	-3.06398728572780	-2.05750846627661
C	1.86609772392545	-3.34781135968722	-0.55940508159827
C	-5.38481961291107	-0.66936412566604	1.45090474860466
C	-6.72639861068432	-0.05243383022193	1.04488140656927
C	-5.42907030821353	-1.18810832468084	2.89174262493379
C	-3.06200268512940	2.45754114013716	0.91493826552128
C	-1.86728781352963	3.34831676860286	0.55998138866488
C	-3.88517269118942	3.06350669377221	2.05708737463736
H	6.12539767875245	-3.85185315244922	2.30131563180372
H	4.66204543723100	-4.19366445245323	0.36238776699410
H	6.26157912446012	-1.60711244260396	3.36993177327750
H	4.90114625738025	0.24673506770081	2.47026834563341
H	3.78147351600552	4.63477462614251	1.86598689156853
H	2.61199558554679	2.44720746898555	1.88579344947487
H	5.72774448260392	4.96203784591055	0.35417787600191
H	6.43960610468018	3.14692175888011	-1.13935590706719
H	-4.66302352985455	4.19321436782806	-0.36301982793135
H	-6.12573659701300	3.85103102943526	-2.30236069654085
H	-6.26102817722126	1.60625551385013	-3.37101696714196

H	-4.90030142610065	-0.24720682222225	-2.47102471409982
H	-2.61176818213744	-2.44768559246649	-1.88565608757373
H	-3.78120071777797	-4.63527863983571	-1.86497358676375
H	-5.72723682027604	-4.96210029938811	-0.35276072263015
H	-6.43891917304579	-3.14651085145506	1.14029125147818
H	4.63164772102533	-0.11823862028446	-1.42282961745390
H	2.66803763242333	-1.50458339037818	-1.27091044206409
H	-4.63115504273533	0.11896012001308	1.42212738037571
H	6.67134545316376	-0.38955757711179	-0.04852921701465
H	7.51530622244795	0.81081734296743	-1.03938347101559
H	7.01642181544284	-0.73048991202720	-1.75139460595354
H	5.62967331970818	0.36438979710827	-3.58112506830089
H	6.22115701109427	1.93158676812281	-3.02776571490438
H	4.48109357594952	1.65092630632679	-3.17325321273060
H	4.75420330709472	-2.44524263924006	-2.28959689900177
H	3.27049539464407	-3.14328762639217	-2.95926966289909
H	4.24103685712931	-4.06704743829635	-1.81188075100400
H	1.25541256850597	-2.88866280876331	0.22036062448992
H	2.20381565430473	-4.32346133980885	-0.19756490875359
H	1.23469977746493	-3.51097443537542	-1.43714469809078
H	-7.51476869685199	-0.81089520364860	1.04028904933244
H	-6.67146350251005	0.38914265561856	0.04846660556940
H	-7.01589046402260	0.73087186533012	1.75130455736870
H	-6.21955650942908	-1.93054977791109	3.02856931498677
H	-5.62825234393132	-0.36296351716874	3.58102278667137
H	-4.47951010393525	-1.64939130925244	3.17327042139369
H	-1.25605776837512	2.88951614617629	-0.21955860175888
H	-1.23636274937045	3.51161213009511	1.43803620279521

H	-2.20522711777198	4.32387794442268	0.19811080880529
H	-4.75585949419294	2.44437968945610	2.28867864999425
H	-4.24311086201765	4.06645641678631	1.81141774333615
H	-3.27275259534421	3.14293645155459	2.95915321366733
H	-2.66884378310585	1.50468300800507	1.27089622777104

Equilibrium S_0 structure for **[7]*oi*Pr**, wB97X-D/cc-pVTZ

88

C	3.146623	0.396597	0.434193
C	4.454427	0.332221	0.582591
C	1.895352	0.440007	0.270889
C	-1.895390	0.440056	-0.270858
C	-3.146652	0.396649	-0.434229
C	-4.454450	0.332219	-0.582651
C	5.161031	-0.973041	0.693198
C	5.248212	1.581922	0.750965
C	-5.161004	-0.973074	-0.693221
C	-5.248287	1.581885	-0.751026
C	6.313757	1.885914	-0.106677
C	7.056867	3.032208	0.156303
C	6.755391	3.869154	1.217026
C	5.680255	3.578252	2.040579
C	4.933186	2.438876	1.803383
C	4.988699	-2.031305	-0.209905
C	6.046370	-1.113620	1.764394
C	6.732177	-2.292081	1.978449
C	6.549600	-3.351127	1.102822
C	5.694928	-3.209266	0.025837
C	-6.313817	1.885856	0.106643
C	-7.056978	3.032116	-0.156339
C	-6.755566	3.869050	-1.217090
C	-5.680442	3.578174	-2.040667
C	-4.933321	2.438832	-1.803468

C	-6.046319	-1.113733	-1.764426
C	-6.732076	-2.292231	-1.978441
C	-6.549471	-3.351232	-1.102766
C	-5.694818	-3.209292	-0.025775
C	-4.988638	-2.031294	0.209925
C	4.107349	-1.934874	-1.440669
C	2.847341	-2.789237	-1.286434
C	4.869949	-2.296387	-2.717681
C	6.644062	1.030499	-1.315656
C	6.678267	1.854420	-2.604410
C	7.947233	0.254085	-1.120461
C	-6.644047	1.030466	1.315662
C	-6.678192	1.854422	2.604396
C	-7.947220	0.254032	1.120561
C	-4.107300	-1.934771	1.440688
C	-4.869889	-2.296261	2.717713
C	-2.847254	-2.789086	1.286498
H	7.354425	4.752221	1.393844
H	7.887278	3.283275	-0.491031
H	5.427710	4.229805	2.865689
H	4.099123	2.190126	2.445937
H	7.404291	-2.382979	2.820472
H	6.187723	-0.279059	2.438085
H	7.078071	-4.282690	1.253493
H	5.574713	-4.038851	-0.658617
H	-5.574579	-4.038844	0.658714
H	-7.077904	-4.282822	-1.253405
H	-7.404174	-2.383191	-2.820470

H	-6.187696	-0.279206	-2.438154
H	-4.099267	2.190101	-2.446039
H	-5.427945	4.229720	-2.865797
H	-7.354638	4.752091	-1.393910
H	-7.887378	3.283167	0.491015
H	3.787450	-0.899849	-1.545054
H	5.842987	0.303249	-1.434560
H	-5.842958	0.303228	1.434545
H	2.201713	-2.679549	-2.158634
H	2.280351	-2.494005	-0.404117
H	3.103875	-3.845790	-1.186828
H	5.157487	-3.348446	-2.735993
H	5.777739	-1.699745	-2.817119
H	4.243679	-2.112168	-3.591277
H	7.503854	2.567568	-2.606120
H	5.751443	2.411688	-2.739709
H	6.811014	1.196678	-3.464554
H	8.149711	-0.374296	-1.989263
H	7.895000	-0.387724	-0.241591
H	8.790595	0.936106	-0.995578
H	-7.503781	2.567568	2.606125
H	-5.751363	2.411697	2.739634
H	-6.810895	1.196704	3.464565
H	-8.149634	-0.374337	1.989386
H	-7.895034	-0.387791	0.241699
H	-8.790600	0.936038	0.995720
H	-5.157365	-3.348336	2.736081
H	-5.777713	-1.699666	2.817115

H	-4.243634	-2.111959	3.591302
H	-2.201637	-2.679334	2.158698
H	-2.280270	-2.493868	0.404173
H	-3.103744	-3.845654	1.186934
H	-3.787449	-0.899726	1.545028
C	0.626467	0.456064	0.089400
C	-0.626508	0.456078	-0.089339

References

[1] M. J. James, N. D. Grant, P. O'Brien, R. J. K. Taylor, W. P. Unsworth, *Org. Lett.*, **2016**, *18*, 6256–6259.

[2] M. Berberan-Santos, E. Bodunov, B. Valeur, *Chem. Phys.*, **2005**, *315*, 171–182.

[3] S. Grimme, M. Waletzke, *J. Chem. Phys*., **1999**, *111*, 5645−5655; C. M. Marian, A. Heil, M. Kleinschmidt, *WIREs Comput. Mol. Sci.,* **2019**, *9*, e1394.

[4] B. O. Roos, P. R. Taylor, P. E. M. Siegbahn, *Chem. Phys.* **1980**, *48*, 157–173.

[5] C. Angeli, R. Cimiraglia, S. Evangelisti, T. Leininger, J. P. Malrieu, *J. Chem. Phys.* **2001**, *114*, 10252–-10264, DOI 10.1063/1.1361246.

[6] C. Angeli, R. Cimiraglia, J. P. Malrieu, *J. Chem. Phys.* **2002, 117**, 9138–-9153, DOI 10.1063/1.1515317.

[7] C. Bannwarth, S. Ehlert and S. Grimme., J. Chem. *Theory Comput.*, **2019**, *15*, 1652–1671.

[8] C. Bannwarth, E. Caldeweyher, S. Ehlert, A. Hansen, P. Pracht, J. Seibert, S. Spicher, S. Grimme, *Comput. Mol. Sci.*, **2020**, *11*, e01493.

[9] The Effects of Ring Strain on Cyclic Tetraaryl[5]cumulenes, B. Sun, M.S. Oakley, K. Yoshida, Y. Yang, M. Tommasini, C. Zanchi, A. Lucotti, M.J. Ferguson, F. Hampel, M. Klobukowski, R.R. Tykwinski, *Chem. Eur. J.,* **2022**, *28*, e202200616.